Lifetime measurements of excited nuclei through modern nuclear spectroscopy

By

Lumkile Msebi

Supervisor

Dr. P. Jones

iThemba LABS(Cape Town)

Co-supervisors

Dr. M. Herbert

University of the Western Cape

Prof. J.F. Sharpey-Schafer

University of Zululand

A thesis submitted to the Faculty of Science

University of Western Cape, Cape Town

in fulfilment of the requirements for the

degree of Doctor of Philosophy.

September, 2021

A Dedication to my Family and wife to be...

"The dawning of a new day, I can feel it over me now. The Light of a new day....I can feel the rays of His Light breaking through upon my soul. The new day. The old one is pressing away. "

Candidate's Declaration

I declare that this thesis is my own, original work. It has not been submitted before.

Lumkile Msebi

September 2021

Abstract

The progressive development of scintillator detectors has made it possible to perform direct electronic lifetime determination up to a few hundred nanoseconds. The 2" by 2" $LaBr_3$:Ce detectors provide a combination of excellent time resolution and good energy resolution. Recently a fast timing array has been commissioned at iThemba LABS, Cape Town consisting of eight 2" by 2" $LaBr_3$:Ce detectors. Test measurements using radioactive sources produced at the laboratory were conducted. Six 2" by 2" $LaBr_3$:Ce detectors were coupled to the AFRODITE array as their first in-beam experiment. AFRODITE consisted of eight HPGe clover detectors as well as two 3.5" x 8" $LaBr_3$:Ce detectors. A particle telescope was used to select the desired reaction channels. The reactions of interest ^{45}Sc(p,d)^{44}Sc and ^{45}Sc(p,α)^{42}Ca were carried out at a beam energy of 27 MeV. The current analysis also investigates the rare earth nucleus ^{150}Gd which was populated through ^{150}Sm(α,4n)^{150}Gd at a beam energy of 48 MeV. Through these reactions, excited states that have lifetimes which are apt for the characterization of the 2" by 2" $LaBr_3$:Ce detectors were populated. Various techniques such as the slope method and the centroid shift method have been employed to extract the lifetimes of excited states. Lifetimes that were previously measured for ^{44}Sc and ^{42}Ca were measured again in this work. New lifetimes were obtained ^{44}Sc and ^{150}Gd. Shell Model calculation were done to compare experimental and theoretical results. All these endeavours will seek to unveil the quadrupole moment of nuclei and their intrinsic behaviour.

Acknowledgements

Namhla kunamhla! Namhla siyakwazi ukuba sibelapha emva kwendudumo nezaqhwithi. Sizakuvuya, sonwabe, senzenjeya kuba ililisele laqandula. Namhla siyakwazi ukuba siyozikha sibone namakhoba. Inga ingomso iqaqambe njengale mini yanamhla.

When traversing through uncharted, uncertain and unforgiving territory. When in the midst of rough seas with high waves perpetually crushing against me. When the mist of despair fills air with despondency ... I have learned to put my trust in thee Oh Lord and to say my help comes from Thee. Because of Thee Oh Lord I can be on the victorious end and tell a story of how I overcame. That I can be able to stand on the victorious end, makes me to be ever Eternally grateful to none other but Thee Oh Lord.

"If you can watch the things you have given your life to broken and stoop over to build 'em up with worn out tools. If you can force your heart and nerve and sinew to serve your turn long after they are gone And so hold on when there is there is nothing in you Except the will that says to them 'Hold on'... Yours is the Earth and everything in it..." In my journey towards achieving this goal, the potent words poem has been my inspiration and a necessary one. The poem does not end with these words neither does my inspiration and it would be a gross in justice no to acknowledge the following people.

I am indebted to my mother, Sharon Msebi, for all the love, support and care that did not start with achieving this goal but from birth. With little to support us as family, she made endless sacrifices to ensure that we live to the next day and even to a Greater Day. I thank her because it is through of her that I was able to go through my basic education when there was no means to do so. I thank her because it is through that I could obtain a university degree. I thank her because it is through her that when there was no means to take me to university she had immerse

faith and accompanied me to register at a university for the first time. I thank her because it is through her that when things were difficult at home and even for myself at university she stood like a mother eagle to brood an atmosphere of hope in the face of adversity.

Posthumously, I would like thank my father, Vuyisile Msebi, whose role as a father figure has shaped me in many ways. I thank him for working day and night to build a better future for us. His stern guidance has benefited me and indeed I continue to reap those benefits. When pursuing this journey and all other journeys in my life, I have this blessed hope that he wanted the best for me and therefore I should give my best. May his soul resurrect to Life Eternal.

I thank my one and only sister, Bulelwa Msebi, whose not only a sister but a friend. In pursuit of this achievement, I had to be away from home and this did not sit well with her. This did not sit well with me either but in the end it was not in vain because the trophy is coming home. I thank my brother, Xolela Msebi, knowing very well that he expected me to finish and bring the trophy home. I thank my brother, Thobile Msebi, for always wanting know how things are progressing. I deeply and sincerely thank my family for bearing with me in my absence from home even when times were tough.

Let me express my heart felt gratitude to none other than Prof. John Sharpey-Schafer. Our journey did start with my PhD studies but from my Masters degree. Ever since then he has been not only supervisor but also a mentor, friend and a father figure. It is very rare to have someone who occupies such a senior role to be able to have so much empathy, care and love. With him, I could always confide and and know that he has my best interest at heart. We would talk about anything and everything to a point that I become oblivious that he is my co-supervisor. Lockdown has robbed us of all the wonderful and fun moments we would have at his house where he and his precious wife, Sylvie, would receive us for lunch or dinner. There is never dull moment when he is around because he is the Best. Long may his fruits of love, care and legacy live on for many generations to come.

I thank my supervisor Pete Jones for the role he played in this journey. I thank him for also assisting me with the code that had me worried for a long time and it seemed very impossible that things would work but in the end all things worked out. I thank Prof Robert Lindsay for all the administration and ensuring that I my records are up to date even though I was not his student. He really went out of his way even when there were difficulties, he would find a solution.

ACKNOWLEDGEMENTS

I appreciate all the efforts knowing full well that he did not have to do it but he was still willing to assist. I thank Prof. Sifiso Ntshangase and Doctor Siyabonga Majola for all the discussions we would have and the ideas they would share with me. I thank my friends Bonginkosi Zikhali, Abraham Avaa, Doris Jiotsa Kenfack, Mistura Ajani, Maluba Chisapi and Munirat Bashir for all the collaboration, discussions and assistance. Indeed I can look back and say I have had a privilege of working with such great people in my life.

Contents

List of Figures

List of Tables

Chapter 1

Introduction

1.1 Introduction

Advances in gamma-ray spectroscopy have led to massive strides in unveiling the underlying properties of nuclear structure. These advances are complimented by the ever progressing development in technology that has launched modern gamma-ray spectrometer arrays that are hybrid in nature. It is always desirable, in the study of nuclear structure, to have the best energy resolution, optimal time resolution and highest efficiency without prejudicing the quality of the data. Scintillator detectors have made a steady progress in recent years with the latest development being $LaBr_3$:Ce scintillator detectors, which boast of good energy resolution and excellent timing properties [1]. With the recent acquisition of an array of eight 2" by 2" $LaBr_3$:Ce detectors at iThemba LABS, it has been possible to probe the performance of $LaBr_3$:Ce detectors first hand. Various functions and capabilities of these detectors are explored in this current study. The existing iThemba infrastructure, the AFRODITE Array, is complimented by the $LaBr_3$:Ce detectors to obtain a comprehensive analysis of the behaviour of excited nuclei. With the ongoing endeavours to build larger and more improved hybrid spectrometers at iThemba LABS, such as the African Lanthanum Bromide Array, this study is a prelude of the valuable physics that can be produced by these hybrid detector arrays.

Of strategic importance to the effectiveness of these detectors is their ability to measure the lifetimes of nuclear excited states. In nuclear physics, the lifetimes of excited states span a broad range from 10^{-15} to 10^{3} seconds. Different methods have been developed to study these lifetimes that cover a certain time range. Studies of the lifetimes of radioactive decay transitions have been crucial in unveiling the complex structure of a nucleus. To gain more in depth knowledge about

the fundamental properties of a nucleus, the lifetimes of excited states prove to be an essential tool. Factors that have a direct bearing on the lifetimes such as the electromagnetic nature of a transition, its energy and multiplicity all form part of the fundamental properties in question. The transition matrix elements have a direct relationship with lifetimes of excited states thus revealing the underlying physics of nuclei. Moreover, from the lifetimes of excited states one is able to determine the transition probability and hence the quadrupole moment. From the quadrupole moment, the deformation character of a nucleus can be deduced. Collective quadrupole and octupole modes may be identified from the magnitude and spin and parity dependence of transition rates [2]. These electromagnetic transition rates may be obtained from the partial mean life of excited states.

This work looks at lifetimes of excited states for nuclei in mass region $A > 40$, ^{44}Sc and ^{42}Ca as well as a nucleus in the rare earth region, ^{150}Gd. The ^{44}Sc and ^{42}Ca nuclei have lifetimes over a wide dynamic range, providing us an excellent opportunity to aptly characterize the 2" by 2" $LaBr_3$:Ce detectors. The lifetimes of these nuclei have been previously studied using various methods including the Doppler Shift Attenuation Method and the Recoil Distance Doppler Shift Method [3, 4, 5, 6, 7, 8, 9, 10, 11, 12]. Using the modern fast-timing technique, this study provides a thorough measurement of the excited states and a detailed analysis in these nuclei.

The advent of scintillator detectors gave birth to a much more efficient way of measuring lifetimes of excited nuclear states directly. The direct measurement of lifetimes using electronic means is called fast-timing. The present work seeks to reveal how 2" by 2" $LaBr_3$:Ce scintillator detectors, incorporated to digital pulse processing (DPP) modules, are paramount in the technique of fast-timing.

1.1.1 Motivation for the present study

This present work explores the nuclear properties in gamma-ray spectroscopy through the use of $LaBr_3$:Ce scintillator detectors. It characterizes the recently commissioned 2" by 2" $LaBr_3$:Ce scintillator detectors and measures their performance and properties in realistic experimental set-ups. Through these detectors, this work seeks to investigate how the fundamental properties of the nuclei currently studied. A broad insight into the underlying physics is provided here with nuclei in the mass region $A > 40$ and the intriguing rare earth nuclei. The eminent shell model is put to the test, through experimental results and calculations, in the present study. In the shell model framework, nucleons are held together by the strong interaction inside of a volume with a radius of a few Fermis. The nucleus is considered as a closed shell with n number of valence nucleons as shown in Fig1.1. This model is based on an assumption, as a first approximation, that

each nucleon moves independently in a spherically symmetric potential including a spin-orbit term.

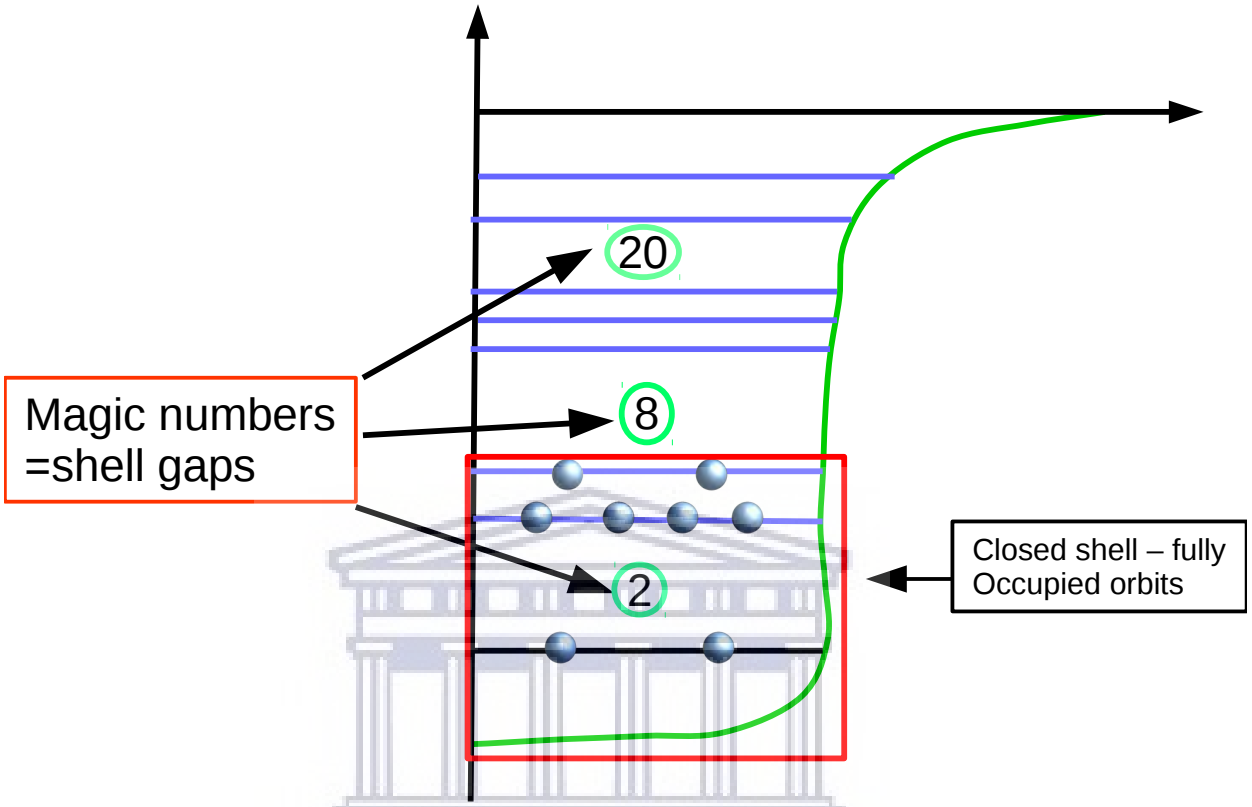

Figure 1.1: Single particle levels accommodate nucleons based on Pauli's exclusion principle to form the shell structure of the nucleus. A certain combination of nucleons exhibit a rather stable phenomenon and are called magic numbers.

The nuclei, ^{44}Sc and ^{42}Ca, both have valence nucleons in the $f_{7/2}$ orbit, discussed in section 2.5. This orbit is energetically favoured [13] and it is an orbit in which prospects of shape coexistence are investigated. Indeed it was in the 1970s that the phenomenon of shape coexistence in the $f_{7/2}$ was discovered and studied in the odd- A isotopes [14]. The shape coexistence phenomenon can emerge in the proximity of shell and subshell closures. It is an extremely important phenomenon in the field of nuclear structure and it is revealed by the transition probabilities as a function of the wavefunction content of nuclear states [2]. The present study seeks to canvass how this phenomenon plays itself out in ^{44}Sc and ^{42}Ca nuclei. This is made possible by utilizing 2" by 2" $LaBr_3$:Ce detectors to extract lifetimes, from which transition probabilities are obtained. The ^{44}Sc and ^{42}Ca nuclei are well suited in unpacking critical aspects of the nuclear properties since they lie close to the doubly magic ^{40}Ca and ^{56}Ni. For this reason, their structure can be interpreted in terms of competition between single-particle or collective excitations. The present work delves

more in deeply into the underlying nucleon-nucleon interactions, seeking to understand charge independence and charge symmetry.

The rare earth nucleus ^{150}Gd is a different mass region. The nucleus ^{150}Gd is the fourth nucleus in which discrete superdeformed bands were discovered [15]. It is suspected that the lack of yrast traps in this nucleus is due to its number of protons $Z = 64$, being at sub-shell closure. Rotational bands have been proposed by *Lipas et al* [16] that are similar to the lowest levels of collective bands in normally deformed nuclei. The present work seeks to investigate the collectivity, be it quadrupole or octupole, of these rare earth nuclei, which can be inferred from reduced transition probabilities. Lifetimes of these excited states yield spectroscopic factors and observables which are timid to the structure of the intrinsic wave-functions. Accordingly, it is necessary to observe the systematics of transition probabilities to gain a broader insight into the properties of nucleus in relation to other neighbouring nuclei.

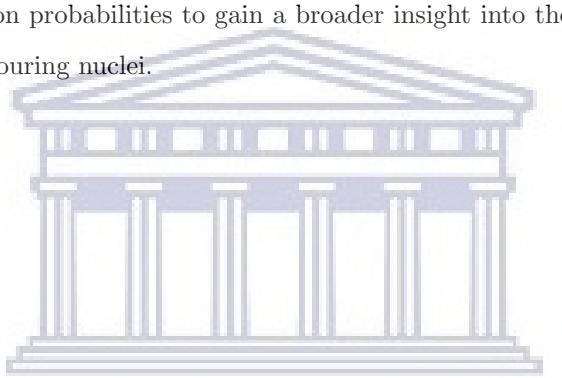

Chapter 2

Nuclear Structure Theory

2.1 Radiation interaction with matter

Radiation can interact with matter through atomic nuclei or extranuclear electrons. In most cases these interactions involve a transfer of energy from the radiation to the matter with which it interacts [17]. The discussion that follows is about how gamma rays interact with matter. The rest of attenuation mechanisms are discussed in depth in ref [17]. There are three ways in which gamma rays interact with matter:

2.1.1 Compton scattering

Inelastic scattering is a scattering process in which kinetic energy is not conserved. One such scattering is Compton scattering. Compton scattering is particularly important in this work as it affects the quality of the timing information. Compton scattering was discovered in 1922 by Arthur H. Compton (1892-1962) while conducting research on the scattering of X-rays by light elements [18]. In Compton scattering a photon interacts with an electron thereby transferring some of its energy to an electron. This results in a decrease in energy of the photon and an increase of the wavelength. Figure 2.1 an incoming photon of energy:

$$E = \frac{hc}{\lambda} \tag{2.1}$$

and momentum

$$p = \frac{E}{c} \tag{2.2}$$

interacts with an electron and kinetic energy and momentum are conserved. In general, it is not

possible that the electron moves in the direction of the photon, since mass, energy and momentum must be conserved.

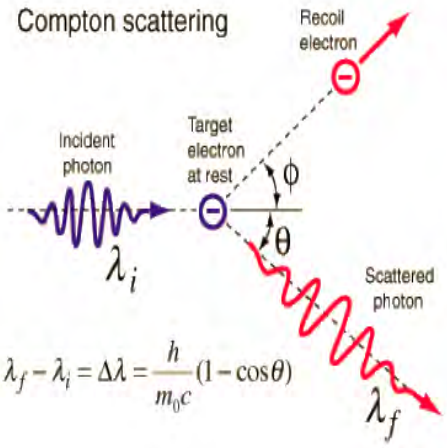

Figure 2.1: Compton scattering diagram showing the relationship of the incident photon and electron initially at rest to the scattered photon and electron given kinetic energy. The change in wavelength formula shown here results from the conservation of energy and momentum [19].

The change in wavelength of a photon as a result of the conservation of energy and momentum can be written in the following manner:

$$1/E' - 1/E = \frac{1}{m_e c^2} \times (1 - cos\theta) \tag{2.3}$$

It is important to note that the energy and the momentum are expressed in their relativistic terms. This effect is very crucial since it demonstrates that light cannot be explained purely as a wave phenomenon. Classically, light was thought as an electromagnetic wave but this could not explain the low intensity shifts in wavelength. To explain the low intensity Compton scattering, light must behave as if it consists of particles.

Through quantum electrodynamics Oskar Klein and Yoshio Nishina derived the probability of a photon being Compton scattered into a given solid angle $d\Omega$. The Klein-Nishina cross section for scattering from a free electron is:

$$\frac{d\sigma}{d\Omega} = \frac{r_0^2}{2}\frac{f}{(1+g)^3}(1 + \frac{g^2}{f(1+g)}) \tag{2.4}$$

where

$$r_0 = \frac{e^2}{4\pi\varepsilon_0 m_e c^2} \tag{2.5}$$

is the classical radius of the electron

$f = 1 + cos^2\theta$

$g = \frac{E_0}{m_e c^2}(1 - cos\theta)$

2.1.2 Photoelectric effect

The photoelectric effect is the interaction between a photon and a tightly bound electron. The binding energy of the electron must be equal to or smaller than the energy of the photon. In the photoelectric effect, the photon transfers all of its energy to the electron and is completely absorbed as illustrated by Fig.2.2. The photoelectron or the struck electron dissipates its energy in the absorbing medium mainly by excitation and ionization. The kinetic energy of the photoelectron is given by:

$$T_e = E_\gamma - B_e \tag{2.6}$$

where E_γ is the energy of the incoming photon given by Eq.2.1 and B_e is the binding energy of the photoelectron. The binding energy is transferred to the absorbing medium through fluorescent radiation that follows the initial interaction. The photoelectric effect is favoured for low photon energies less than 200 keV for germanium because the entire energy of the photon is deposited into the detector. It is this very strong dependence of photoelectric absorption on the atomic number Z that makes lead such a good material for shielding against X-rays [17].

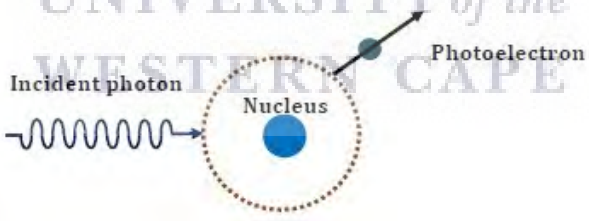

Figure 2.2: A schematic diagram illustrating the photoelectric effect.

2.1.3 Pair production

Pair production takes place when a gamma ray or photon, in an intense electric field near the nuclei, is transformed to an electron-positron pair. This electron positron pair is formed when the energy of gamma ray is greater than $2m_0c^2$ (approximately 1.022 MeV) in the strong Coulomb field of a nucleus. The energy of the photon partly appears as the rest masses of the two particles and partly as the kinetic energies of the electron (E_e) and positron (E_p):

$$h\nu = E_e + E_p + 2m_0c^2 \tag{2.7}$$

The positron slows down and comes to rest and encounters an electron through the force of attraction. Annihilation then takes place in which the electron and positron rest masses are converted into two γ rays, each with energy of 511 keV. The annihilation γ rays are emitted in the opposite direction, as illustrated in Fig.2.3, in order to conserve momentum and they may interact in the absorbing medium by either photoelectric absorption or Compton scattering [20].

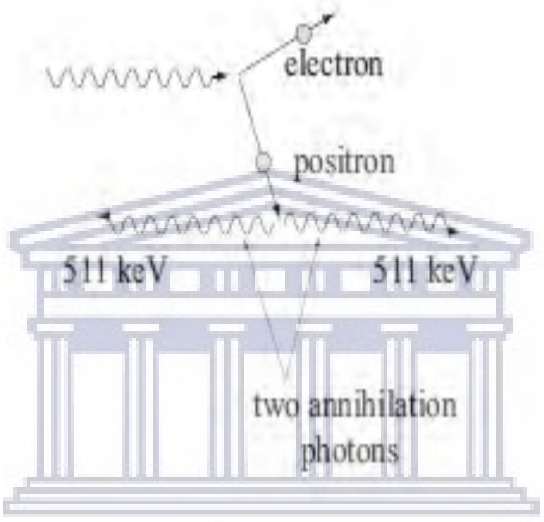

Figure 2.3: Pair production and annihilation. The two annihilation gamma rays are produced as a result of annihilation between a positron and an electron.

2.2 Scintillation and photomultiplier tubes

A scintillator is a material that converts energy lost through ionizing radiation into pulses of light. When a γ ray interacts with matter it may lose its energy by creating electron-hole pairs. Figure 2.4 illustrates how the primary electrons, created through this interaction, raise secondary electrons to the conduction band, thereby leaving holes in the valence band. If an electron de-excites, by falling from the conduction band to the valence band, it emits electromagnetic radiation in the form of a photon. The energy of this photon is high (around optical wavelengths) and is easily detected by the photomultiplier, since it is sensitive to it [21].

Since the scintillation crystal produces pulses of light, these have to be converted to an electrical signal in order to be processed by a computer. This is the function of the photomultiplier tube (PMT) as illustrated in Fig.2.5. First, the light photon strikes the PMT, free electrons from the

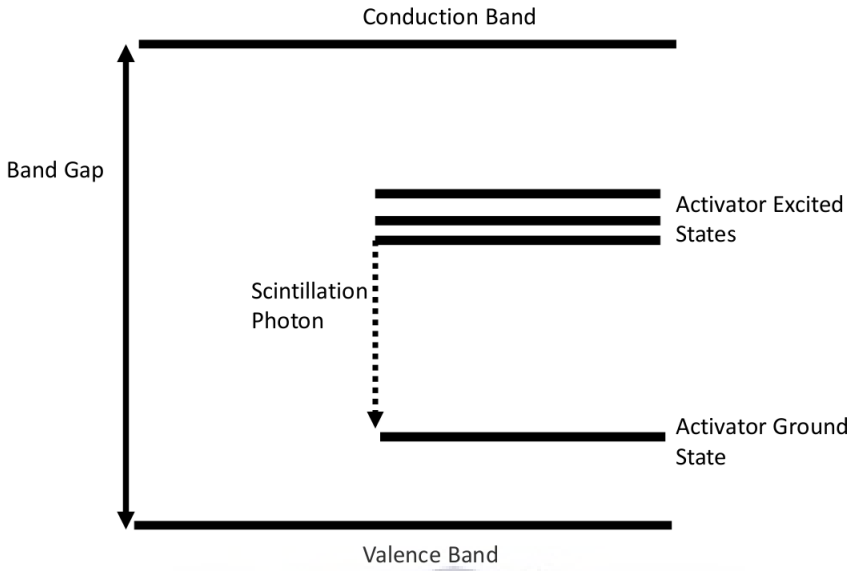

Figure 2.4: Discrete energy bands of an activated crystalline scintillator. The forbidden band is also represented here by the activator excited states lines.

cathode, causing it to emit a photoelectron. The photoelectrons are accelerated by a high voltage potential difference and are focused electrostatically onto the first of a series of electron multiplier stages, called dynodes. These emit more electrons than they receive, thus amplifying the signal. As the electrons progress from the first dynode to the next they are multiplied, a process that is repeated along the series of dynodes. The anode collects the amplified signal and then outputs it on the measurement circuit.

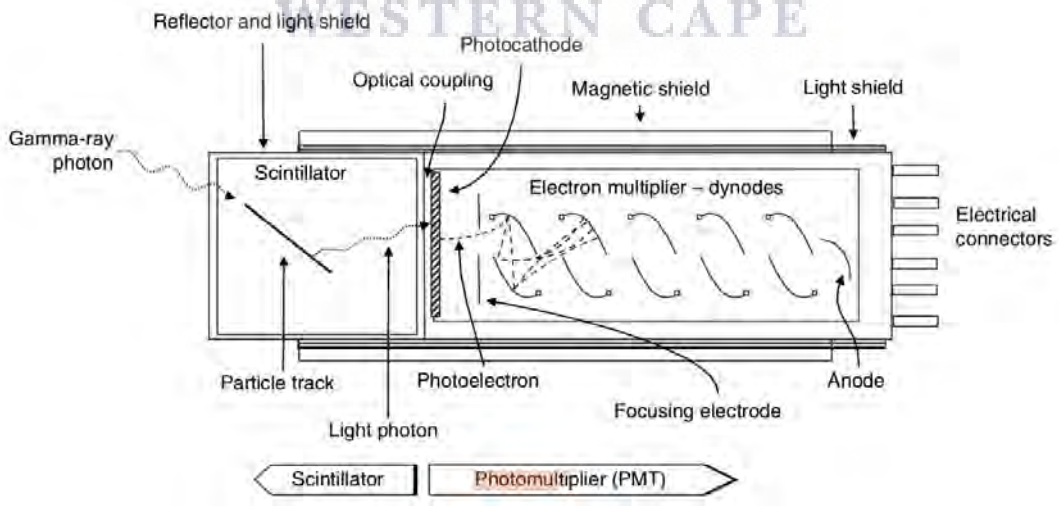

Figure 2.5: A scintillator-photomultiplier tube detector assembly [21].

2.3 Electromagnetic properties and nuclear levels

Because nuclear energy levels are discrete in nature, they are governed by principles of quantum mechanics. In particular, quantum properties such as angular momentum, isospin and parity characterize each energy level or excited state. An excited nuclear state i decays to a lower excited state j through photon emission, hence angular momentum and energy are conserved thus the energy of the photon will be:

$$\hbar\omega = E_i - E_f \tag{2.8}$$

The total angular momentum of a nuclear system is given by:

$$I = L \pm S \tag{2.9}$$

where L is the orbital angular momentum which is an integral multiple of $\hbar$ and S is the spin angular momentum with a value of half integral multiple of $\hbar$.

Excited nuclear states are usually de-excited through electromagnetic transitions by emission of γ rays or by internal conversion [22]. Thus the underlying behaviour of nuclei can be studied through electromagnetic interactions with the benefit of the fact that these interactions are weak compared to the strong force. Charge distributions and current distributions of excited states are unique for each excited nuclear state. These result in electric and magnetic moments in nuclei respectively.

The transitions that involve the emission of electromagnetic radiation are best described in terms of multipole expansion. Theoretically, transition strengths are predicted to be dependent on the multipole order. The lower orders of the multipole moment, such as monopole, dipole, quadrupole and hexadecapole account for significant contributions in the interaction of the electromagnetic field with nucleons. The commonly observed modes of γ radiation are the electric dipole *E1*, magnetic dipole *M1*, electric quadrupole *E2*. Current and charge distributions influence multipole moments and consequently influence single particle and collective behaviour. The γ ray selection rules state that the γ ray decay between states of initial spin J_i^π and final state spin J_f^π proceed by a photon of multipole order L where:

$$\mid J_i + J_f \mid \geq L \geq \mid J_i - J_f \mid \tag{2.10}$$

The parity operator validates whether the wave function of a nuclear state changes its sign under a reflection in space. It transforms $\psi(\mathbf{r})$ into $\psi(\mathbf{-r})$ such that:

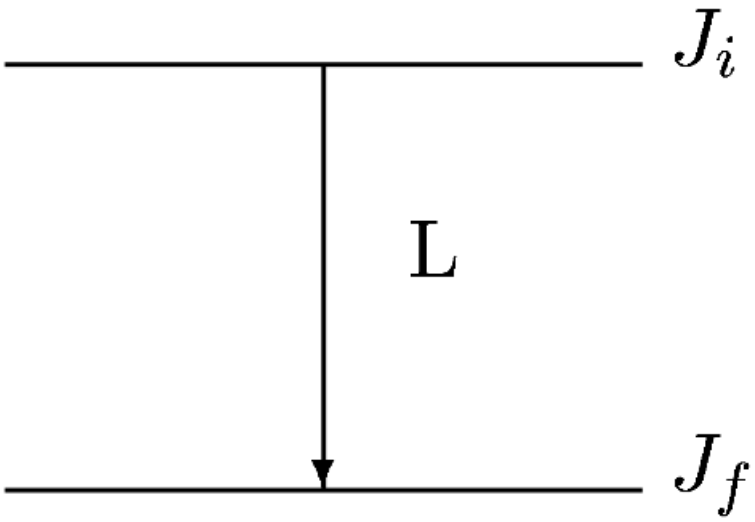

Figure 2.6: Schematic decay scheme showing a gamma transition from initial spin J_i^π to final state spin J_f^π

for even parity $\psi(\mathbf{r}) = \psi(\text{-}\mathbf{r})$

for odd parity $\psi(\mathbf{r}) = \text{-}\psi(\text{-}\mathbf{r})$

The parity of a multipole order L is given by $\pi = (-1)^{L+1}$ and $\pi = (-1)^L$ for a magnetic transition and an electric transition respectively. The parity of a wave-function is that of the spherical harmonics in a central potential:

$$Y_l m_l(\theta, \phi) = Y_l m_l(180 - \theta, \phi + 180) = (-1)^l Y_l m_l(\theta, \phi) \tag{2.11}$$

where for spherical harmonics the transformation $\mathbf{r} \rightarrow \text{-}\mathbf{r}$ is equivalent to a rotation in ϕ through an angle of 180° and $\theta \rightarrow 180° - \theta$. Looking at 2.6, the initial state can be expressed as $|\psi_i> = |\alpha J_i M_i>$ and the final state as $|\psi_f> = |\beta J_f M_f>$, for a given electric or magnetic transition, (X), with operator M of a defined multipolarity λ. The Wigner-Eckart theorem can be used to express the matrix elements as a function of the reduced matrix element, $<\psi_f \,||\, M(X\lambda) \,||\, \psi_i>$, which does not depend on the third component of the nuclear spin (the magnetic quantum number) [2].

2.3.1 Electric quadrupole moment

Atomic nuclei with the nuclear spin ≥ 1 are bound to have nuclear quadrupole moments. Consider a charged particle moving around an orbit with radius r as depicted in Fig.2.7. Classically, the electric quadrupole moment (Q_0) takes the form $q(3z^2 - r^2)$ for the axial symmetry where z is the orientation of the field. If the charged particle moves with spherical symmetry then:

$$\bar{x}^2 = \bar{y}^2 = \bar{z}^2 = \frac{1}{3}\bar{r}^2 \quad \text{and} \quad Q_0 = 0 \tag{2.12}$$

If the charged particle moves in the xy plane, see Fig.2.7, then $z = 0$ and the electric quadrupole moment is negative $Q_0 = -r^2$.

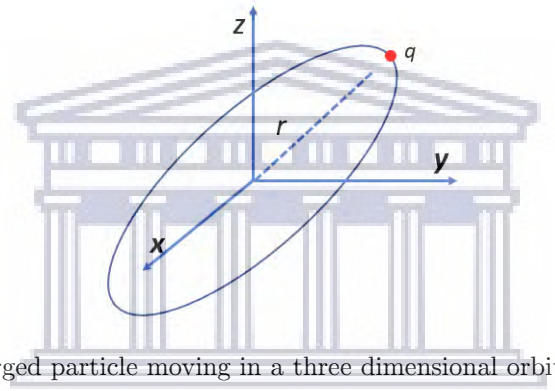

Figure 2.7: A charged particle moving in a three dimensional orbit with radius r.

For any given nucleus, the quadrupole moment will be a sum of the quadrupole moments of each nucleon. For most nuclei, however, the quadrupole moment can be estimated from the valence nucleon [22]. This is because paired nucleons move in spherically symmetric orbits and thus do not contribute to the quadrupole moment. The quadrupole moment is expressed in units of barn $(b) = 10^{-28}m^2$, with an expected range between 0.06 eb and 0.5 eb. The quadrupole moment in classical physics:

$$Q_0 = \int_v \rho(r,\theta)(3z^2 - r^2)dV \tag{2.13}$$

where ρ is the charge density of the infinitesimal volume dV, r is the distance to dV and z is the projection of r onto the z axis.

While in quantum mechanics, it can be expressed as :

$$Q_0 = \sum_1^z \int_v \psi^*(3z^2 - r^2)\psi_i dV \tag{2.14}$$

Here, distinction is drawn between the intrinsic quadrupole moment Q_0 and the spectroscopic quadrupole moment Q. In Fig.2.8, the quadrupole moment operator $Q_2(r^{'})$ is defined relative to the intrinsic coordinate system $x^{'}$, $y^{'}$ and $z^{'}$. The intrinsic quadrupole moment is given by the expectation value of $Q_2(r^{'})$ and it is what would be measured in the intrinsic coordinate system (if it were possible to make this measurement). The relationship between the intrinsic quadrupole moment and the reduced transition probability of an $E2$ is defined by this model dependent formula:

$$B(E2) = \frac{5}{16\pi}(eQ_0)^2 \mid< J_i K 20 \mid J_f K >\mid^2 \tag{2.15}$$

where $< J_i 2K0 \mid J_f K >$ are the Clebsch-Gordon coefficients for the transition decaying from a state of spin J to one of $J-2$ given by:

$$< J_i 2K0 \mid J_f K >= \sqrt{\frac{3(J-K)(J-K-1)(J+K)(J+K-1)}{(2J-2)(2J-1)J(2J+1)}} \tag{2.16}$$

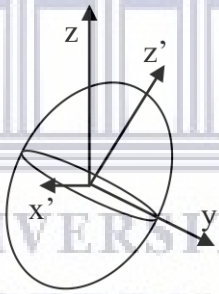

Figure 2.8: The intrinsic coordinate system with its axes fixed with the nuclear axes of symmetry.

The intrinsic quadrupole moment of a charge distribution gives information on the type of deformation, if any, of a nucleus as shown in Fig.2.9.

The spectroscopic quadrupole moment Q is the quadrupole moment measured in the laboratory coordinate system x, y, z, for which the z-axis corresponds to the maximum projection of the nuclear angular momentum ($M = I$). Techniques that measure the nuclear quadrupole moment by its interaction with the gradient of an external electric field, obtain results for the spectroscopic quadrupole moment. The relation between the two quadrupole moments is:

$$Q = Q_0 \frac{3K^2 - I(I+1)}{(I+1)(2I+3)} \tag{2.17}$$

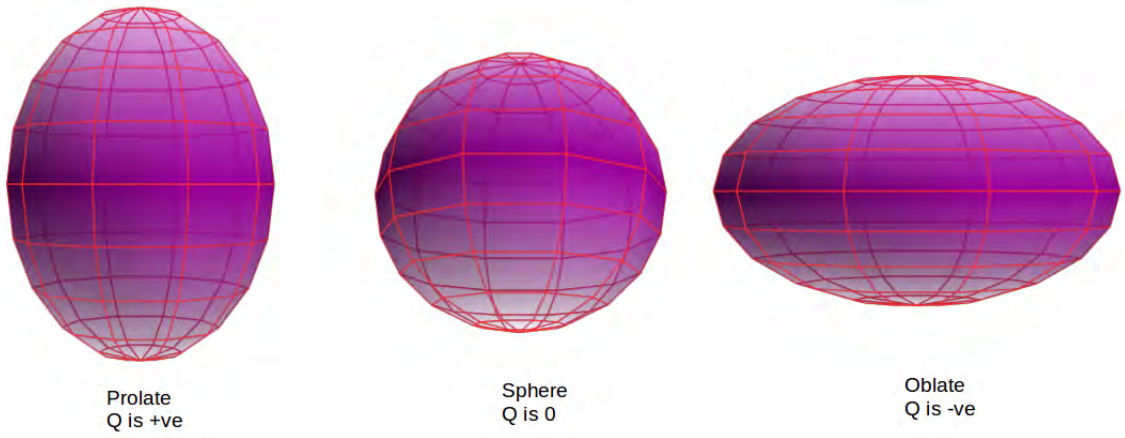

Figure 2.9: Different nuclear shapes as dictated by the intrinsic quadrupole moment values.

2.4 Transition Probability

During the process of de-exciting from one nuclear state to another, photons are emitted. The multipole order of the transition associated to the angular momentum transferred is 2^L, with L being a quantum number. The transition probability for γ ray emission can be expressed as [23]:

$$\lambda_{fi}^{(\sigma L)} = \frac{2}{\epsilon_0 \hbar} \frac{L+1}{L[(2L+1)!!]^2} \left(\frac{E_\gamma}{\hbar c}\right)^{2L+1} |< \xi_i J_i m_i \mid M_{\sigma L \mu} \mid \xi_f J_f m_f >|^2 \tag{2.18}$$

where σ is the type of transition with E for the electric and M for magnetic transition.
L and μ are the quantum numbers for the angular momentum and its projection.
E_γ is the transition energy ξ represents all other quantum numbers besides angular momentum and its projection. $< \xi_i J_i m_i \mid M_{\sigma L \mu} \mid \xi_f J_f m_f >$ is the nuclear matrix element of the transition $< \xi_i J_i m_i \mid \rightarrow < \xi_f J_f m_f \mid$ (Note that knowledge of the initial and final wave-functions is important). Evaluation of the nuclear matrix element is necessary in order to determine transition probability.

Equation 2.18 gives the transition probability for one sub-process and depends on the transition energy, being related to E^{2L+1}. In order to obtain the total transition probability that determines a lifetime of the initial state we have to sum over all the possible substates [24]. So Eq.2.18 can be written as:

$$\lambda_{fi}^{(\sigma L)} = \frac{2}{\epsilon_0 \hbar} \frac{L+1}{L[(2L+1)!!]^2} \left(\frac{E_\gamma}{\hbar c}\right)^{2L+1} B(\sigma L; \xi_i J_i \rightarrow \xi_f J_f) \tag{2.19}$$

where

$$B(\sigma L; \xi_i J_i \rightarrow \xi_f J_f) = \frac{1}{2J_i + 1} \mid < \xi_f J_f \mid\mid M_{\sigma L} \mid\mid \xi_i J_i > \mid^2 \tag{2.20}$$

is the reduced transition probability and $<\xi_f J_f \parallel M_{\sigma L} \parallel \xi_i J_i>$ is the reduced transition matrix element. Here there is no energy dependency and the reduced transition probability is the squared transition matrix element. Although the reduced transition matrix element can be either electric or magnetic, the $E2$ component plays a crucial role in study of nuclear structure. In particular, the reduced transition matrix element for electric quadrupole transitions $B(E_2)$, and can quantum mechanically be expressed as:

$$B(E_2, J_i \rightarrow J_f) = \frac{1}{2J_i + 1} \sum_{m_i} \sum_{m_{f,\mu}} \mid <J_f m_f \mid (E2, \mu) \mid J_i m_i> \mid^2 \tag{2.21}$$

where the $(E2, \mu)$ is the electric quadrupole operator and $\mu = -2...2$. Information on the intrinsic properties of nuclei can be extracted from the B(E2) values, which are evidently wave-function-dependent.

Albeit, there are many instances where the electromagnetic radiation has a mixed contribution from electric and magnetic components. Experiments prove to be effective in determining the mixing ratio $\sigma(M1/E2)$.

2.4.1 Lifetimes of excited nuclear states

Lifetimes of excited nuclear states are proportional to the square of the transition matrix elements and can be simply expressed as [25]:

$$\Gamma\alpha \mid <\psi_f \mid M \mid \psi_i> \mid^2 \tag{2.22}$$

where Γ is the intrinsic energy width and is related to the lifetime by the Heisenberg uncertainty principle, τ is the mean lifetime of a nuclear state: $\Gamma\tau \geq \hbar$.

The transition matrix element is simplified for the purpose of this discussion such that:

ψ_f and ψ_i are the wave-functions of the initial and final states respectively.

M is the operator for the decay of the transition.

Following this relation, it is evident that lifetimes of excited nuclear states are an important observable since they provide crucial insight into the nature of nuclear excitations and their structure. Unstable nuclei decay to other nuclei through a fundamental law of radioactive decay:

$$N(t) = N_0 exp\left(-\frac{t}{\tau}\right) \tag{2.23}$$

where $N(t)$ is the number of nuclei at time t

τ is the mean lifetime of the nucleus and N_0 is the initial number of nuclei.

$\left(-\frac{t}{\tau}\right)$ can be written in terms of the characteristic decay constant λ as $(-\lambda t)$, and:

$$\lambda = \frac{1}{\tau} = \frac{ln2}{t_{\frac{1}{2}}} \tag{2.24}$$

where $t_{\frac{1}{2}}$ is half-life of an excited nuclear state.

Other than radioactive decay, nuclei posses excited states that exhibit unique lifetimes for each state. Equation 2.23 can be expanded, for more complicated excited nuclear systems, as follows:

$$\frac{d}{dt}N_j(t) = -\lambda_j N_j(t) + \sum_{i<j}^{n} \lambda_i N_i(t) b_{ji} \text{ (introduced by Bateman)[26]} \tag{2.25}$$

where b_{ji} is the branching ratio for a transition with initial level (i) and final level (j) and only n feeding levels are considered. The partial mean life τ_γ can be express as $\tau_\gamma = \frac{\tau}{br_\gamma}$ with br_γ as the branching ratio and τ the mean life of an excited state [2].

Excited nuclei decay via electromagnetic radiation by emitting γ rays as elaborated in section (1). It is apparent that by measuring the lifetime of an excited state, one is measuring the decay probability from one quantum state to another. To gain insight of the enhancement of a transition rate caused by collective nuclear effects, it is useful to express transition rates in Weisskopf units [2]. These units are used as a comparison point for the measured reduced transition probability, however, they are not meant to be true theoretical calculations to be compared with measured transitions. But rather, they provide reasonable relative comparisons of transition rates and are effectively useful as a yard stick as to the lifetime range expected for a typical decay of fixed multipolarity. The Weisskopf single particle estimates are shell model based and are used to find the approximate reduced transition probability. They can be calculated by taking a single-particle state with a wave-function that is constant inside the nucleus and zero outside it. Table 5.1 gives the single particle estimates for the reduced transition probabilities. It is important to note that nuclear de-excitations that are based on collective effects deviate substantially from the Weisskopf single particle estimates.

According to [27], the general Eq.for the single particle estimates for the reduced probability matrix element for an electric transition is:

$$B(Wu : EL) = \frac{1.2^{2L}}{4\pi}\left(\frac{3}{L+3}\right)^2 A^{\frac{2L}{3}} e^2 f m^{2L} \tag{2.26}$$

and for a magnetic transition is:

$$B(Wu:ML) = \frac{10}{\pi} 1.2^{2L-2} \left(\frac{3}{L+3}\right)^2 A^{2L-2} 2 \left(\frac{e\hbar}{2Mc}\right)^2 fm^{2L-2} \tag{2.27}$$

Table 2.1: Weisskopf single particle estimates for transition half-lives [28, 29]. The transition energies (E_γ) are in keV and A is the mass number.

Transition Multipolarity	$T_{\frac{1}{2}}$ (seconds)
E_1	$6.76 \times 10^{-6} E_\gamma^{-3} A^{-\frac{2}{3}}$
E_2	$9.52 \times 10^{6} E_\gamma^{-5} A^{-\frac{4}{3}}$
E_3	$2.04 \times 10^{19} E_\gamma^{-7} A^{-2}$
E_4	$6.50 \times 10^{31} E_\gamma^{-9} A^{-\frac{8}{3}}$
M_1	$2.20 \times 10^{-5} E_\gamma^{-3}$
M_2	$3.10 \times 10^{7} E_\gamma^{-5} A^{-\frac{2}{3}}$
M_3	$6.66 \times 10^{19} E_\gamma^{-7} A^{-\frac{4}{3}}$
M_4	$2.12 \times 10^{32} E_\gamma^{-9} A^{-2}$

2.5 The Spherical Shell Model

Two of the nuclei that are of interest to this work, ^{44}Sc and ^{42}Ca, are in the $A > 40$ and $A \leq 45$ mass region. The nearest inert core for nuclei in $A > 40$ and $A \leq 45$ mass region is the ^{40}Ca inert core. This doubly magic inert core with $N = 20 = Z$ is formed between $d_{3/2}$ and $f_{7/2}$ orbits see Fig.2.10. These orbits have opposite parities, which explains the behaviour of the magic number 20 against collective nucleonic excitations [30]. The shell gap at magic number 20 is an ideal testing ground for nuclear models since it is large enough to avoid coupling between single particle states and collective excitations at low energy.

For nuclei to be bound it is essential that the nuclear force should be stronger than the electromagnetic force. It is imperative to comprehend that nuclei may be described by an independent particle model in which nuclei are described in terms of a mean field in which weakly interacting particles move in orbits of a spherically symmetric nucleus [31]. This model is effective when dealing with a single nucleon outside the closed shell. When there is more than one nucleon outside the closed shell and residual interactions may not be ignored, the Spherical Shell Model (SSM) [32] becomes useful.

The existence of magic numbers in certain nuclei played a major role in the development of the shell model. As is well established in atomic theory, when certain shells are completely filled it results in an inert gas. In the atomic shell model, the shells are filled with electrons in order of increasing energy, consistent with the requirement of the Pauli's exclusion principle. This model

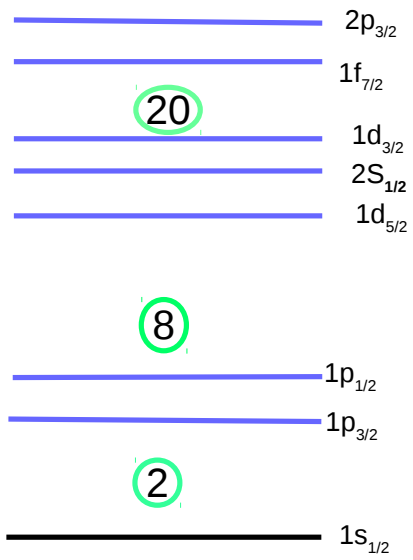

Figure 2.10: Experimental single-particle levels with magic numbers encircled in between them.

assumes that atomic properties are determined primarily by the valence electrons. One is able to see smooth variations of atomic properties within a subshell, however, as a subshell is completely filled and one enters the next subshell, sudden and epic changes are observed. Remarkably, some measured properties of atomic systems are in good agreement with the predictions of the model.

The SSM is critical in understanding how nucleons move in well defined orbits, even though a single nucleon can make a collision during each orbit. Nucleons, which are fermions, are governed by Pauli's exclusion principle. In atomic theory, electrons move freely in orbits which are occupied based on Pauli's exclusion principle. A single nucleon, on the other hand, can make a collision during each orbit. The fundamental assumption of the SSM model is that neutrons and protons move independently in an average potential, interacting with each other through a residual interaction of a two-body character. Under the assumption of a two-body interaction, the Hamiltonian describing the properties of a nucleon-nucleon potential can be expressed as [31]:

$$\hat{H} = \hat{T} + \hat{V} = \sum_{i=1}^{A} \frac{p^2}{2m_i} + \sum_{i>k=1}^{A} V_{ik}(r_i - r_k) \tag{2.28}$$

A reformulation of the nuclear potential was introduced by including a spin-orbit interaction term of the form $f(r)\hat{l}.\hat{s}$. This splits the high-j shells and squeezes the $\hat{l} + \hat{s}$ state down from a major shell N into the shell N–1, leading to the reproduction of all experimental shell gaps. That is, one assumes that the nucleus is a Fermi gas (as in atomic physics) in which nucleons occupy the shells

in increasing order up to the Fermi level [33].

Interactions between nucleons alters their occupation as a result of scattering. Moreover, residual interactions form an important fundamental base in which correlations, collectivity and configuration mixing happen which strongly influence nuclear structure. Shell structure is evidenced by the two-nucleon separation energy, which is the minimum energy to take two protons or neutrons out. In this instance, two nucleons are taken out in pairs to account for a term in the nuclear potential that favours pairing of nucleons. That nucleons can pair off in a closed shell, yields zero angular momentum and lowers the energy of a system.

The pairing interaction is only effective when the particles have extremely high spatial overlaps. The pairing interaction is attractive and is only effective for 0^+ states of identical nucleons in equivalent orbits [31]. The empirical evidence for pairing is prominent in even-even nuclei with spherical shape in which the large energy gap between the ground state and the first excited state is observed. Studying pairing correlations in the spherical shell model is advantageous since most of the interactions employed are adjusted to open shell nuclei. Another added advantage is the exact diagonalisation of the Hamiltonian matrix is done and the results obtained contain all possible correlations including pairing [34]. Other tools such as the Bardeen-Cooper-Schrieffer (BCS) [35] and the Hartee-Fock-Bogoliubov approximation [36] are essentially part of means where pairing interaction is studied.

Current models include:

(i) The triaxial projected shell model (TPSM) [37, 38, 39, 40, 34, 41]

(ii) The five-dimensional collective Hamiltonian (5DCH) based on the covariant density functional theory [42, 43].

(iii) Monte Carlo Shell Model (MCSM) [44]

2.5.1 Configuration mixing

In nuclear structure studies, a configuration is the group of states which can be formed by particles in orbits specified by n (principal quantum number) and l (orbital angular momentum) in the case of LS coupling or n, l and j (total angular momentum) in the case of jj coupling [45]. Each configuration consists of many different states. The absence of mutual interaction between configurations, making them degenerate, is the reason for grouping them under one name. The residual interactions between particles in different orbits are taken as the cause of configuration mixing. The portion of the interaction that is not absorbed in the central potential is referred to as

"residual", which results when there are two or more valence nucleons and the interaction between them, see Fig.2.11, has to be explicitly considered. There has been an increase on supporting evidence of configuration mixing in nuclear states. In seldom cases, two nuclear configurations of the same spin and parity cannot be described in terms of exactly pure configurations but rather linear combinations of two different configurations with wave-functions ψ_1 and ψ_2 [46]. These cases arise when there are different but close lying configurations of equal J. A strong configuration interaction may, therefore, be expected to arise because the finer details of interaction between nucleons are ignored in the zero-order approximation. Thus, deviations from the average central potential can be considered as a perturbation which mixes configurations [47]. Pairs that are shifted from one configuration to another will be mixed considerably. It is such mixtures that have the tendency to change the transition probability and when the states become "pure" that the transition probability may approximate closely its intrinsic value. A fair amount of mixing destroys the symmetry between particles and holes in a subshell below a magic number [47]. If the configuration mixing parameter is large enough, the levels of the two configurations are strongly mixed and an eigenstate from a given configuration could intrude into another resulting in a phenomenon called "Intruder States" [48].

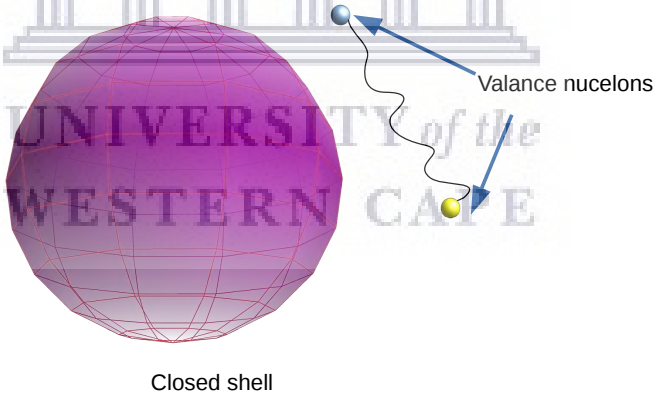

Figure 2.11: Nuclei with two or more valence nucleons will experience residual interactions. Here the sphere represents a closed shell with filled orbital and nucleons are represented by the small coloured circles. Residual interactions are due inter-nucleon interactions that are not part of the average potential.

2.5.2 Shell Model space

A model space is a truncation of the infinite set of orbitals to a finite set, with all operators normalized to account for orbitals that may have been left out. Truncation is introduced when

exact diagonalizations are impossible. One ought to bear in mind that the model space is a subspace of the full Hilbert space. To make up for those left out orbitals, an introduction, of effective operators which take care of the mixing of configurations that are explicitly included in the shell model calculations, is done. One would perceive that the chosen model space is a good approximation and that the neglected configuration mixing can be treated in perturbation theory [49]. If one considers effective interaction, the large space is reduced into a smaller model space by treating the coupling between them perturbatively. This transforms the full potential and its repulsive short distance in behaviour into a smooth pseudo-potential [50]. Nucleon-nucleon potentials reproduce nucleon-nucleon scattering data quite accurately. A major obstacle in shell model calculations is that all realistic nucleon-nucleon potentials have a strong repulsive core. This obstacle was, however, overcame by resorting to the Brueckner G matrix method, which was originally designed for nuclear matter calculations [51]. The operators are normalized by obtaining a G matrix type that takes into account short range repulsion which then is renormalized with perturbation theory to account for mixing of configurations beyond the model space. The single particle orbitals are defined by the active particles or holes that determine the properties at low energies when constructing a model scheme. The appropriate model space is found by looking at the experimentally observed states for a single nucleon outside the assumed inert core. Other factors that need to be considered include computational power and the shell gaps.

2.5.3 Shell Model calculations

Shell Model calculations prove to be paramount in extracting observable properties of nuclei such as spectroscopic factors, electromagnetic multipole moments and transition probability. In addition crucial information describing the fundamental behaviour of the nucleus (wave function, excitation energy, occupation numbers, and quadrupole moment) may be obtained from Shell Model calculations. Here the number of valence neutrons are fixed by selecting the nearest closed shells. The valence space is significantly important since it should reflect the basic physical fact: that the most critical components of the low-lying states of nuclei should be accounted for by many body states involving the excitation of particles in a few orbitals around the Fermi level [50]. With the rapid progress in computational capacity and numerical methods, precise $0\hbar\omega$ calculations can be achieved for nuclei in the pf-shell region. The $0\hbar\omega$ space is, conceptually, particles that are restricted to have the lowest possible values of p (the principal quantum number) that obey Pauli's exclusion principle. The $N\hbar\omega$ space (often referred to as no-core space) accounts for many body states that are allowed to have components involving basis states with up to N oscillating quanta

more than those pertaining to the $0\hbar\omega$ space. In its best form, the $0\hbar\omega$ space can only describe a limited number of low-lying states of the same natural parity [50]. The choice of a valence space is primarily informed by the physics involved in a particular system. When dealing with large complex spaces, one suffers from the center of mass problem. It then becomes prudent to prune the valence space as suggested by the Independent Particle Model (IPM). Other physical properties that affect the choice of valence space include collective motion, number of active nucleons and deformation.

Effective interaction:

Inevitably, when a model space is chosen, there will be "excluded" space as mentioned above. For this reason, an effective interaction is needed since it considers the "excluded" space while correcting for the bare Hamiltonian and other operators. Effective interactions are vital in Shell Model calculations in any means they are approached, be it phenomenologically determined interaction or empirical considerations (such as nucleon-nucleon interactions). By manipulating phenomenological and empirical considerations, one is able to parameterize an interaction that is comparable to the experimental one. This parameterization can be model dependent, e.g. delta-function interaction, or independent of any assumptions, e.g. two body matrix elements [52].
In these calculations, an interaction is expressed by the single particle energies (SPE) and two body matrix element (TBME) given by:

$$< ab \mid V \mid cd >_{JT} \tag{2.29}$$

where a, b, c, d are the single particle orbits V is an effective two body interaction
J and T are the spin and isospin of the coupled nucleons respectively. The Hamiltonian, together with the TBME and SPE are used to derive the effective interaction through a fit in experimental levels in a model space. The effective interaction should reproduce the eigenvalues of the original eigenvalues problem:

$$H \mid \psi_i >= E_i \mid \psi_i \tag{2.30}$$

where

$$H = H_0 + H_1 \tag{2.31}$$

and

$$H_0 = \sum_{i=1}^{A}(t_i + U_i) \tag{2.32}$$

$$H_1 = \sum_{i<j=1}^{A} V_{ij}^{NN} - \sum_{i=1}^{A} U_i \tag{2.33}$$

An auxiliary one-body potential U_i has been introduced in order to break up the nuclear Hamiltonian as the sum of a one-body term H_0, which describes the independent motion of the nucleons, and the interaction H_1 [51].

There are various means that effective interactions may be manifested including:

(i) Nucleon-nucleon interaction in free space

Here nucleons are perceived as non-relativistic particles interacting through a Hamiltonian consisting of two-body and higher potentials. The nucleon-nucleon potential is the significant and dominant one. Unlike free nucleon interaction, the nucleon-nucleon interaction is subject to Pauli's exclusion principle and is thus affected by the presence of other nucleons. Two interacting nucleons, as per Pauli's exclusion principle, may not scatter into states occupied by other nucleons. What also makes this interaction distinct from other free nucleon interaction is that a large part of it is absorbed into the mean field which is due to the average interaction between nucleons. Intensive studies have been undertaken to obtain a smooth realistic nucleon-nucleon potential and these are highlighted in detail by *Cagarrio et al* [51]. The first successful attempt to derive an effective interaction from free nucleon-nucleon potentials was in mid 1960s by Kuo and Brown [48]. The Kuo-Brown interaction is derived with no assumption from $0f_{1/2}$ to the higher pf shell orbits. Ongoing studies paved way to the development of potentials such as the Bonn [53] and Paris [54, 55, 56, 57] potentials. This led to renewed studies of the third and higher order contributions to the effective interaction. With the progress in practical application of the shell model with realistic effective interactions, more insight is obtained into the spectroscopic properties in various mass regions.

(ii) Virtual excitation from the inert core (closed shell) below the model space.

In nuclear shell models an assumption is made that the full description of a nucleus is an inert

core (closed shell) plus n valence nucleons. A strong binding energy gain resulting from collective correlation can overcome the energy gap of shell closures [50, 58, 59, 60, 61]. Core excitations are likely to happen at low excitations compared to those of valence excitations. This case presents itself when one type of nucleon has a closed or almost closed shell configuration, while the other type is at mid-shell [62].

It is possible to polarize a core by exciting one of its nucleons into a valence orbit, as depicted in 2.12, this results in effective interaction. A nucleon can create a bulge on the surface when polarizing a core. When a core is polarized, its quantum mechanical properties, such as angular momentum, parity and isospin, change. Through polarization effect of the proton core, a neutron which has no electric charge will be endowed with an effective charge.

(iii) Virtual excitations to orbits above the model space.

Contrary to energy conservation restraints, nucleons can scatter to higher states. This is explained in terms of the Heisenberg uncertainty principle. Energy violation are possible if they last for a short period of time. When there is more than one valence nucleon, they will interact and changes in configurations may happen since it is possible that particles can change their quantum numbers. Nucleons may be excited to orbits that are above the model space, see Fig.2.13 , thus cognizance need to be taken to account for such excitations. The excitations from the lower shells are included effectively by perturbation (-like) methods. Effective charges result from polarization effects in the nuclear core and from virtual excitation into higher orbits. These charges account for interactions with nucleons that would otherwise be neglected because of the inert core approximation [63]. Core-polarization interactions between the valence particles is strongly attractive and non-central. It produces effects that are quantitatively similar to paring-plus quadrupole interactions [64].

Fundamental procedure of Shell Model calculations:

In undertaking shell model calculations, the first important consideration is the nearest inert core or closed shell. By so doing, there is control over the number of single particle orbitals included in the model space and the number of valence nucleons. The single particle orbitals define the active particle (or holes) which determine the properties at low energy when constructing a model space.

A model space is set up as well as the configurations that span the space for each J^{π} value. The

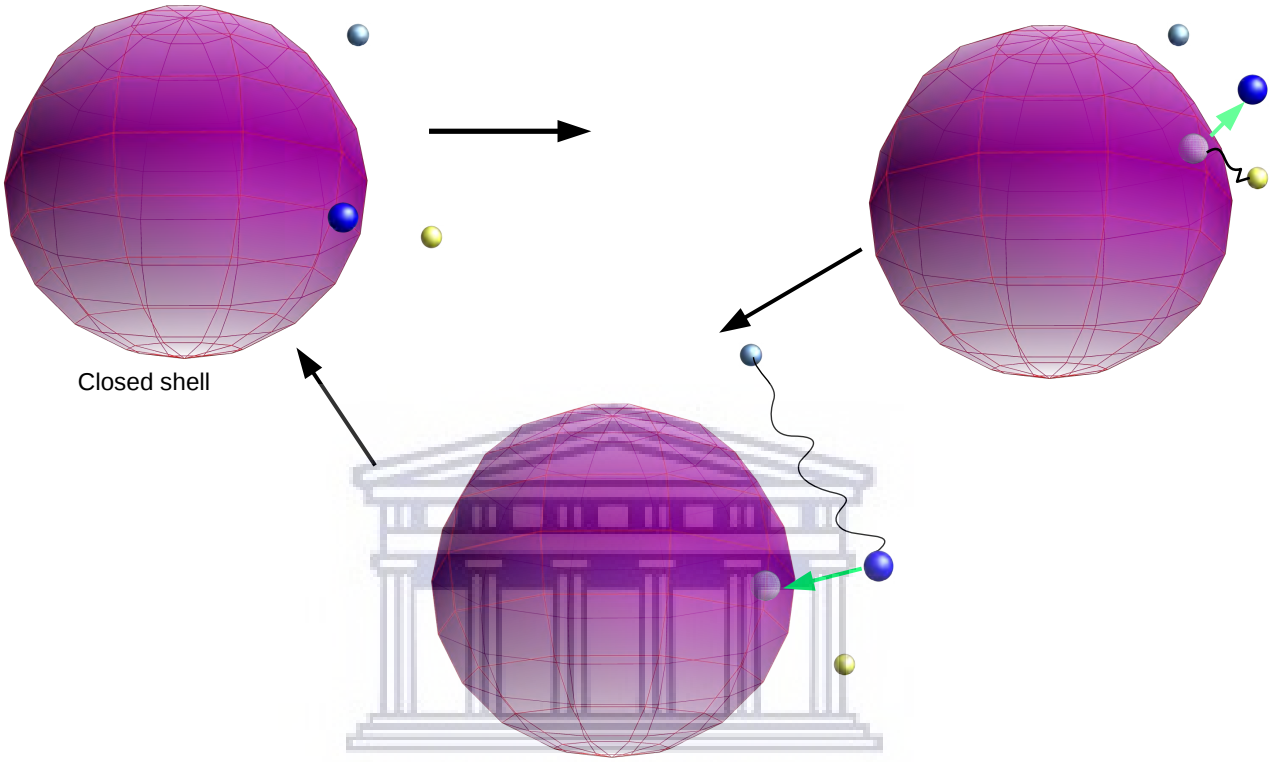

Figure 2.12: A schematic showing effective interaction. A nucleon can be excited into a valence space containing more than one nucleon. This is an important low-order core-valence interaction that happens through a G interaction with one of the valence nucleons. Subsequently, the excited nucleon can de-excite through interaction with the other valence nucleons.

model space should be tailored to study the desired properties of the system under investigation. Truncations may be made so that occupation numbers of certain orbits are limited with lower or upper bounds within the model space.

The energy matrix $[H_{ij}]$ is built by starting from single-particle energies ε_{jpi}, ε_{jni} and the two body matrix element for identical and non-identical nucleons. The two body matrix element can be written as:

$< j1, j2, J, T \mid V \mid j3, j4, J, T >$

and thus the Hamiltonian is expressed as:

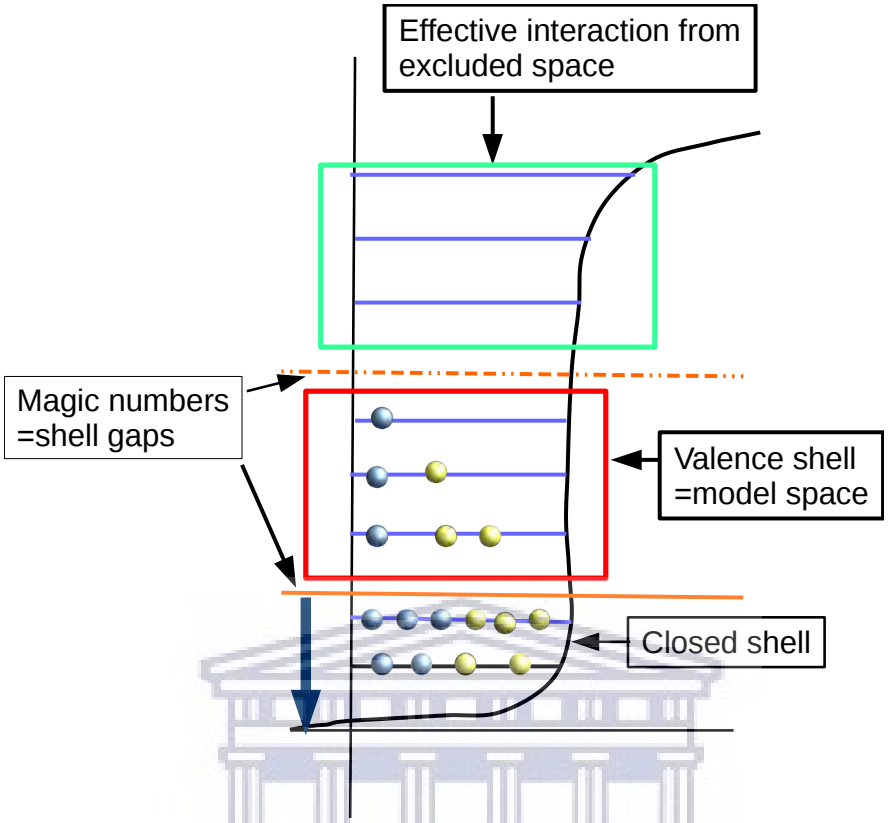

Figure 2.13: Effective interaction induced by excitations from higher orbits. The closed shell consists of fully occupied orbitals whereas the valence shell consists of partially occupied orbitals with nucleons moving around.

$$H = \sum_i \varepsilon_i n_i + \sum_{i,j,k,l} v_{ij,kl} a_i^\dagger a_j^\dagger a_l a_k \tag{2.34}$$

where i, j, k, l are single particle states. Knowing this, the matrix of the Hamiltonian H can be obtained and by diagonalizing H, one can achieve eigenvalues and wave-functions of good J values by superposing the Slater determinants properly.

From the wave-functions $\psi_i(J_i^{\pi i})$ and $\psi_f(J_f^{\pi f})$ physical observables are obtained and can be compared with existing data.

2.6 Intruder states

In any given model space, finite or not, it is inevitable to encounter states which are undescribed or experimental levels whose configurations are outside the defined model space. These states are called intruder states and the usually start at an excitation energy which is typical of the first

excited in closed shell nuclei. Orbitals involved in decoupled bands are usually high j, unnatural parity states, which "intrude" down from higher shell as a consequence of the spin-orbit interaction. If the intruder state has the same parity as the states in the model space, explicit mixing maybe important. Most intruder states are due to proton excitations which is a direct relation of a strong $p-n$ interaction in lowering these levels. Intruder state excitations energies are lowered relative to their unperturbed (no $p-n$ interaction) value. Because sufficient number of valence nucleons lead to more deformed shapes, intruder levels should be more deformed than "normal" levels [31].

2.7 Collective model

Away from closed shell, the interaction between valence nucleons leads to collective motion which represents a coherent motion of all nucleons and leads to deformation, vibrational and rotational degrees of freedom. Many of these collective properties are similar to those of a rotating or vibrating drop of liquid. Indeed, the Collective Model encompassed both the Liquid Drop Model and the Shell Model. It was introduced in its finer form by A. Bohr and B.R. Mottelson [65].

2.7.1 Rotational excitations

In a collective nuclear rotational motion, the nucleons move coherently around the axis perpendicular to the symmetry axis, as illustrated in Fig.2.14. Adding valence nucleons to spherical, closed-core nuclei breaks the spatial symmetry. The deformed nuclear potential can then undergo collective rotation, involving less energy than other degrees of freedom and thus dominates the spectrum of strongly deformed nuclei. Classically, the kinetic energy of a rotating object is $\frac{1}{2}\mathcal{J}\omega^2$ where $\mathcal{J}$ is the moment of inertia and ω is angular velocity. In quantum mechanics, the rotational Hamiltonian is

$$H = \frac{\hbar^2}{2\mathcal{J}}\mathbf{R}^2 \tag{2.35}$$

where $\mathbf{R}$ is the rotational angular momentum operator. Here the moment of inertia $\mathcal{J}$ depends on the shape and internal structure of the nucleus. If we assume that the ground state is $J^\pi = 0^+$, $K = 0$ and if all the angular momentum can be ascribed to rotation then the total angular momentum $J = \mathbf{R}$ we obtain the symmetric top rotational energy expression:

$$E_{rot}(J) = \frac{\hbar^2}{2\mathcal{J}}J(J+1) \tag{2.36}$$

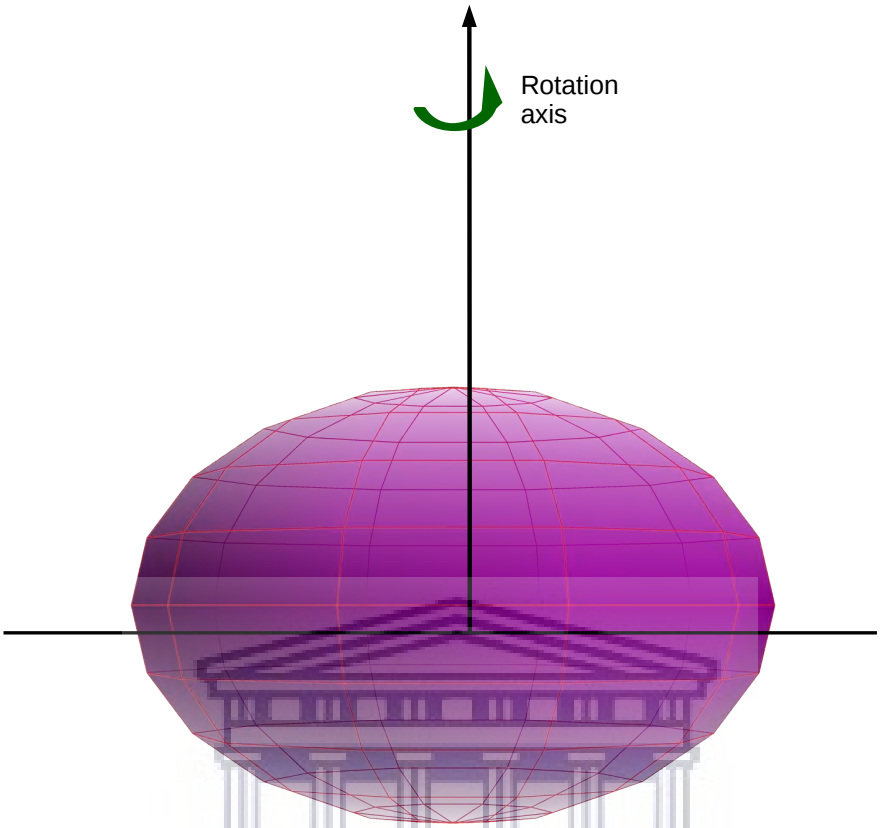

Figure 2.14: Schematic illustration of the collective rotation around an axis perpendicular to the symmetry axis.

where only even J are allowed [31]. Increasing the quantum number J corresponds to adding rotational energy to the nucleus and the nuclear excited states form a sequence known as a rotational band [22]. There are different types of rotational bands that are known and are dependent on the intrinsic nuclear configuration:

(i) ground state bands of even-even nuclei

These bands consist of E2 Transition and are built above the 0^+ ground state.

(ii) strongly-coupled bands

These bands reflect the rotation of a nucleus with one or more odd nucleons, when the single particle angular momentum j is coupled to the collective rotation of the nucleus.

(iii) decoupled bands

These bands reflect the rotation of a nucleus with one or more odd nucleons, for which the odd particles are decoupled from nuclear rotation.

Rotational bands with nearly constant moment of inertia can be found in the regions of well-

deformed nuclei. The rare-earth region of $A = 170$ is an example of such cases where these rotational bands are found.

2.7.2 Vibrational excitations

The deformed nuclear shapes arise because nuclei can lower their energy by rearranging their protons and neutrons into deformed shells that accommodate different number of nucleons.
The general shape of the nucleus can be expressed as:

$$R(\theta,\varphi) = R_0\left[1 + \sum_{\lambda\mu}\alpha_{\lambda\mu}Y^{\mu}_{\lambda}(\theta,\varphi)\right] \tag{2.37}$$

Where;
$R(\theta,\varphi)$ is the distance from the centre of the nucleus to the surface.
R_0 is the radius of the sphere of the same volume.
$\alpha_{\lambda\mu}$ coefficients are the amplitudes of spherical harmonics.
$Y^{\mu}_{\lambda}(\theta,\varphi)$ are the spherical harmonics.

Nuclei undergo collective vibrations about both spherical and deformed shapes. The degree of softness of these vibrations is characterized by the excitation energy required to populate states. Since the nucleus is not a rigid body, the surface can vibrate such that small deformations are induced [66]. Vibrational quanta called "phonons" of multipolarity, λ, carry the energy. Phonons of $\lambda = 2$ produce low-energy quadrupole vibrations, which can take two forms. The first, β vibrations, are shape oscillations directed along the symmetry axis, see Fig. 2.15 and are based on $I^{\pi} = 0^{+}$ states. This vibration preserves the axial symmetry and the angular momentum vector for such oscillations is perpendicular to the symmetry axis. A second type of quadrupole vibration produces oscillations in the γ shape parameter. The angular momentum vector of γ vibrations points along the symmetry axis which gives rise to bands based on $I^{\pi} = 2^{+}$ states. This vibration can be pictured as pulling in and out the sides of a rugby football, see Fig.2.14.
Octupole vibrations are associated with $\lambda = 3$ phonons, represented in Fig. 2.15. These oscillations are more difficult to visualize but they produce bands based on $I^{\pi} = 0^{-}, 1^{-}, 2^{-}$ and 3^{-} states. Although the $I^{\pi} = 3^{-}$ level is a purely octupole vibrational state, the bandheads are able to have angular momentum of less than 3 by coupling with the back rotating nuclear core [67]. A nuclear shape that lacks a fixed γ deformation but shows oscillations between all possible values of γ is called γ-soft. Such a nucleus is likely to vibrate.

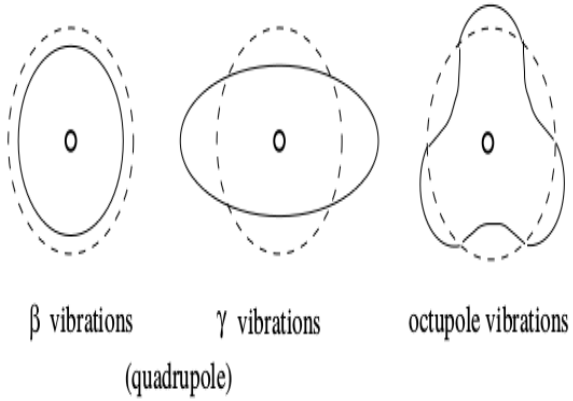

Figure 2.15: Diagram showing β, γ (quadrupole) and octupole vibrations looking along the symmetry axis. The dashed circle represents the cross-section of a non-vibrating, axially symmetric nucleus [67].

2.8 The Nilsson model

Far away from closed shells, residual interactions between nucleons can distort the nuclear shape away from spherical. When moving away from the closed-shell configurations, the level structure can become much more complex, with many levels closely located to each other. In such nuclei, the mixing among levels becomes important and the Fermi surface (i.e. the boundary between filled and unfilled states) can be deformed significantly. In nuclei, it results in dramatic consequences: the nuclei are indeed deformed in their shapes. A model that accounts for deformation of nuclei, like the Nilsson model, becomes of utmost necessity.

The Nilsson (or deformed shell) model [68, 69] uses a deformed potential instead of a spherically symmetric potential used in the shell model. Nilsson introduced the anisotropic oscillator potential to be used as a modified shell-model potential which reproduced well the single-particle states in deformed nuclei. This model provides a microscopic basis for the existence of rotational and vibrational collective motion that is directly linked to the shell model.

The Nilsson potential is based on the deformed harmonic oscillator potential for a spheroidal nucleus deformed along the z-axis, and can be written as:

$$V = \frac{m}{2}(\omega_x^2 x^2 + \omega_y^2 y^2 + \omega_z^2 z^2) + C\hat{l}.\hat{s} + D\hat{l}^2 \tag{2.38}$$

The $\hat{l}.\hat{s}$ term is the spin-orbit coupling term which is included to reproduce the observed major shell gaps at magic numbers. The first term is the deformed harmonic oscillator potential. The last term, which produces a more realistic potential, accounts for the fact that at large distance from the centre of the nucleus, nuclei experience a deeper potential.

2.8.1 Nilsson diagrams

The Nilsson levels are different in all aspects from the shell model states. Their prediction of energies, angular momenta, quantum numbers agree better with experimental data. Figure 2.16 shows how the Nilsson levels vary as a function of deformation. Each shell model of orbital angular momentum j splits into $j + \frac{1}{2}$ levels. Each level may contain up to two nucleons and form a rotational band. The solid lines represent even parity while the dotted lines represent odd parity. An important feature that arises from the Nilsson model is the energy dependence of the single nucleon on the projection of their angular momentum onto the symmetry axis Z, as shown in Fig.2.17. The energy levels in the Nilsson diagram are labeled by quantum numbers where: N is the total number of oscillator quanta, n_z is the number of oscillator quanta along the intrinsic symmetry axis, Σ is the projection of intrinsic spin and Λ the projection of orbital angular momentum along the intrinsic symmetry axis with $\Omega = \Sigma + \Lambda$. For each intrinsic deformed state selection rules exist for the asymptotic quantum numbers [70].

The main trends in the location of rotational bands can be understood from a consideration of available orbitals in a Nilsson diagram [68]. Since the lowest Nilsson orbits in the N = 82-126 shell are strongly down sloping as a function of deformation (Fig.2.18), a deformed minimum in the potential-energy surface eventually becomes energetically favoured for sudden onset of deformation. Detailed calculations correctly predict the onset of deformation between N = 88 and 90 and relate it to the occupation of the low-K orbits from the $h_{9/2}$ shell [71]. The Nilsson model has been successfully extended by introducing pairing, cranking, tuned interactions, larger bases, asymptotically correct potentials, and more complex shapes [71].

2.9 Lifetime measurement spectroscopy

Lifetime measurements can be undertaken through direct (e.g. fast-timing) or indirect means (e.g. Coulomb excitation). Indirect methods are called as such because they are inferred from a measure-

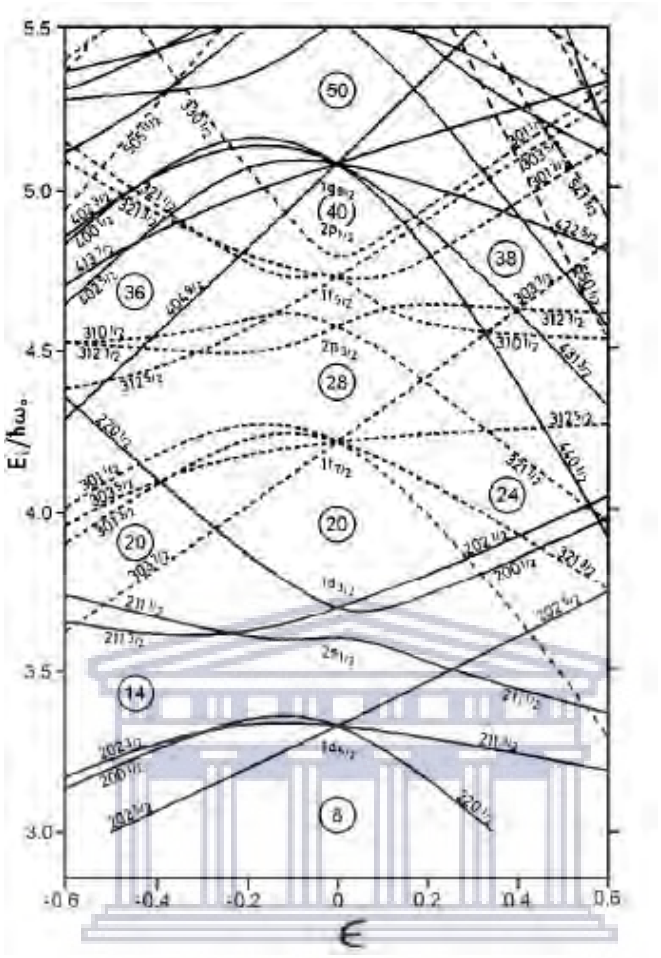

Figure 2.16: Nilsson diagram of energy levels (in units of $\hbar\omega_0$) as a function of a deformation parameter ε. The figures enclosed in circles along the centre give the neutron or proton numbers and l–j values of a single nucleon. Approximate quantum numbers are represented at the end of the solid and dotted lines.

ment of the width ($\tau = \hbar/\Gamma$) [24]. Some of indirect methods include Coulomb excitation, inelastic electron scattering and nuclear resonance fluorescence. In fast-timing, the time at which a state is populated and decays may be measured by the exponential decay law to obtain the mean lifetime.

One of the earliest techniques of measuring lifetimes is Doppler Shift Attenuation Method (DSAM) introduced by Elliot and Bell [72, 73]. Its effectiveness was later brought into limelight by 1954 by Devons [51]. In this method the γ ray at an unshifted energy and another at a shifted energy are observed. The Doppler shift is as a result of γ rays emitted while the nucleus is in flight when product nuclei are allowed out of the reaction target. The γ ray at an unshifted energy are formed when a nucleus in an excited state decays at rest. The lifetime of the level emitting a γ ray is compared with the slowing down time, approximately 3×10^{-13}s of a recoiling atom in a solid.

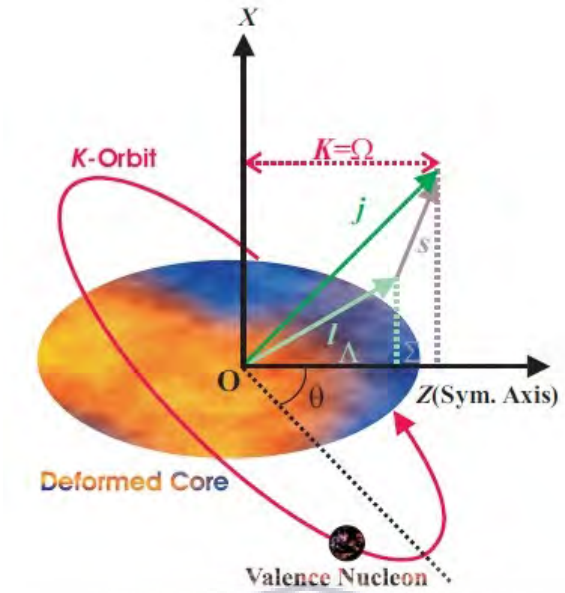

Figure 2.17: Graphical representation of a single particle orbit K at an inclination θ to a prolate deformed nucleus. Vector couplings of angular momenta are illustrated and their projection onto the symmetry axis Z define quantum numbers Σ and Ω.

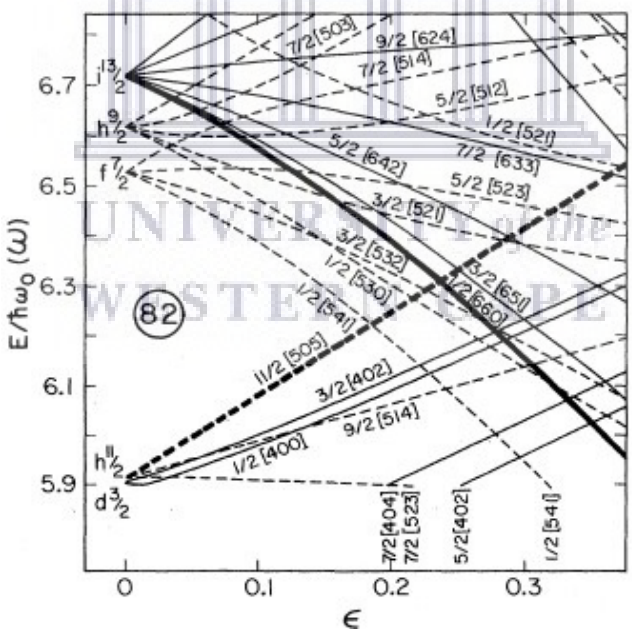

Figure 2.18: Portion of the Nilsson diagram for neutrons. The crossing of the $\frac{1}{2}[660]$ and $\frac{11}{2}[505]$ orbitals is said to be responsible for the low-lying 0_2^+ bands in the N = 88 and N = 90 rare earth region [70].

This slowing down is due to two physical processes;

(i) the excitation and exchange of electrons as the ionized atom of the recoil nucleus moves through

the stopping material.

(*ii*) the scattering of the moving atom by the screened Coulomb fields of nuclei of the atoms in the stopping material. The Recoil Distance Method (RDM) also uses a Doppler effect, however, here a thin target is used to prevent the slowing down the recoiling nuclei. This allows the recoiling nuclei to travel into vacuum whose distance is determined by the stopper behind the target. The ratio of the shifted and unshifted γ ray is measured as function of the stopper-target distance. In this method, the lifetime of the level emitting a γ ray is compared with the time taken for the recoil to travel in a vacuum between two foils separated by distances in the range $5\mu m$ to $2cm$. Lifetime techniques that utilize fast plastics only, were limited in their ability to carry out measurements in complex decay schemes. The reason is that, in spite of their sufficiently good timing resolution, these detectors have extremely poor energy resolution. Energy gates are selected from the Compton continuum since fast plastics do not record full energy peaks. The development of the BaF_2 scintillator, that has superior timing resolution, made it possible to measure lifetimes directly. This gave birth to direct measurement of lifetimes through electronic techniques which is also known as the fast-timing technique. One of earliest techniques used was the Fast Electronic Scintillation Timing (FEST) [74] and was commonly used in β-decay experiments. In this technique, time is measured between the emission of β-decay and the subsequent emission in the daughter nucleus. A method of using β-γ-γ coincidences was used effectively by [74, 75] to measure lifetimes for neutron-rich nuclei. In this method, timing information is obtained from $\beta - \gamma$ coincidence between a fast plastic scintillator and a BaF_2 crystal. The Ge-detector is used to select the desired decay branch through a coincident γ ray.

With the advent of $LaBr_3$:Ce scintillator detectors, analysis of complex decay schemes becomes possible since they have a better energy resolution than that of other scintillators [76, 77, 78, 79, 80, 81, 82, 83, 84]. The time resolution of the $LaBr_3$:Ce scintillator detectors is comparable to that of BaF_3. The $LaBr_3$:Ce is an inorganic crystal with an hexagonal (UCL3 type) structure with a P63/m space group [85]. The crystals are cerium Ce^{3+} doped thus producing luminescence in the blue/UV part of the electromagnetic spectrum (λ max = 380 nm) [76]. The crystal shape optimizes the solid angle thus improving light collection and time resolution. $LaBr_3$:Ce detectors vary in dimensions ranging from 1" by 1" to 3.5" by 8". Choosing the optimal crystal size is often challenging since a delicate balance has to be reached between the intrinsic time resolution and the detector efficiency. The intrinsic time resolution weakens with the increasing crystal size whereas the converse is true for detector efficiency. The different timing methods and the range of lifetimes that they can extract are depicted in Fig.2.19. Direct timing measurements down to a

few nanoseconds are possible with germanium detectors.

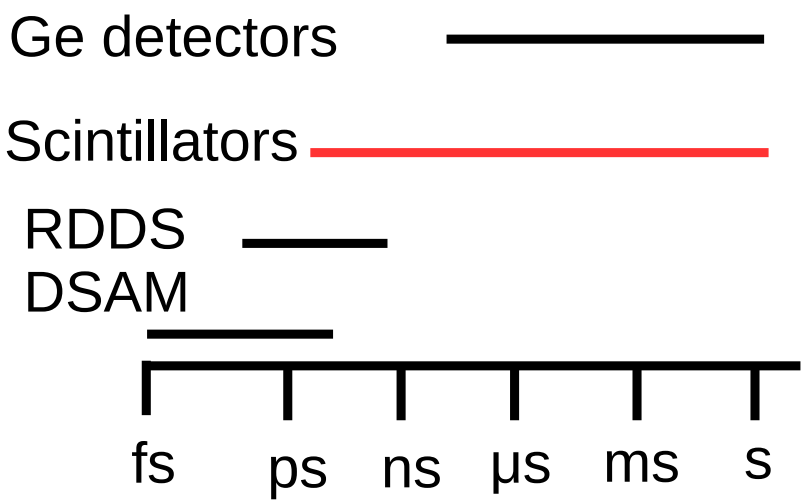

Figure 2.19: Lifetimes of excited states that can be obtained by different timing methods. The range that may be extracted by $LaBr_3$:Ce scintillator detectors is down to tens of picoseconds and is highlighted in red.

2.9.1 Direct transfer reactions

A direct reaction occurs, in general, if one of the particles in the initial two body interaction, involving the incident projectile, leaves the nucleus. There are two types of direct transfer reactions, illustrated in Fig.2.20:

(i) Stripping reaction - in which the incident projectile nucleus is "stripped away" such that the target nucleus absorbs part of the projectile. The remainder of the projectile continues past the target.

(ii) Pickup reaction - in which nucleons are "picked up' from the target and transferred onto the projectile.

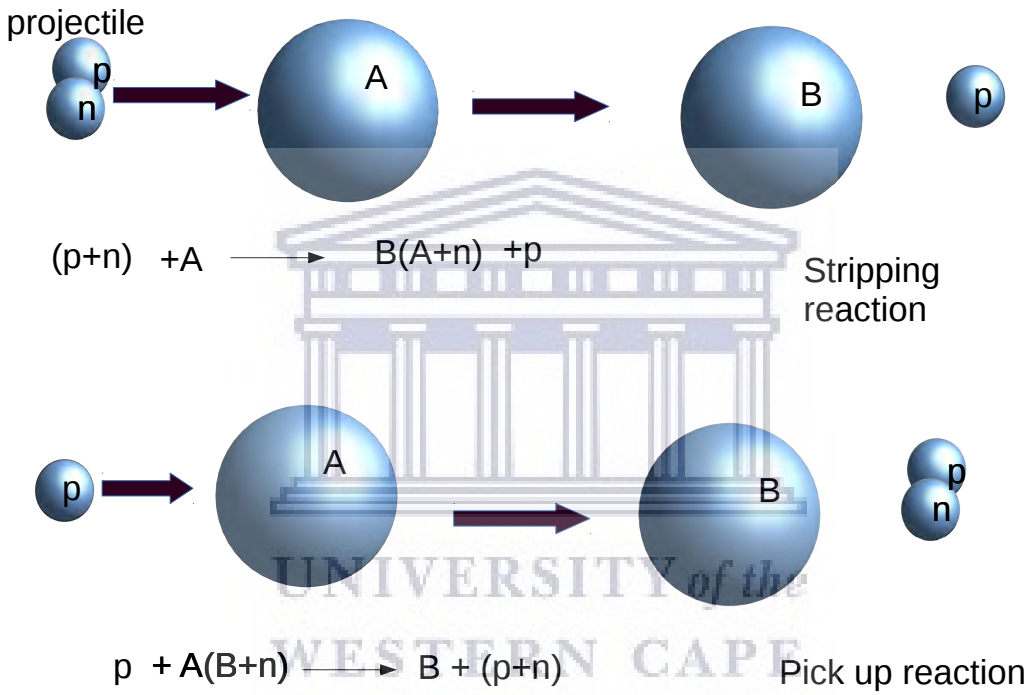

Figure 2.20: In direct transfer reactions an incoming projectile either sheds a nucleon which then binds to the target or picks up a nucleon from a target. The first is called a stripping reaction while the second is called a pick-up reaction.

Chapter 3

Experimental Techniques and Data Analysis

This work analyses two sets of experimental data that were all performed at iThemba LABS using the AFRODITE array [86]. The conventional AFRODITE array consists of HPGe clover detectors and LEPS detectors. Studying the complexity of nuclear spectroscopy, it is beneficial to broaden the scope of research by observing and consolidating the various aspects nuclear structure. It is for this reason that hybrid arrays, i.e. those arrays that consists of different types of detectors, are becoming increasingly popular. Progress in technology has led to improved scintillator detectors, with the more recent being $LaBr_3$:Ce detectors, as discussed in 3.3. The use of $LaBr_3$:Ce detectors in fast timing is conventionally done with analog systems. This work explores the function of these detectors with high speed digital readout electronics [87]. The detector geometry for the direct reaction and heavy ion fusion evaporation experiments conducted in this work is shown in Fig.3.1.

3.1 The ^{45}Sc(p,d)^{44}Sc and ^{45}Sc(p,α)^{42}Ca direct reactions

This is the first experiment, in which the recently commissioned 2" by 2" $LaBr_3$:Ce detectors were exposed to the beam for the first time at iThemba LABS. Six 2" by 2" $LaBr_3$:Ce detectors, together with two large volume 3.5" by 8" $LaBr_3$:Ce detectors were coupled to the AFRODITE array consisting of eight HPGe clover detectors see Fig.3.2. The S2 micron double sided silicon detector, with 48 rings and 16 sectors, was used in this work to build a particle identification telescope that consists of a thin energy loss stage in transmission geometry followed by a much thicker residual energy detector in which the particles are stopped. This particle dE-E telescope,

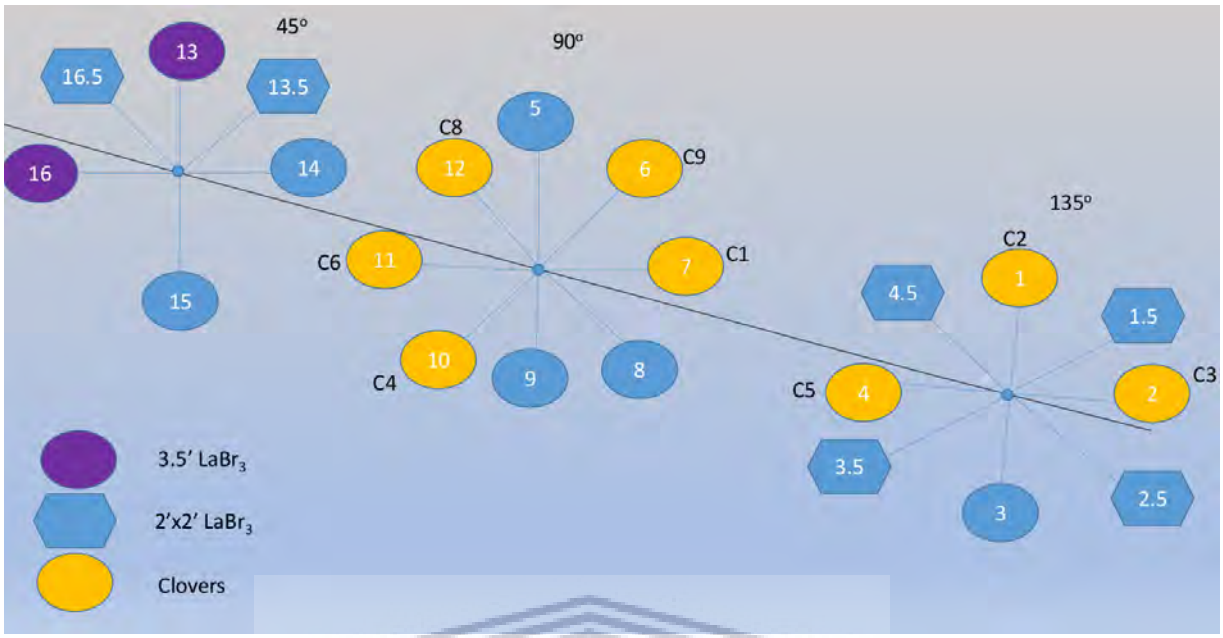

Figure 3.1: The geometry of the detector set up for the direct reaction and heavy ion fusion evaporation experiments performed in this analysis. The oval orange represents the position where the clover detectors where placed, oval purple represents 3.5" by 8" $LaBr_3$:Ce detector were placed and the hexagonal shape represents the 2" by 2" $LaBr_3$:Ce detectors. The oval blue shape represents the vacant clover positions.

useful in selecting a desired reaction channel, was inserted inside the target chamber, as shown in Fig.3.3. The nuclei studied in this work, ^{44}Sc and ^{42}Ca were populated through the ^{45}Sc(p,d)^{44}Sc and ^{45}Sc(p,α) ^{42}Ca reactions respectively with a beam energy of 27 MeV. The target thickness was 4.4 mg/cm^2 which is ideal for better statistics since, in general, targets $\geq$ 1mg/cm^2 increase the number of interactions between the beam and target particles leading to a higher event rate. This experiment makes it possible to get high quality results through the use of the different detectors that have excellent efficiency, energy and time resolution. In this chapter, we explore, partly, how each detector serves a specific purpose and the combined output of using the detectors together.

3.2 The ^{150}Sm(α,4n)^{150}Gd reaction

The second part of this work studies the nuclei in the much sought after rare earth region, namely ^{150}Gd. These nuclei were populated using the ^{150}Sm(α,4n)^{150}Gd fusion evaporation reaction. The target thickness was 2.2 mg/cm^2.

In a nuclear fusion reaction, a projectile nucleus fuses with a target nucleus thereby forming a compound nucleus with high excitation energy and angular momentum. The compound nucleus

Figure 3.2: The AFRODITE array consisting of HPGe clover detectors with BGO shields, large volume 3.5" by 8" $LaBr_3$:Ce detectors and medium sized 2" by 2" $LaBr_3$:Ce detectors.

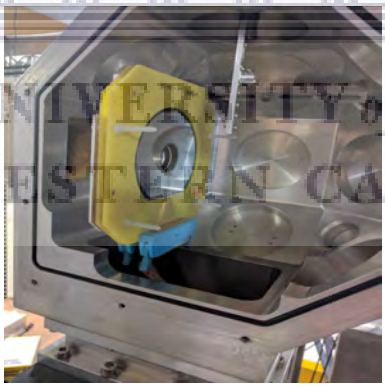

Figure 3.3: The S2 micron double sided silicon detector inserted inside the target chamber of the AFRODITE array.

decays by emitting neutrons and becomes a residual nucleus which decays emitting gamma rays, illustrated in Fig.3.4. In order to overcome the Coulomb barrier of a target nucleus, sufficient energy must be put into the system. It is for this reason that 48 MeV beam energy was used to populate medium to low states of ^{150}Gd. The Coulomb potential is expressed as follows:

$$V_{cb} = 1.22\frac{Z_b Z_t}{(A_b^{1/3} + A_t^{1/3})} \tag{3.1}$$

where Z_b and Z_t are the atomic numbers of the beam and target. And A_b and A_t are the mass number for the beam and target respectively.

The product Z_b Z_t will in the end appear in an exponential barrier penetration probability, so the fusion cross section is extremely sensitive to the Coulomb barrier [22]. Both energy and angular momentum are conserved in a fusion evaporation reaction. An added advantage of a fusion evaporation reaction is that it produces states that are oriented. Such states are very important for Direct Corelation of Oriented states measurements (DCO), ultimately one is able determine the quadrupole and dipole nature of a transition.

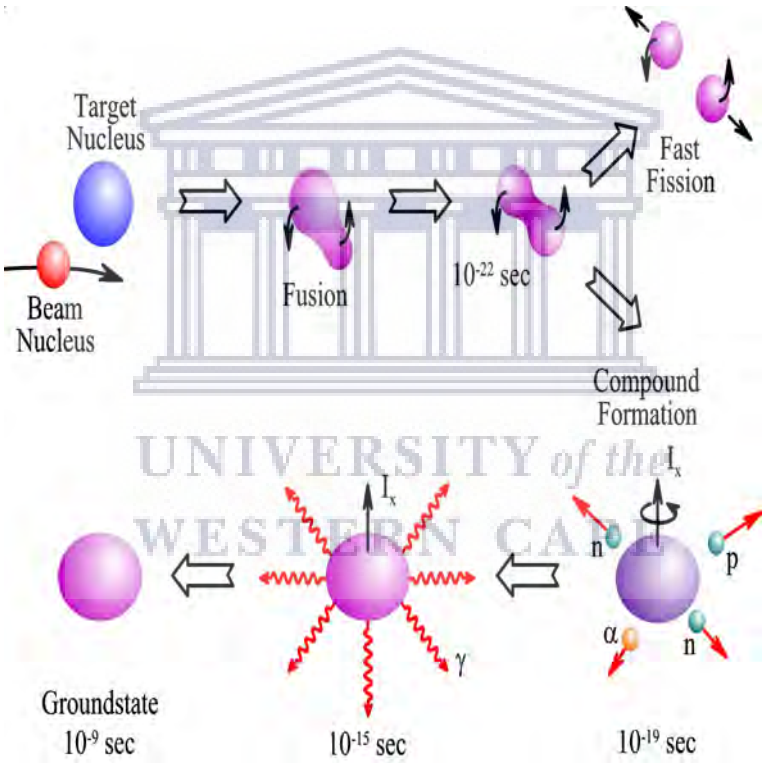

Figure 3.4: Schematic representation of a Heavy Ion Fusion-Evaporation (HIFE) reaction. The projectile fuses with a target nucleus and forms a compound nucleus at a high excitation energy and angular momentum.

3.3 Scintillator detectors

A scintillator is a luminescent material that converts energy lost by ionization radiation into pulses of light. The light output is proportional to the energy absorbed thus making scintillators an

apt tool for gamma spectroscopy when combined with a photomultiplier tube. It is desirable to have a high scintillation light output for good timing performance. Influential parameters that have dependence on the timing performance include, the number of photo electrons released at the photocathode, their time spread to the first dynode and the spread in the electron multiplier gain [21]. In the main, there are two types of scintillators organic and inorganic scintillators. For the purpose of this work, we discuss the inorganic scintillator more in depth.

(i) Organic scintillator

In this scintillator, the fluorescence process arises from the transitions in the energy level structure of a single molecule and therefore can be observed from a given molecular species independent of its physical state [20]. No crystal structure is involved in this type of scintillator.

(ii) Inorganic scintillator

The scintillation mechanism depends on the energy states determined by the crystal lattice of the material. In a scintillator, electrons can only occupy certain bands of energy. The valence band, as shown in Fig.2.4, represents those electrons that are bound at crystal sites while the conduction band represents those electrons that are free to migrate throughout the crystal. The forbidden band is found at the intermediate band of energies, where electrons are not found in the pure crystal. It is possible to ensure that the emitted photon is in the visible part of the spectrum. This is done by adding a small amount of impurities, called activators, to the inorganic scintillation crystal. This results in new energy levels to be created in the forbidden band of the pure crystal and the positive hole moves swiftly to the location of the activator, thereby ionizing it. The electrons can then drop from the conduction band into the activator energy states creating a neutral impurity configuration which has its own set of excited states. De-excitation of a photon will have high probability and can occur promptly for those activator states that happen to be in an excited state with an allowed transition to the ground state [20]. Different light emission of inorganic scintillator have different time characteristics and are classified into prompt fluorescence, phosphorescence and delayed fluorescence. It is mainly the prompt fluorescence that contributes to the output pulse since the time constants of measurement circuits are set much smaller than typical phosphorescence and delayed fluorescence decay times. When long-lived light (phosphorescence and delayed fluorescence) arrives at the light sensor, it is normally undistinguished from random noise [88].

3.4 Clover detectors

A clover detector is one type of a High Purity Germanium Detector (HPGe) used to detect high-energy gamma rays with energies above 300 keV. Semiconductors that are commonly used are silicon and germanium such as the HPGe. A semiconductor is a substance that has electrical conducting properties midway between a good conductor and an insulator. Both silicon and germanium have four valance electrons. They form crystals made of lattice atoms that are joined together by covalent bonds.

The clover detector consists of four coaxial n-type HPGe crystals, arranged like a four leaf structure, that are 0.2mm apart. As shown in Fig.3.6, HPGe crystals are 50mm in diameter and 70mm in length mounted together into a common cryostat. This arrangement allows for a large detector volume which alleviates some of the adverse effects of Compton scattering, by increasing the volume to surface area ratio thus reducing scatter out of the detector volume. These crystals are called elements of the clover detector. They provide a large photo efficiency as well as high multiplicity because of their granularity. To reduce the amount of material around the detector, it is held only by the rear side.

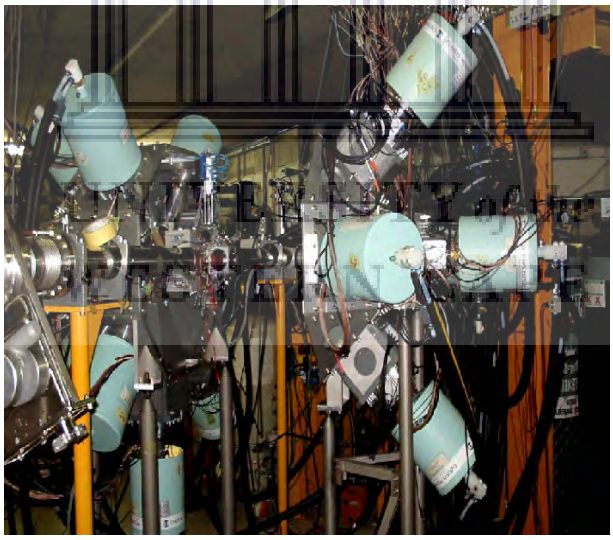

Figure 3.5: The AFRODITE array and its clover detectors and LEPS detectors.

3.4.1 Addback

Addback accounts for cases when a gamma ray deposits its energy onto a crystal and after scattering it deposits the rest of its energy into another crystal. The ratio of the photopeak and total efficiency (see Fig.3.7) is improved when the energies registered in each crystal are added if the scattered

events happen within a premediated time interval. Gamma rays with high energy are particularly prone to enhanced photopeak effect since low energy gamma rays have a low probability to Compton scatter.

The addback procedure depends on the scattering probability and a range of addback schemes is suggested for summing. For instance, if two neighbouring crystals are fired horizontally or vertically i.e. AB, CD or BD, AC (see Fig.3.8) the signals are added. Cases of diagonal scattering (AD or BC) and triple hits (ABD) or (ACD) are not accepted. Since these scattering probabilities are too small and such events mostly constitute of background.

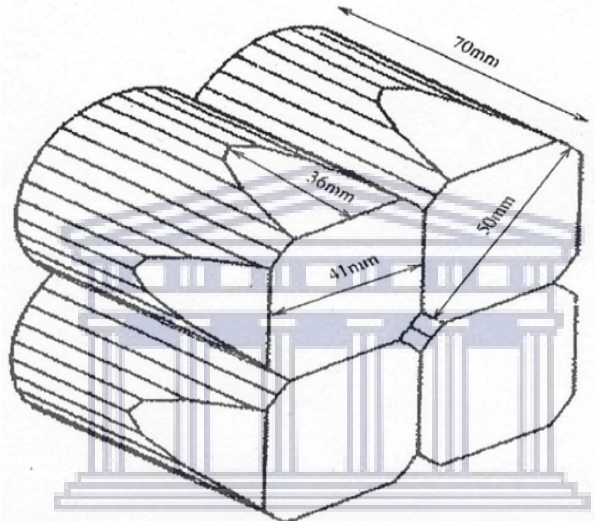

Figure 3.6: Drawing of a HPGe clover detector showing the shape and positioning of individual crystals [89].

3.4.2 Compton suppression

When a gamma ray Compton scatters, only a portion of the energy of the photon is deposited, contributing to unwanted background. A way of reducing this unwanted background, incurred due to multiple scatter events, is called Compton suppression. By making use of the bismuth germanate (BGO) shield, this unwanted background can be reduced, as evidenced in Fig.3.9. BGO surround HPGe detectors (see Fig.3.10) BGO shields are scintillation detectors that have comparatively low light output as opposed to other scintillators. They also have a high refractive index which makes light collection a challenge. It is for these reasons that they are best used for veto detectors for Compton scattered events. Heavy metal collimators are placed in front of the BGO detectors in order to prevent the detection of gamma rays which have not scattered from the Ge crystal.

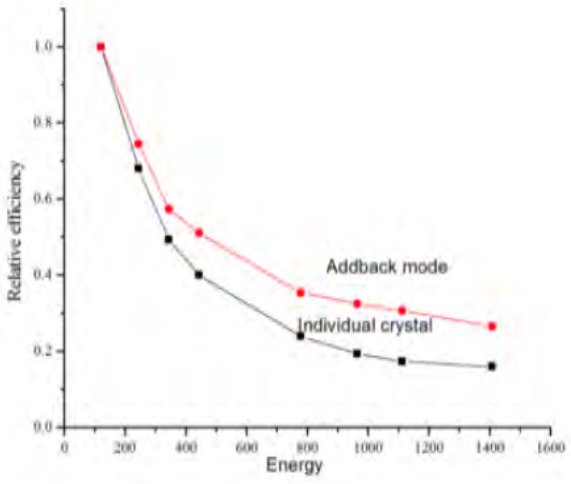

Figure 3.7: Relative efficiency as a function of gamma energy plot which shows that low energy gamma rays have a low probability to Compton scatter [90].

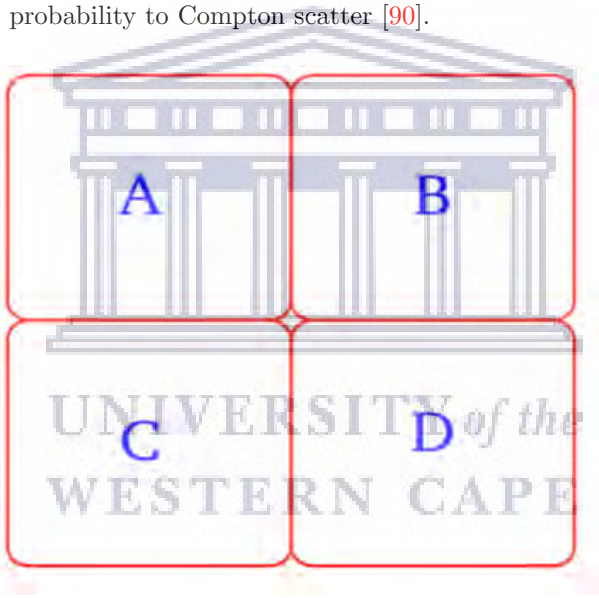

Figure 3.8: A schematic illustrating the four crystals of the clover detector.

3.4.3 Relative efficiency

The relative efficiency is the efficiency of detectors relative to one another. It is influenced by the type of detecting material, size and shape of a detector, the energies of the radiation, the distance between the source, and the medium between the source and the detector [92].

Efficiency calibration of the clover detectors was performed after the experiment using ^{152}Eu source. The source was placed at the target position. The relative efficiency (ε) of each detector was fitted using the Radware program *e*ffit [93] as follows.

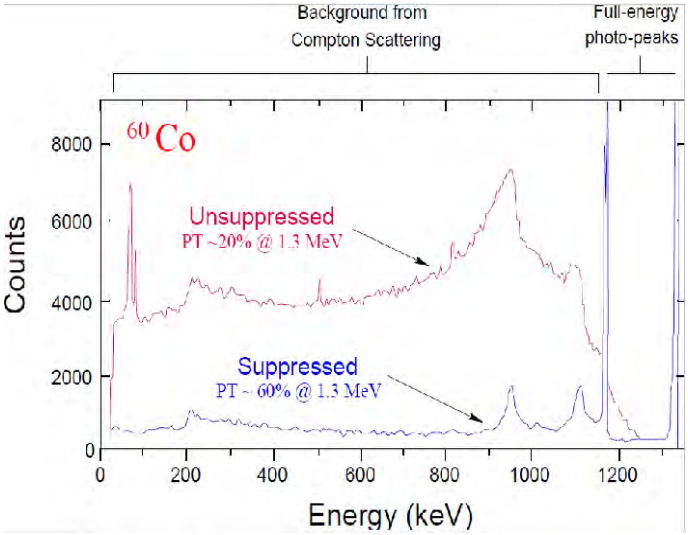

Figure 3.9: An illustration of how the use of a Compton suppression shield, such as the BGO, reduces the Compton background. The effects are clearly seen here for ^{60}Co spectra, with the Unsuppressed spectrum containing a lot of unwanted background while the Suppressed spectrum has little background [91].

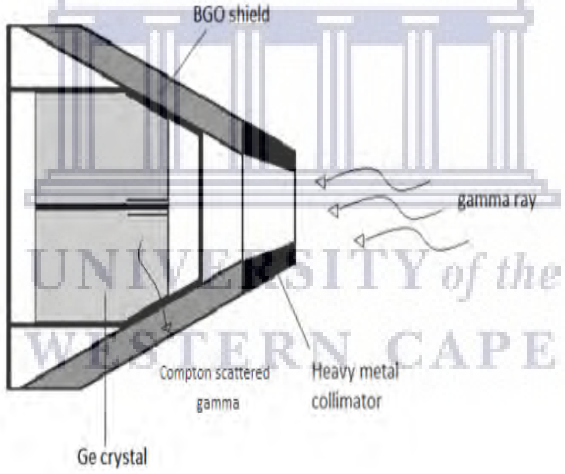

Figure 3.10: BGO shield with heavy metal.

$$ln(\varepsilon) = [(A + Bx + Cx^2)^{-G} + (D + Ey + Fy^2)^{-G}]^{-1/G} \tag{3.2}$$

where A, B and C describe the efficiency at low energies and D, E and F describe the efficiency at high energies. While G is an interaction parameter between the low and high energy region that determines the efficiency in the turn over region. The parameter x is given by $x = log(E_\gamma/100)$ and y is given by $y = log(E_\gamma/1000)$. The relative efficiency for the curve in Fig.3.11 was obtained

using the Radware Software effit program. Gamma rays escape from the detector before they can be fully absorbed resulting in an exponential drop in efficiency, see Fig.3.11.

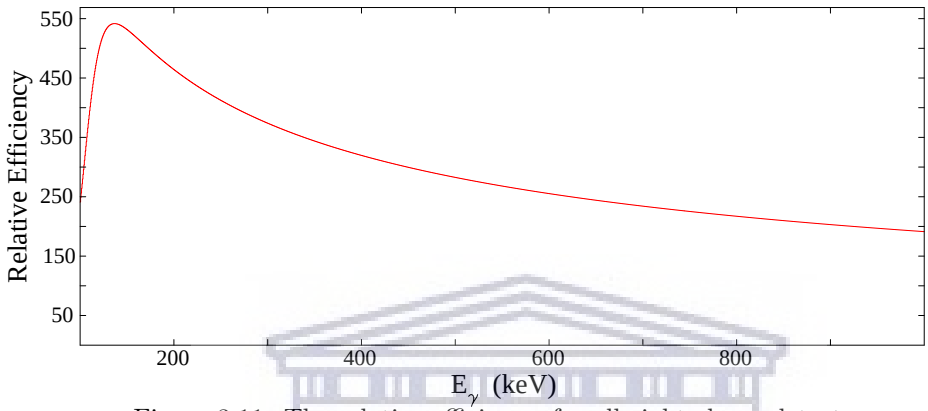

Figure 3.11: The relative efficiency, for all eight clover detectors.

3.5 Evaluation of different types of detectors

In this current work, the different types of detectors used helps us to comprehend how they are fundamentally different from one another. Indeed, one is able to see how each detector serves a purpose that is unique and combining these unique properties gives rise to a hybrid array. These hybrid arrays have launched a profound and broad perspective in gamma spectroscopy. Here the detectors used were the 2" by 2" $LaBr_3$:Ce detectors, 3.5" by 8" $LaBr_3$:Ce detectors and HPGe clover detectors as elaborated in Fig.3.2. In addition, the S2 micron double sided silicon detector was also used. The 2" by 2" $LaBr_3$:Ce detectors have been discussed at length in the previous sections. The 3.5" by 8" $LaBr_3$:Ce detectors are highly favoured for their superior efficiency and their ability to easily separate the full energy peak from the first and second escape [94]. Figure 3.12 shows the ^{60}Co spectrum collected with the different types of detectors used in this work. It is clear that large volume (3" by 5.8") $LaBr_3$:Ce detector has the largest efficiency followed and the medium volume 2" by 2" $LaBr_3$:Ce detector and the HPGe detector has the lowest efficiency.

The size of the crystal is influential in determining the ability of a detector to detect γ rays emitted. The larger the crystal the more it is able to detect photons with respect to the solid angle it subtends. *Nicolini et al* [94] simulated efficiencies for different sizes of $LaBr_3$:Ce detectors ranging

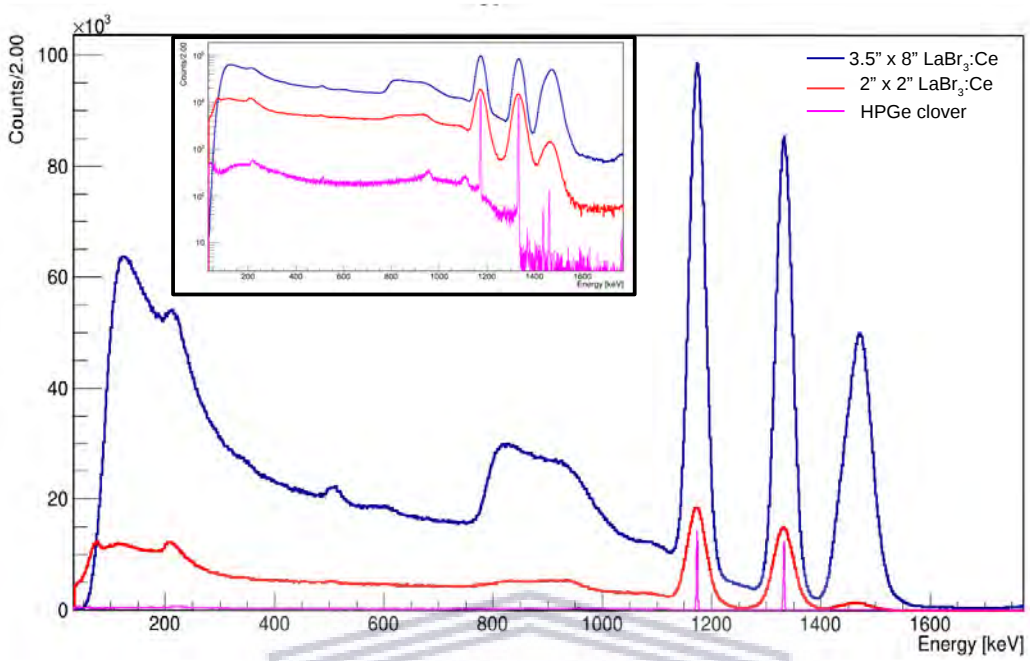

Figure 3.12: The ^{60}Co spectrum obtained from the different detectors. Evidently each detector has different capabilities from the other and combining them into a hybrid array high quality spectroscopic information is obtained. The peak at 1436 keV, from ^{138}La, is due to the internal radioactivity of the $LaBr_3$:Ce detector.

from 1" by 1" to 4" by 4" showing how efficiency increases with detector size. As highlighted in section 2.9 above, a compromise has to be reached between detector efficiency and time resolution when considering the crystal size. The rise and decay time pulses slows down with increasing detector size thus contributing to the detector performance. This may be due to the large spread in the collection time of the $LaBr_3$:Ce detectors-emitted photons at the PMT entrance window, as a result of longer light paths towards the photo-cathode [1]. Indeed, the average path length increases with detector size thereby impacting directly on the properties of the scintillator detector such as time resolution. While the efficiency of the $LaBr_3$:Ce detectors is higher than that of HPGe detectors, the energy resolution of HPGe detectors is much better than that of $LaBr_3$:Ce detectors. This is clearly visible in Fig.3.12 and it is these unique properties that combine to yield a comprehensive perspective on γ-ray spectroscopy. The energy resolution of the clover detectors is approximately 2 keV at 1332 keV while for large volume $LaBr_3$:Ce detectors it is around 3.0 % according to the manufacturer [76, 78] . The time resolution of the HPGe detectors is approximately 10 ns while *Giaz et al* [1] obtained a time resolution of about 1 ns for large volume

$LaBr_3$:Ce detectors.

3.5.1 The particle telescope

Direct transfer reactions may produce light particles that make it difficult to unambiguously identify the desired reaction channel. The S2 micron double sided silicon detector is based on ion-implantation technology. This is a compact particle identification detector that is easy to maintain. The bulk of the detector is n-type silicon and annular strips of p^+-type silicon are implanted on the front of the detector. The energy lost by a particle in the first telescope stage is denoted by dE, the residual energy measured in the second detector stage by E. The particle identification telescope made of dE-E detectors was mounted downstream such that the sectors of each detector are facing each other. The thickness of the dE detector used was 309μm and the thickness of the E was 1041μm . The ring side of the dE detector was facing the beam and the E-ring side was facing the beam dump. The distance from target to the front of the dE detector was 22mm and the distance from target front of the E detector being 26mm. These distances used made it possible to have an angular coverage was 26.7°to 53°. An aluminium foil was placed 2.5mm in front of dE detector as a shield from heavy particles. The particles we are interested in deposit energy up to approximately 30 MeV in the dE detector and up to around 20 MeV in the E detector. Test measurements were done with preamplifiers ranging from 20 MeV to 100 MeV in order to select the one that yields optimum results and has less signal-to-noise ratio. We have selected the preamplifier with the 25 MeV range since it satisfied our requirements. To remove with the background noise, the preamplifiers were grounded. The mass and the charge of the particle both influence the energy loss per unit length. This energy loss is best described by the Bethe-Bloch formula [92] which is euphemistically known as the stopping power. It expresses the passage of charged particles through matter. Figure 3.13 shows the plot of the energy deposited in the dE on the vertical axis and the energy deposited in the E detector on the horizontal axis. A simulation of the expected energies for a particle telescope with 284 μm thick dE detector and 996 μm thick E detector for a beam energy of 30 MeV is shown in Fig.3.14. The calculated ΔE E energy deposition was obtained using the SiRi kinematic calculator [95]

3.5.2 The $LaBr_3$:Ce detectors

Six 2" by 2" $LaBr_3$:Ce detectors with Brilliance:Ce-380 crystals, coupled to a R2083 photo-multiplier tube (PMT) were used. The Lanthanum Bromide material is cerium doped hence the notation $LaBr_3$:Ce and is an inorganic scintillator that is characterized by a high light output, fast

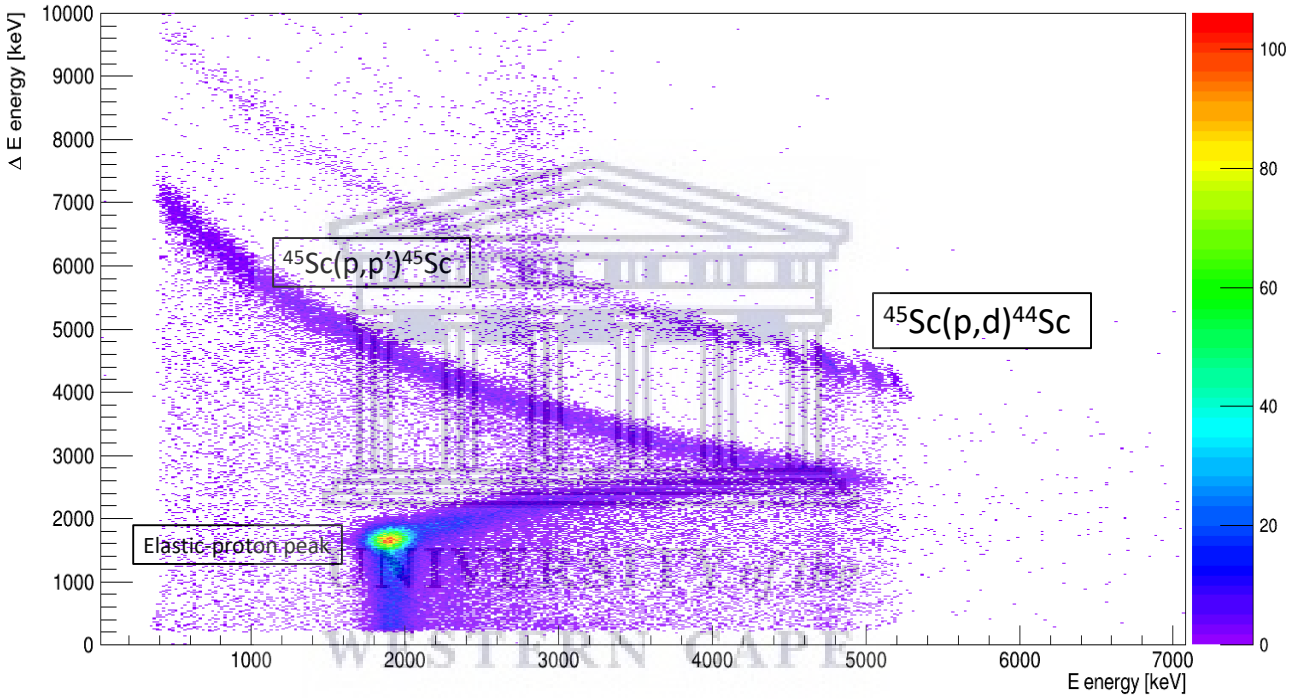

Figure 3.13: The Δ E vs E matrix obtained from the particle telescope. As each particle passes through the telescope it has a distinct banana shaped like distribution that makes it possible to distinguish the different particles.

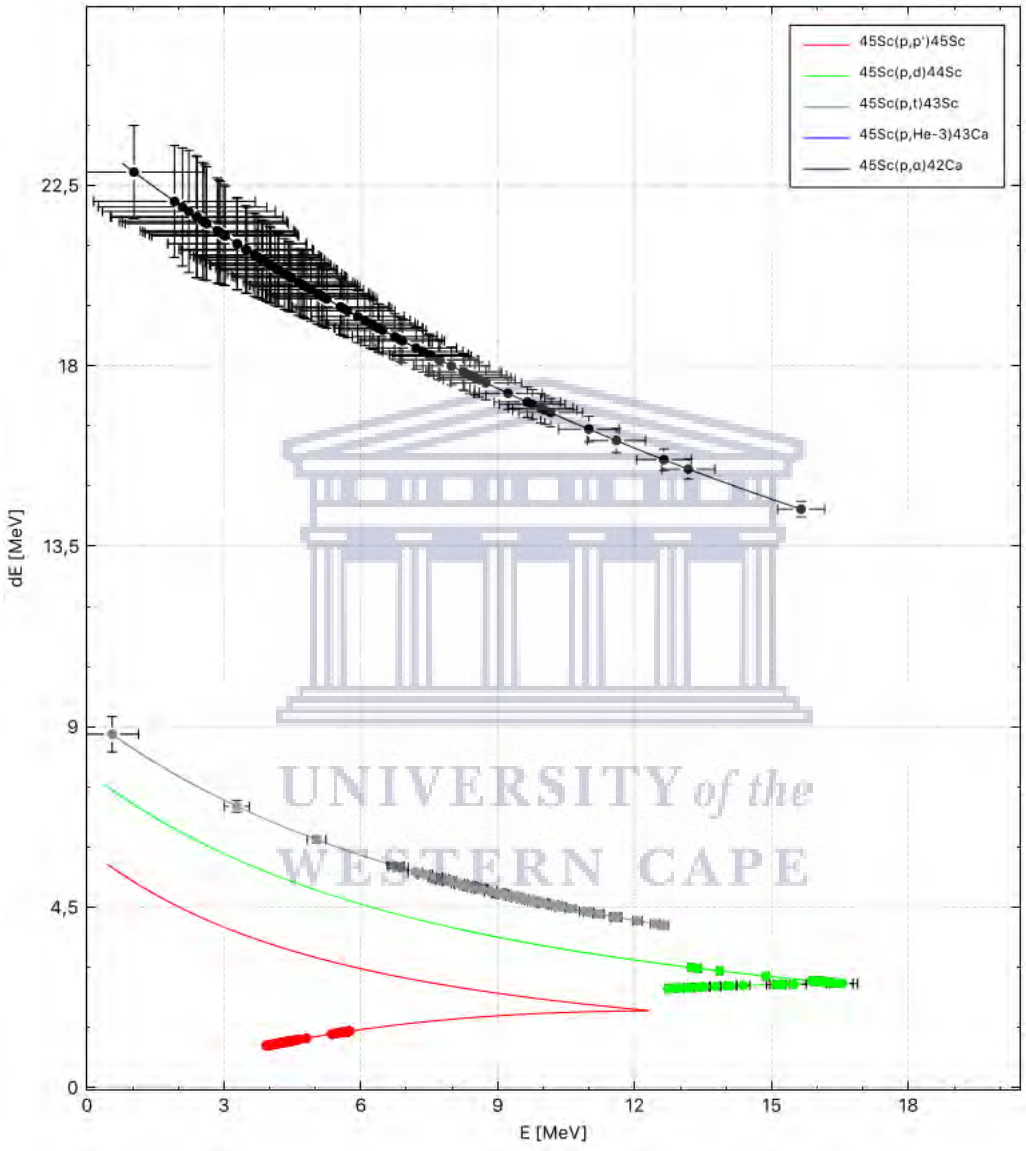

Figure 3.14: Simulations of the expected particle energies on a particle telescope showing the different reaction channels.

decay time output pulse. The number 380 (Brilliance:Ce-380) indicate the values of the wavelength of the emitted scintillation light [76, 78].

The $LaBr_3$:Ce scintillator have two types of output signals:

(i) The fast-timing output signal which is the anode of the PMT. This signal is connected to the input of the Constant Fraction Discriminator (CFD) to provide a timing signal which is related to the time of occurrence of the γ-ray detection.

(ii) A slower output (dynode), used to measure energy, whose output pulse is sent to the main amplifier for pulse height analysis.

The slow signals were incorporated in the first six channels of the 500 MHZ XIA digital acquisition card while the fast signals were incorporated from channel nine to fifteen. The aptly named pre-amplifier is provided to amplify the output signals prior to possible further amplification. It integrates the charged pulse and converts it into a voltage pulse whose amplitude is proportional to the energy deposited in the detector by the absorbed γ-ray. A high voltage (HV) is supplied to the PM tube base of the $LaBr_3$:Ce detector with the voltage difference to be applied across the cathode-anode. The advent of $LaBr_3$:Ce scintillator detectors has brought a better prospect than that presented by other scintillators such as BaF_2: and NaI detectors. In contrast to other scintillation detectors [76, 29, 79, 80, 81, 82, 83, 84] $LaBr_3$:Ce detectors boast of superior energy resolution. $LaBr_3$:Ce detectors have a higher detection efficiency due, partly, to their high density and high atomic number.

The crystal shape optimizes the solid angle thus improving light collection and time resolution. $LaBr_3$:Ce detectors vary in dimensions ranging from 1" by 1" to 3.5" by 8". Because of their fragile and highly hygroscopic nature, the detectors are always kept in a sealed capsules. Choosing the optimal crystal size is often challenging since a delicate balance has to be reached between the intrinsic time resolution and the detector efficiency. The intrinsic time resolution weakens with the increasing crystal size whereas the converse is true for detector efficiency.

3.5.3 Electronics of the fast-timing detectors

Advances made in gamma spectroscopy has launched a gateway into building and analysing complex decay schemes. The use of 2" x 2" $LaBr_3$:Ce array in gamma spectroscopy has proven to be an effective method for direct measurement of excited nuclear states lifetimes. These arrays are effective in measuring sub-nanosecond lifetimes, using γ-γ coincidence, over a wide range of

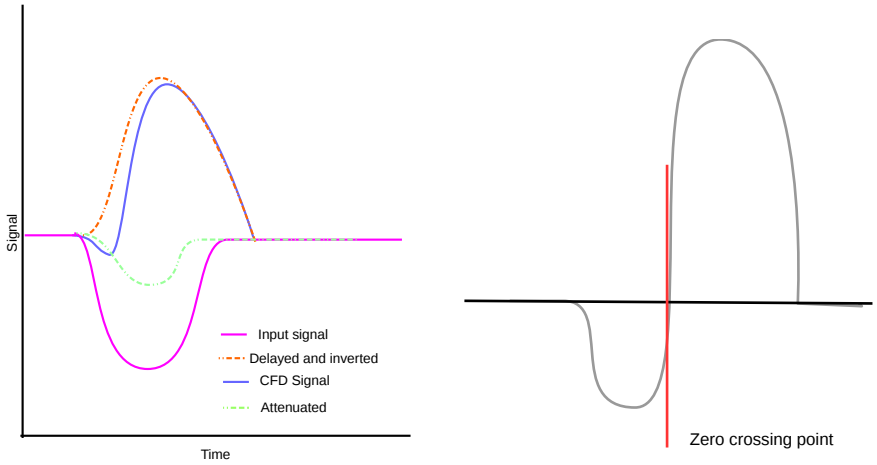

(a) (b)

Figure 3.15: (a) The CFD of the incoming signal is split into two "branches" such that one branch is attenuated and the other is inverted and delayed. The CFD signal is the sum of two branches and the CFD output signal will appear at the zero crossing of the CFD signal.
(b) The zero crossing point in which the output signal of the CFD is independent of the amplitude of the input signal and it is therefore not influenced by height of the input pulse, thereby reducing the walk.

energies [96, 97, 98, 99, 100, 101, 102]. The coincidence time window used in this analysis is 500 ns. Since fast-timing is a direct measurement of the lifetime through electronic techniques, two signals are essential. The first may be designated by a γ-ray that populates an excited state, the other is designated by the γ transition that depopulates the excited state and is the stop. To optimize the fast-timing set-up of this work various number of test measurements, adjustments of electronics, with different modules were performed.

The fundamental and essential parameter in fast-timing is the constant fraction discriminator (CFD). Variations in the amplitude and risetime of the incoming logic signal are minimized by the CFD. These variations, resulting from time movement of the output pulse relative to the input pulse, are known as the walk. The effects of the walk have a severely negative impact on the quality of the timing signal. Another stumbling block in the quality of the timing signal is the jitter which is the timing fluctuations caused by noise and statistical fluctuations originating from the detector signal. It is thus a challenge in fast-timing measurements to obtain a signal that is directly related in time to the event. The development of a trigger that will trigger at the optimum triggering fraction regardless of the input height is crucial. The CFD is a valuable tool to perform this function. Figure 3.15a shows how the input signal is delayed and a fraction of the undelayed input is subtracted from it to produce a bipolar pulse. One part is largely attenuated and is equal

to the time it takes for the pulse to rise from the constant fraction level to the pulse peak. The other is delayed and inverted. These pulses are then summed together and the zero crossing point is, see Fig.3.15b, taken as the starting point. The zero-crossing point is at constant fraction of the original height. The length of the delay between the attenuated and delayed inverted signal is adjustable using external cables of known delay length. The threshold voltage, delayed time and zero crossing are CFD parameters that can be easily adjusted to produce a reliable and trustworthy results. The threshold prevents triggering from the noise by ignoring signals below the said threshold. The adjustable zero crossing is detected by the CFD comparator which triggers the generation of the logic output pulse for timing.

The primary objective of the CFD is to minimize time-walk variations on the amplitude of the input pulse. This does not mean that the time-walk variations are completely done away with. The CFD, by virtue of its role in a fast-timing set-up, has a contribution into the time resolution of the fast-timing set-up. In principle, the best timing with very fast scintillator detectors is obtained for the "true-constant-fraction" (TCF) condition $t_d > t_r(1 - f)$ [103]
where t_d is the shaping delaying
t_r is the detector signal rise time and f is the attenuation factor, that defines the triggering fraction. This constraint ensures that zero-crossing time occurs after the attenuated linear input signal has reached its maximum amplitude.

Figure 3.16 and 3.17 below, illustrates how the CFD functions in the Digital Pulse Processing module (DPP) DGF-Pixie 16, 14-bit,500 MHz, XIA digital acquisition card. The CFD algorithm implemented in the field programmable array (FPGA) is unique for 500 MHz. This is because the ADC data coming into the FPGA is initially delayed and the FPGA then locates the CFD trigger point between two adjacent 2ns ADC samples. The CFD delay was set to 10 ns to optimize its response. The fast risetime was set to 0.10 μs and 0.02 μs for the slow and fast signal respectively. A more detailed explanation on how the signal is processed in the DGF-Pixie 16 XIA digital acquisition card is found in reference [104].
In the fast-timing environment, it is of utmost importance to achieve a clean signal with high quality. The 500 MHz readout electronics module, with the built-in CFD, is well suited for this purpose. The start and stop signal should be well separated and should be distinguished unambiguously. Since the decay of a quantum state of a system is governed by an exponential distribution towards a high decay time (stop), the lifetimes below the time resolution of a fast-timing set can

be measured [105].

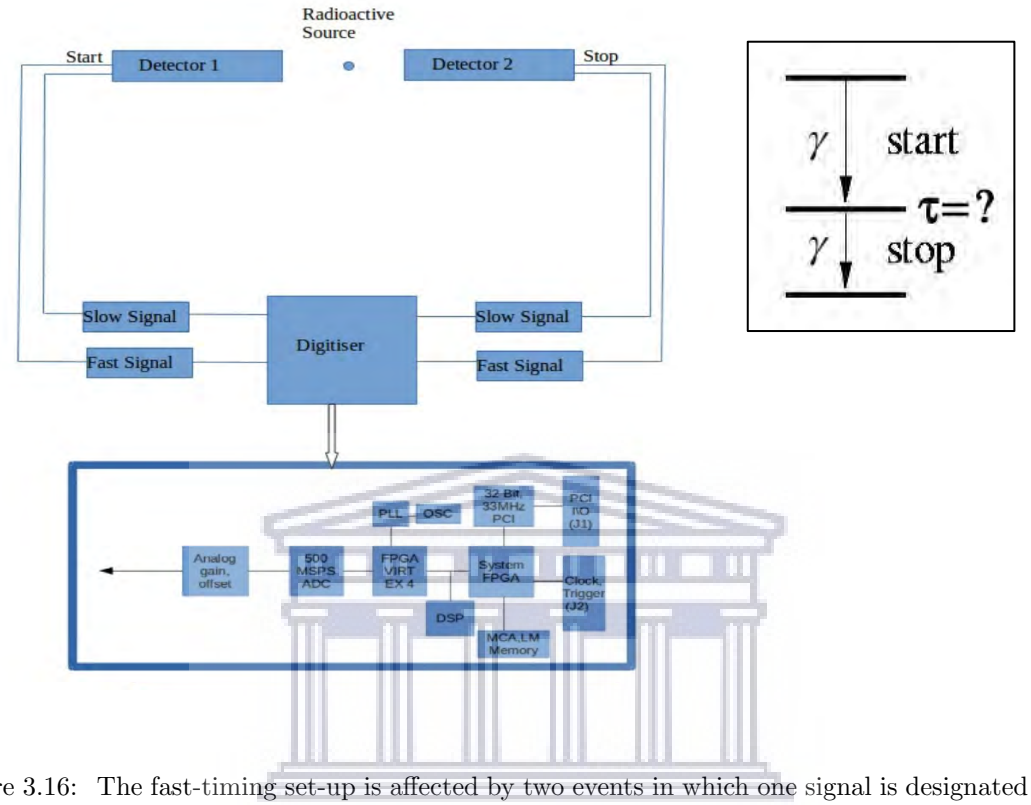

Figure 3.16: The fast-timing set-up is affected by two events in which one signal is designated the start and the other is designated the stop signal. The detectors are connected to a digitiser Pixie-16 card. RIGHT: The decay scheme illustrating the transition populating a state is designated the start while transition depopulating is the stop.

3.5.4 Time resolution

The time resolution of $LaBr_3$:Ce detectors is the single most significant factor that has direct bearing on the limit of the lifetimes that can be measured directly. The time resolution of a system refers to the smallest interval that can be measured with accuracy [92]. A delicate balance is needed when choosing the crystal size, since it deteriorates with crystal size. Another factor that affects time resolution is the operation voltage. It is therefore necessary to adjust the operation voltage such that the optimum operation voltage is reached since it affects both energy and time resolution. The operation voltages used in this work were around $\sim$ -1200 V. Reduction of the total PMT transit time spread is caused by increasing the PMT voltage. This results in an increase in gain and therefore a better time resolution. Added to this, the rise and fall-times of the $LaBr_3$:Ce detectors are inversely related to the voltage such that the intrinsic detector time resolution is

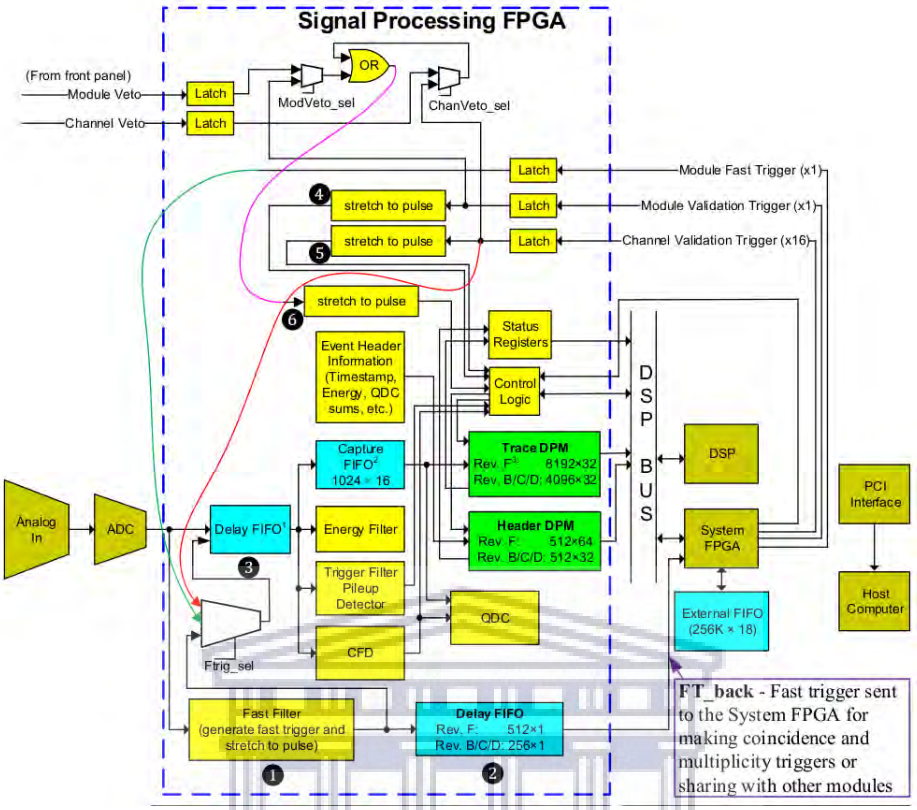

Figure 3.17: An illuustration of the timing algorithm and how the CFD is implemented in the Pixie 16 XIA digital acquisition card [104].

more easily achieved at higher voltages.

The intrinsic time resolution worsens with increasing crystal volume of $LaBr_3$:Ce detectors [76, 106]. The reason is two-fold [82] :

(i)Firstly, the rise-time of the average detector pulse increases, because of more light reflections inside the crystal and slower PMT rise-time.

(ii)Secondly, the individual pulse line shapes are subject to fluctuations because of the random light reflections.

In practice, an emission time profile of a scintillator can contain multi-time components with several different rise and decay time constants. For instance, combinations of two rise and three decay time constants were used to fit the emission profile measured from $LaBr_3$:Ce at different Ce concentrations [107]. In this case it is wise, therefore, to employ a method to include multi-time components using the calculated effective risetime constant and the decay time constant with dominant intensity [84].

To obtain the time resolution of a single detector in this current work, coincidence timing measurements of detector pairs were used. If one looks at a pair of detectors for example Detector 1 and Detector 2, the time resolution may be obtained using this relation:

$$\sigma_{total} = \sqrt{\sigma_{T1}^2 + \sigma_{T2}^2} \tag{3.3}$$

An assumption then made that in a fast-timing $\gamma-\gamma$ array the two detectors are identical such that $\sigma_{T1} = \sigma_{T2}$. To obtain the time resolution of a single detector, coincidence timing measurements of detector pairs were used for the prompt 1172 - 1332 keV cascade from the ^{60}Co decay. The timing resolution for the individual detectors ranged between 320 ps FWHM and 409 ps FWHM. The implementation of the CFD results in a channel width of 0.122 ps.

3.5.5 Energy resolution

In γ-ray spectroscopy, the energy resolution of a detector is crucial in order to be able to produce high quality results. This energy resolution is expressed in terms of the full width half maximum (FWHM). The resolution at energy E is defined as a ratio of the full width at half maximum (FWHM) and the centroid of the full energy peak ($Centr_0$) .

$$\frac{\Delta E}{E} = \frac{FWHM}{Centr_0} \tag{3.4}$$

The contributing factor of the good energy resolution of $LaBr_3$:Ce scintillator detectors is the high light output (47 000–63 000 photons per MeV [77]) Generally the energy resolution of a scintillation detector read out by a photomultiplier can be expressed as:

$$\frac{\Delta E}{E} = \sigma_{intr}^2 + \sigma_{tran}^2 + \sigma_{st}^2 \tag{3.5}$$

where σ_{intr} is the intrinsic detector resolution affected, as an example, by crystal inhomogeneities.

σ_{tran} is the transfer resolution that is correlated to the optical coupling properties of the crystal to the PMT readout, including the photocathode quantum efficiency as well as the focusing of photoelectrons to the first dynode

σ_{st} is the statistical contribution of the PMT [108].

Since the statistical uncertainty of the PMT is directly affected by the number of photoelectrons generated at the photocathode and the photoelectron collection efficiency at the first dynode, it is determined by the last two factors of equation 3.5 [109].

A ^{60}Co radioactive source was used in order determine the energy resolution and the parameters influencing the energy resolution were optimised and described in [87]. The energy resolution value obtained for the detectors is between 3.0% and 3.8% at 1332.5 keV. The manufacturer warrants an energy resolution of 2.8% at 662 keV. Furthermore, 2" x 2" $LaBr_3$:Ce detectors are said to have a 2.1% energy resolution at 1332.5 keV [110]. That our energy resolution is worse than what is warranted could be because of noise induced by electronics or mechanical vibration. The exact reason is, however, not known.

3.5.6 Photopeak efficiency

Because uncharged radiations such as gamma rays or neutrons must first undergo significant interaction in the detector before detection is possible [20], it is paramount to know the detection efficiency. Full energy peak efficiency is defined as the efficiency for detecting full-energy peak pulses only, rather than a pulse of any size for the gamma ray. To obtain the efficiency of each detector, the 2" x 2" $LaBr_3$:Ce scintillator detectors were placed equidistant from the source at 240mm in a set-up depicted in Fig.3.18. The full energy peak efficiency of each of the $LaBr_3$ detector calculated at 1.1 MeV and 1.3 MeV with a ^{60}Co source is shown in Fig.3.19. Evidently, the full energy decreases with an increase in energy, correlating with the emerging dominance of multiple interactions. These interactions include Compton scattering that contributes to the reduction of the photopeak energy. The initial activity of ^{60}Co is recorded to be 367.9 kBq according to information supplied by the manufacturer. During the measurement, ^{60}Co the activity was equal to 68.2 kBq. The full energy peak efficiency was corrected for the radioactive decay through this relation:

$$k_\lambda = e^{-\lambda t}.\frac{(1 - e^{-\lambda \Delta t})}{\lambda \Delta t} \tag{3.6}$$

where k_λ is the radioactive decay correction , λ is the radioactive decay constant for the nucleus of interest, t is the time difference from the reference time and Δt is the acquisition time.
$(1 - e^{-\lambda \Delta t})/\lambda \Delta t$ gives the decay correction during the measurement period (183 minutes).

The total peak efficiency of the array of eight 2" by 2" $LaBr_3$:Ce detectors was found to be 0.28% $\pm$ 0.0013 at 1332 keV with a point source placed 240mm from the face of detectors. Several factors influence the efficiency of detectors including the solid angle and the properties of a detector crystal. Studies [81, 82, 111, 112, 83, 94] undertaken on $LaBr_3$:Ce detectors have shown that its

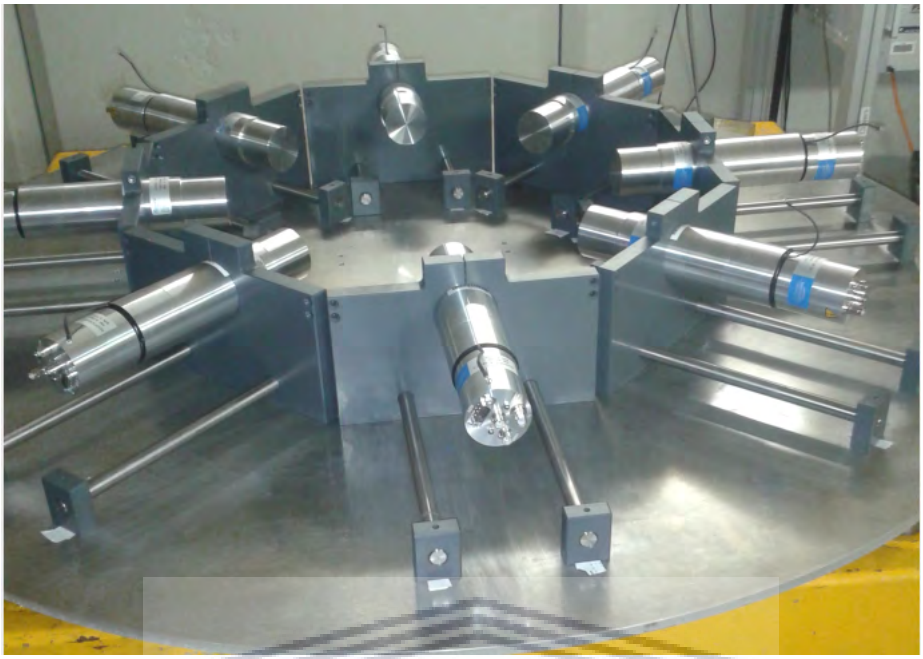

Figure 3.18: An array of 2" x 2" $LaBr_3$:Ce scintillator detectors commissioned recently at iThemba LABS.

high density and high atomic number result in higher detection efficiency. A fast-timing array must subtend as much solid angle as possible to fulfil its function as a reliable and effective spectrometer. The size of the detector itself also affects its efficiency as demonstrated by Nicolini et al. [94], through a simulation of different sizes of $LaBr_3$:Ce detectors. The results show that with an increase in detector crystal the efficiency increases. Studies done on the smaller 1" by 1" $LaBr_3$:Ce [113, 114, 115] crystal has yielded a lower efficiency. Roberts *et al* [116] performed a simulation of five 2" by 2" $LaBr_3$ detectors and found the full energy peak efficiency of a ring of detectors to be approximately 3.1% at 1000 keV at 83 mm from the face of the detectors.

In γ-ray spectroscopy, it is desirable to be able to detect gamma rays with energies up to 4 MeV, which is the energy expected to be emitted by a magic or semi-magic nuclei [117].

3.5.7 Energy calibration of $LaBr_3$:Ce detectors

The ^{152}Eu source was to calibrate both $LaBr_3$:Ce and HPGe clover detectors because of the wide energy range that it covers corroborates the energies of interest for the current work. The ^{152}Eu source is also used for the calibration of the Prompt Response Difference (PRD) curve as will be

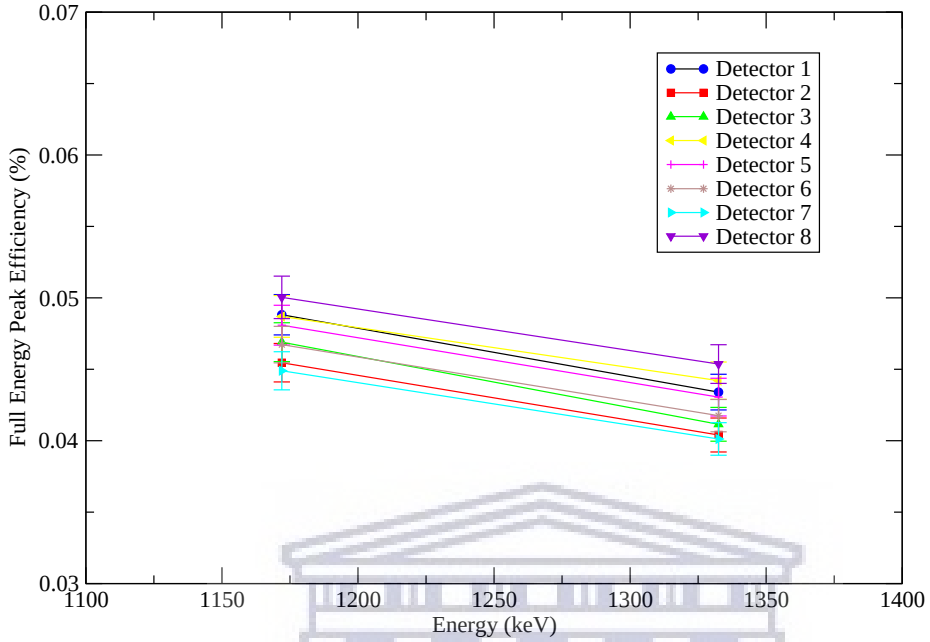

Figure 3.19: Full energy peak efficiency for all eight 2" x 2" $LaBr_3$:Ce scintillator detectors obtained from a ^{60}Co radioactive source placed at 240mm from the face of the detectors as shown in Fig.3.18. The lines are drawn to guide the eye and do not represent any fit.

discussed later. The $LaBr_3$ detectors were calibrated using a third order polynomial of the form:

$$E = ax^3 + bx^2 + cx + d \tag{3.7}$$

where a, b, c, d are the gain matching coefficients. E is the energy and x is the channel number of the original spectrum. Six energy peaks, see Fig.3.20, spanning a region from low to high energies, were used for calibration of $LaBr_3$:Ce detectors. These peaks were fitted and the relevant peak centroids and their uncertainties were taken into account so that each point has an associated weight. Figure 3.20 illustrates how the third order polynomial calibration is more accurate than the first order polynomial. A first order calibration of 2" x 2" $LaBr_3$:Ce detectors was used by reference [118].

Evidently, from Fig.3.20, the third order provides a great improvement on the calibration and even the third order coefficient, as small as it may be, has a positive impact on the fit.

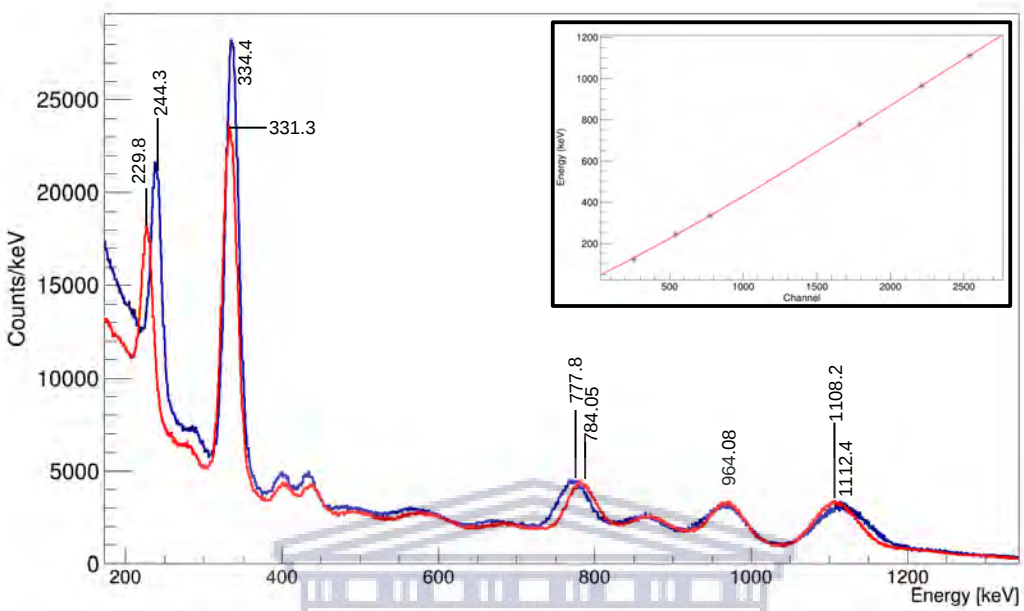

Figure 3.20: The ^{152}Eu calibrated spectrum. The red spectrum was calibrated using a first order polynomial while the blue spectrum was calibrated using a third order polynomial. INSERT: The six energy peaks used to calibrate the $LaBr_3$ detectors with the original energies taken from ENSDF [119].

3.5.8 Synchronization and aligning of time distributions

In this work, detectors that were used include the particle telescope, HPGe clovers and $LaBr_3$:Ce detectors all forming part of an hybrid array. All detectors were incorporated to DPP modules, inserted into two crates. A crate or bin accommodates nuclear electronics in standard modules such that they occupy the full 19 inch relay rack [20]. The particle telescope and the HPGe detectors were incorporated into the 100 MHz, XIA digital acquisition card while the $LaBr_3$ detectors were incorporated to the 500 MHz card. Since the 500 MHz digital acquisition card, by the virtue of its timing properties, sets the clock for other cards, it has to be placed on the first module of the crate. The first crate was fully occupied since it housed the particle telescope and the HPGe detectors. The second crate was used to accommodate the 500 MHz digital acquisition card in the first module. A shift between the detector channels by $\sim$ 2 ns in the 500 MHz card results in the signals to become time shifted by an arbitrary amount in multiples of clock units, see Fig.3.21, whenever a data acquisition system is stopped and resumed again. Looking at each detector pair,

it is evident that the time difference spectra is shifted between run number 1 and run number 2. To correct for this effect, the centroids of the time distributions were determined in order to observe how the signals were shifted during the start and stop process. The energy-independent centroids give constant shift_{ij} values that were arranged in a matrix form, $i \times j$, for each time the data acquisition system was stopped between runs. The matrix elements $i \times j$ were arranged as 6×6 elements such that $\text{shift}_{i=j} = 0$ and $\text{shift}_{ij} = \text{-shift}_{ji}$. This correction is vital in obtaining accurate lifetimes as 3.22 illustrates, how the energy vs time matrix looks before and after the correction.

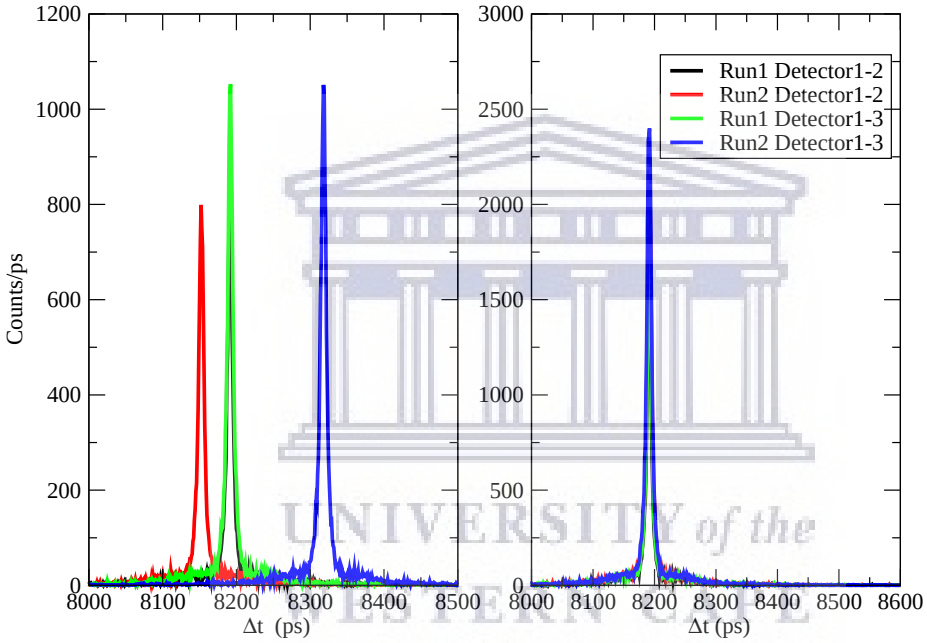

Figure 3.21: Left: The time difference spectra between two detector combinations $i\_j = 1\_2$ and $i\_j = 1\_3$ for run number 1 and run number 2.
Right: The aligned time difference spectra for detector combinations $i\_j = 1\_2$ and $i\_j = 1\_3$ for run number 1 and run number 2.

.

In the fast-timing method, it is critical that measurements are done with much precision as possible. This means that any slight offset between different detector pairs, must be corrected for. This is done by aligning all detector pairs that will be combined to produce a PRD curve, from which sub-nanosecond lifetimes are determined. Figure 3.23 illustrates how the different detector pairs have their own offset. The ^{152}Eu source was used to obtain the time distributions To align all the pairs we fitted the centroids of the time difference between the detector pairs and used the

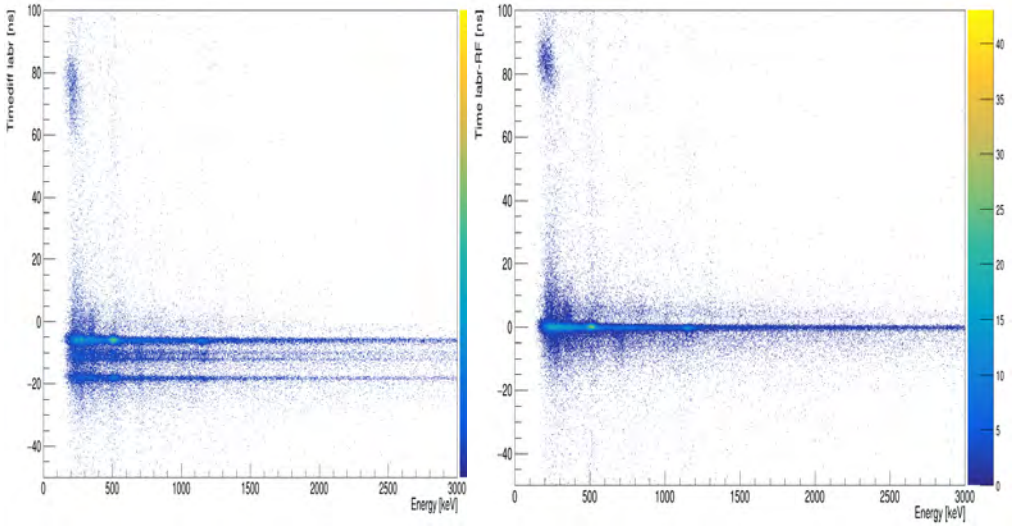

(a) (b)

Figure 3.22: (a) The energy vs time matrix, (from which lifetimes are extracted), without the correcting for the shift between the detector channels. Here it is apparent how the signals are time shifted by an arbitrary amount in multiples of clock units when the data acquisition is stopped and started.
(b) The energy vs time matrix corrected for shift between the detector channels. This single distribution makes it possible to determine lifetimes accurately.

centroids as shifts such that the time spectra are aligned to zero picoseconds.

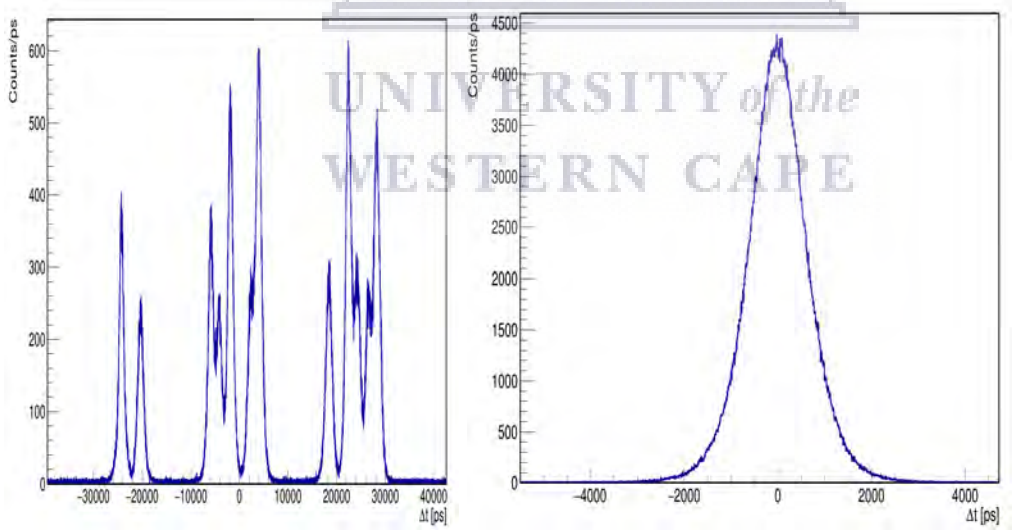

(a) (b)

Figure 3.23: (a) Unaligned time distributions of different detector pairs and their respective offset.
(b) Aligned time distributions of detector pairs.

3.5.9 Time-walk characteristics

Time-walk refers to the inherent variation in delay of the discriminator itself and it is measured with a step function input pulse at the discriminator input [120]. In any $\gamma - \gamma$ fast-timing set-up, the time-walk must be taken into account failing which a degradation of the time resolution is expected. Such a degradation is caused by the superposition and symmetrization of the time-difference spectra of all detector pairs of the set-up. Section 3.5.3 discusses how the CFD minimizes the time-walk and yet time-walk is still evident in a fast-timing array despite the presence of a CFD. Essential to obtaining accurate lifetimes of excited nuclear states is the ability to employ a walk-free signal. The inherent variation in the delay of the discriminator results in time-walk and may affect the quality of the signal. For scintillator detectors, it is not good practice to ignore the time-walk as it may lead to adverse effects on the time resolution of a fast timing array. Various methods may be used to correct for the time-walk of a detector [77, 121, 122, 123], to optimise the input signal. Systematic errors should not be underestimated in a real γ-γ set-up which is asymmetric. Applying a higher PMT operation voltage can reduce the time-walk non-linearity yet this can drive the energy response of the PMT into non-linearity [124].

In executing fast timing measurements, it is necessary to comprehend the dependence of the time response as a function of energy. Moreover, when measuring lifetimes in the sub-nanosecond range, the centroid shift method may be invoked. Characteristics of the energy as a function of the centroid position's prompt time distribution describes the time-walk characteristics. The interplay of the shape of the detector output pulse and the timing principle result in the prompt response function [124].

A ^{60}Co radioactive source was used in this work to investigate the effects of the time-walk. The purpose here, is to illustrate the characteristic Compton response of the setup. One γ-ray detector is gated upon constantly on a transition while other detector selects coincident prompt transitions of different energies so as to obtain a walk-free reference timing signal. Figure 3.24a illustrates that time walk characteristics when the start detector is gated on the 1173 keV and 334 keV. In order to obtain the centroid position over a wide range, 10 keV wide gates, in increments of 20 keV, were gated on the stop detector. The 1173 keV populates the 1332.5 keV in the β-decay ^{60}Co radioactive source. For comparison, a gate was set on the 344 keV which is an essential reference energy describing the prompt response function as elaborated by J.M. Régis *et al* [125]. Similarly, gating the stop detector 1173 keV and 334 keV the fits as represented Fig.3.24b were obtained.

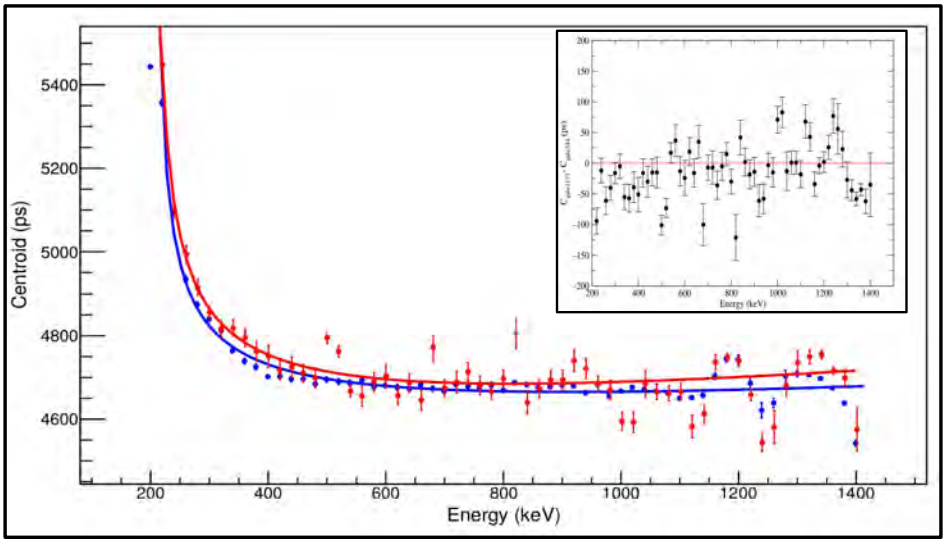

(a)

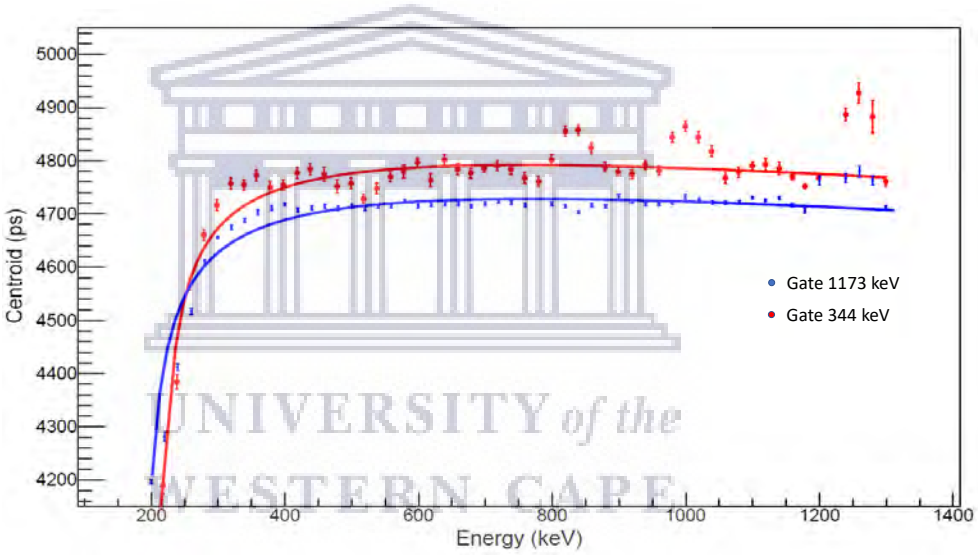

(b)

Figure 3.24: (a) The energy dependency of the centroid position of the prompt time distribution obtained from gating the start detector on the 334 keV (in red) and 1173 keV (in blue) transitions of the ^{60}Co source. This investigation was done as sum of combinations for the eight 2" x 2" $LaBr_3$:Ce detectors. INSERT: The residual of the data points for both fits. No significant difference between the two fits is observed. (b) The gate is now set on the stop detector on the same transitions. The fitted data points in red are for gates set on the 344 keV transition and those in blue are for the 1173 keV transition. This is shown to represent the characteristic Compton response of the set-up.

The time walk characteristics displayed are similar to those demonstrated by J.-M. Régis *et al* [125]. Below 300 keV a delayed structure, which may be a result of Compton events, is observed. The 1173 keV gated centroids show an invariable continuity up to about 1200 keV and from then a structure is visible, possibly emanating from Compton events.

N. Marginean *et al* [96] used a second order polynomial to correct for the time-walk, resulting in an optimum time resolution. The centroids shown in Fig. 3.24a, were fitted using:

$$C(E_\gamma) = \frac{a}{\sqrt{b + E_\gamma}} + cE_\gamma + d \tag{3.8}$$

following parameters were obtained for the 1173 keV gated on the stop (3.24b):

a = -707.1 ± 36.39 $ps\sqrt{keV}$

b = -251.5 ± 0.8006 keV

c = -0.01664 ± 0.003134 ps/keV

d = 4764 ± 4.181 ps

For the energies between 340 keV and 1300 keV, the statistical uncertainty is 26 ps corresponding to a deviation 1σ.

3.6 Lifetime measurements techniques

The data of this experiment was collected using the iThemba LABS Digital Data Acquisition System. The data was sorted into two hours run enabling the user to inspect the quality of the data collected as the experiment progresses. MTSort [126] was employed to perform online and offline data analysis. The software ROOT [127] was used for offline analysis as well, in particular to analyze the $\gamma - \gamma - \Delta T$ cube. The cube $\gamma - \gamma - \Delta T$ makes it easier to be able to set gates, perform projections and fit spectra. Figure 3.25 shows how the x and y axes are the energy gates from which start and stop signals obtained and the z axis is the time-difference. There are various methods and techniques that may be employed to obtain lifetimes of excited nuclear states. The direct measurement of lifetimes is limited by the detector resolution of the fast-timing set-up. Below is the different techniques and their respective limitations.

3.6.1 The slope method

This method is employed when the lifetime of interest is much longer than the detector resolution of the fast-timing array. Setting a gate on the transition that feeds directly onto the level of interest, as a start signal and the one that decay from it as a stop, a time spectrum that represents a decay according to the exponential law, equation 2.23, is obtained. By way of elaborating this method,

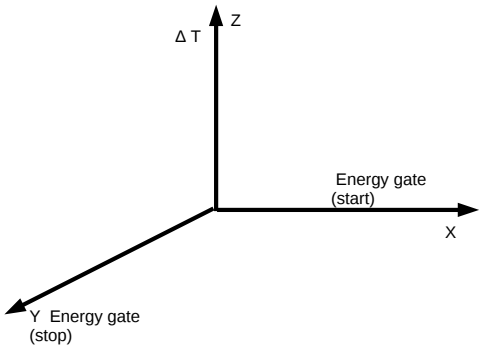

Figure 3.25: A representation of the three dimensional cube showing the energy gates on the x and y axis and the time difference on the z axis.

we consider ^{67}Ga source produced at iThemba LABS, it has a half-life of 3.26 days and initial activity of 3896.1 kBq, decays through 100% electron capture to ^{67}Zn. The spectrum showing the decay transitions, including the 184 keV and 209 keV transitions of ^{67}Ga is shown in Fig.3.26 (insert: The partial decay scheme of ^{67}Ga, here the 209 keV level is seen populating the 184 keV level).

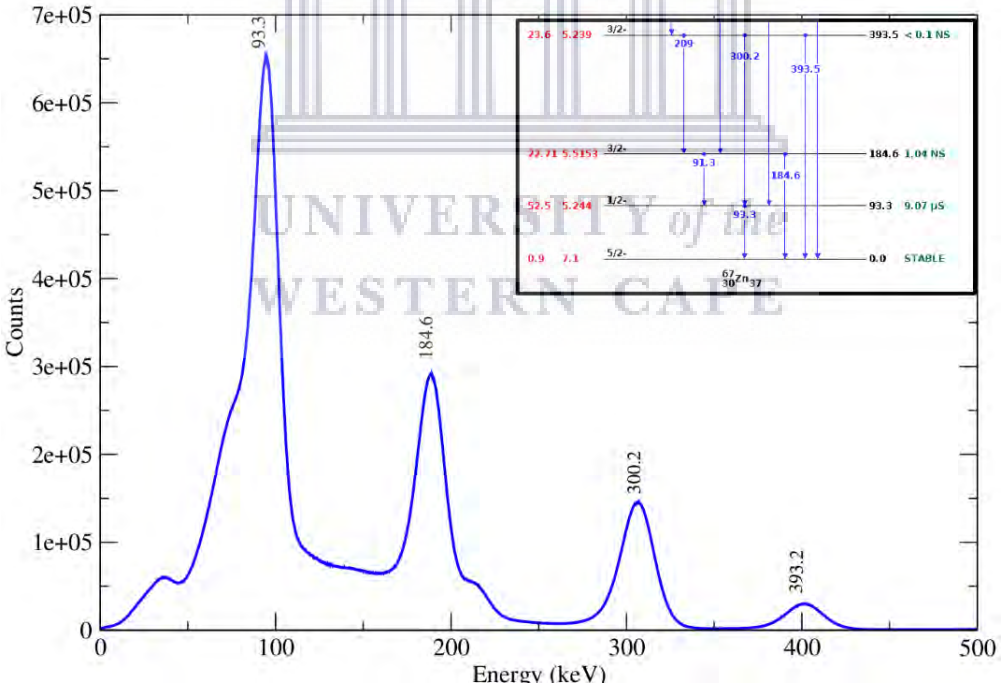

Figure 3.26: The spectrum of ^{67}Ga obtained from a $LaBr_3$:Ce detector. Insert: A level scheme showing the 209 keV transition populating the 184.6 keV level [119] [38].

In this decay process, the 184 keV level decays to the ground state via the $(3/2^-) \rightarrow (5/2^-)$

transition. In this work the lifetime of the $(3/2^-) \rightarrow (5/2^-)$ transition was measured. This was directly obtained by measuring the time between two signals of the $LaBr_3$:Ce detectors. The first signal which defines the start, is given by the 209 keV γ- ray populating the level and the second signal, which is the stop, by the 184 keV γ-ray depopulating it.

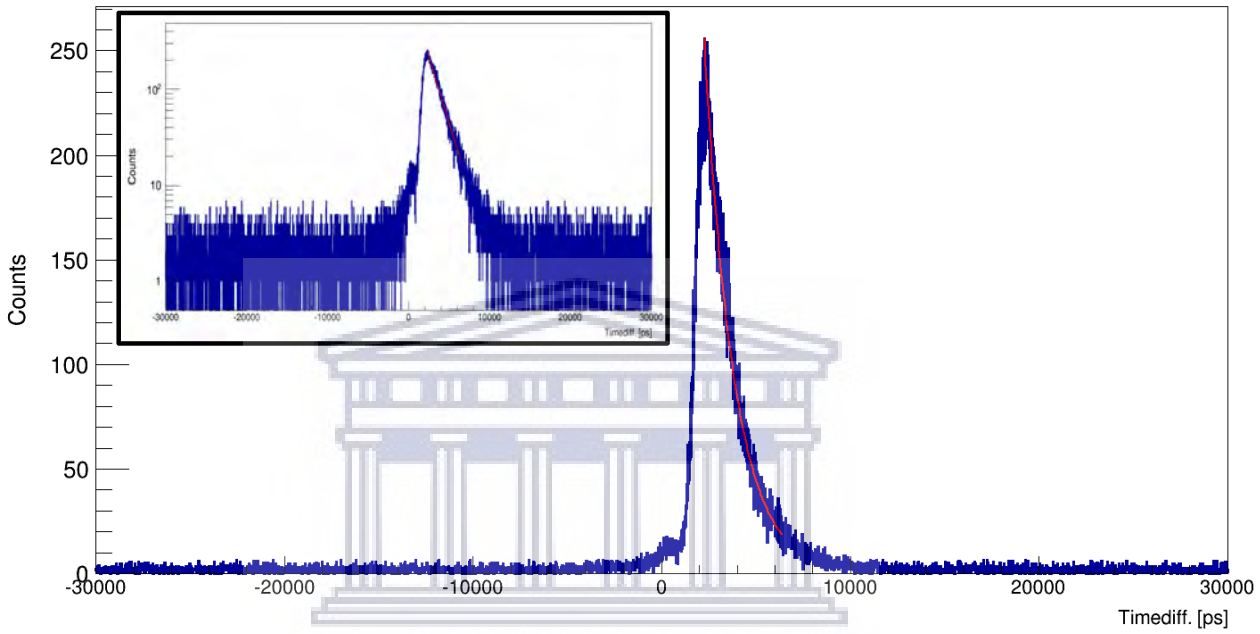

Figure 3.27: The time difference spectrum between two detectors fitted with exponential fit to determine the half life of the 184.6 keV level of the ^{67}Ga radioactive source. INSERT: The time spectrum on log scale.

The time spectrum obtained is shown in Fig.3.27 through which we were able to calculate the lifetime of the $(3/2^-) \rightarrow (5/2^-)$ transition. The lifetime of this transition was calculated to be $T_{1/2} = 1.090(7)ns$. The uncertainty was obtained through error propagation. Lieder *at al* [128] states this half life to be $T_{1/2} = 1.01(5)ns$. While Engel *at al* [129] asserts it to be $T_{1/2} = 1.026(14)ns$.

3.6.2 The convolution method

This method is employed for lifetimes that are comparable to the detector resolution but not much shorter. Assuming no background contribution, the experimentally obtained delayed time

distribution $D(t)$ is a convolution of the normalized Prompt Response Function (PRF) of the set-up, named $P(t)$, with an exponential decay as:

$$D(t) = n\lambda \int_{\infty}^{t} P(t^{'} - t_0) e^{\lambda t - t^{'}} dt^{'} \quad \text{with} \quad \lambda = \frac{1}{\tau} \tag{3.9}$$

where n is the total number of detected $\gamma - \gamma$ events in the time difference spectrum, or the normalization factor, λ is the transition (decay) probability, τ is the mean lifetime of the nuclear excited state interconnected by the $\gamma - \gamma$ cascade and t_0 is the centroid (center of gravity)of PRF $P(t)$.

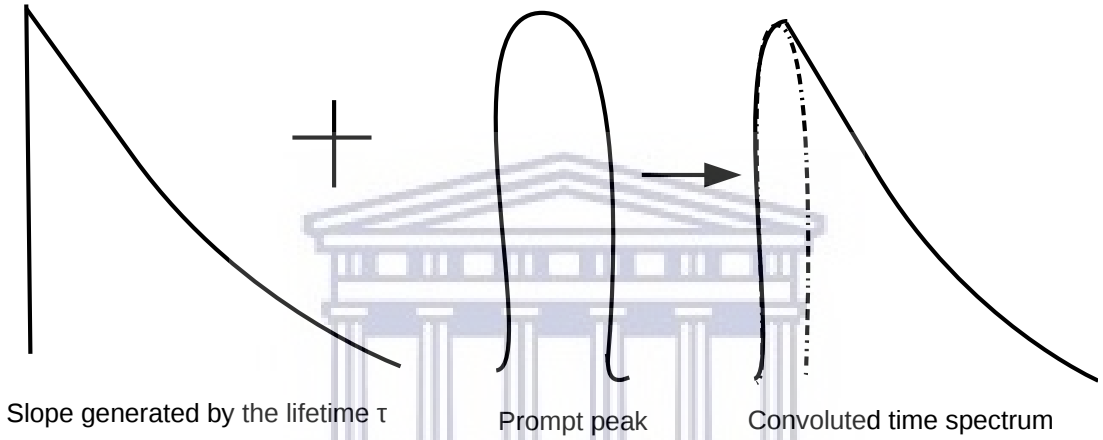

Figure 3.28: The delayed time distribution (slope generated by tau) obtained when the lifetime is longer than the time resolution and the prompt peak obtained from lifetimes that are much shorter than the time resolution. When the lifetime is comparable to the detector resolution then the two curves are convoluted.

Because the time spectrum is a convolution of the prompt peak as well as the exponential decay, a fit to this time distribution should be inclusive of both. The following equation describes the form of the fit obtained using a Gaussian function convoluted with an exponential decay [130]

$$C(t) = \frac{I}{2\tau} exp\left(\frac{\sigma^2}{2\tau^2} - \frac{t-\mu}{\sigma}\right) erfc\left(\frac{1}{\sqrt{2}}\left(\frac{\sigma}{\tau} - \frac{t-\mu}{\sigma}\right)\right) + C \tag{3.10}$$

where erfc is the complementary error function, σ and μ are the standard deviation and the centroid of the Gaussian component of the distribution respectively. The integral of the function is I, whereas τ gives the decay time of the exponential component of the distribution, which is the lifetime of the level of interest. The constant C shifts the function up or down, in order to include any contribution from residual background.

3.6.3 The Generalized Centroid Shift Method

To obtain lifetimes that are much faster than the detector resolution, in this work, the Generalized Centroid Shift (GCS) method [131], [132] was employed. Since the in-beam experimental set-up of this analysis consisted of six 2" by 2" $LaBr_3$:Ce detectors,
$N(N-1)/2$ detector-detector combinations are possible, with N being the number of detectors. The Generalized Centroid Shift Method takes advantage of a system with more than two $LaBr_3$:Ce detectors involving a γ-γ cascade. In this method, the centroid difference is given by the time shift between the centroids of the delayed and anti-delayed time spectra. This centroid difference, assuming no background contributions, corresponds to:

$$\Delta C_{FEP} = C_{delayed} - C_{antidelayed} = PRD + 2\tau \tag{3.11}$$

For unique detector-detector combinations ij, the centroid differences ΔC_{ij} can be measured to provide the mean value as [132]

$$\overline{\Delta C} = \frac{2\sum_{i=j}^{N=1}\sum_{j=i+1}^{N}\Delta C_{ij}}{N(N-1)} = \overline{PRD} + 2\tau \tag{3.12}$$

The mean value, $\overline{\Delta C}$, corresponds to the time shift between two fast-timing array time spectra generated by superposition of the start or stop unique detector-detector combinations.
To extract sub-nanosecond lifetimes, it is important to calibrate the zero-time response of the fast timing set-up. This involves a detailed and thorough process of determining the energy dependent centroid position of simultaneously occurring events (prompt events) of the prompt response function. Through this process, the timing characteristics describing the set-up is possible, which known as the "prompt response difference" (PRD) curve. The centroid shift method uses the PRD curve to determine lifetimes in the sub-nanosecond range.

3.6.4 The Prompt Response Difference curve

The PRD curve was determined using the ^{152}Eu radioactive source which decays to ^{152}Gd through β^- decay mode. It is worth noting that the ^{152}Eu radioactive source allows for precise PRD calibration in the range of 240 keV $<E_\gamma<$ 1300 keV, which is a suitable range for the lifetimes studied in this work. The nucleus ^{152}Gd emits several γ-ray transitions that are in coincidence with each other and have known picosecond lifetimes. This make it possible to select a reference

energy gate and keep it constant while varying other gates that are in coincidence with the chosen reference energy gate. In this work, the 344 keV state was chosen as reference energy gate since there are about seven γ-ray transitions that are in coincidence with it, see Fig.3.29. The γ-ray transitions populating this state are clearly shown in Fig.3.32a. For the PRD curve, one has to consider only full energy events and select a reference energy gate as either a start or stop detector.

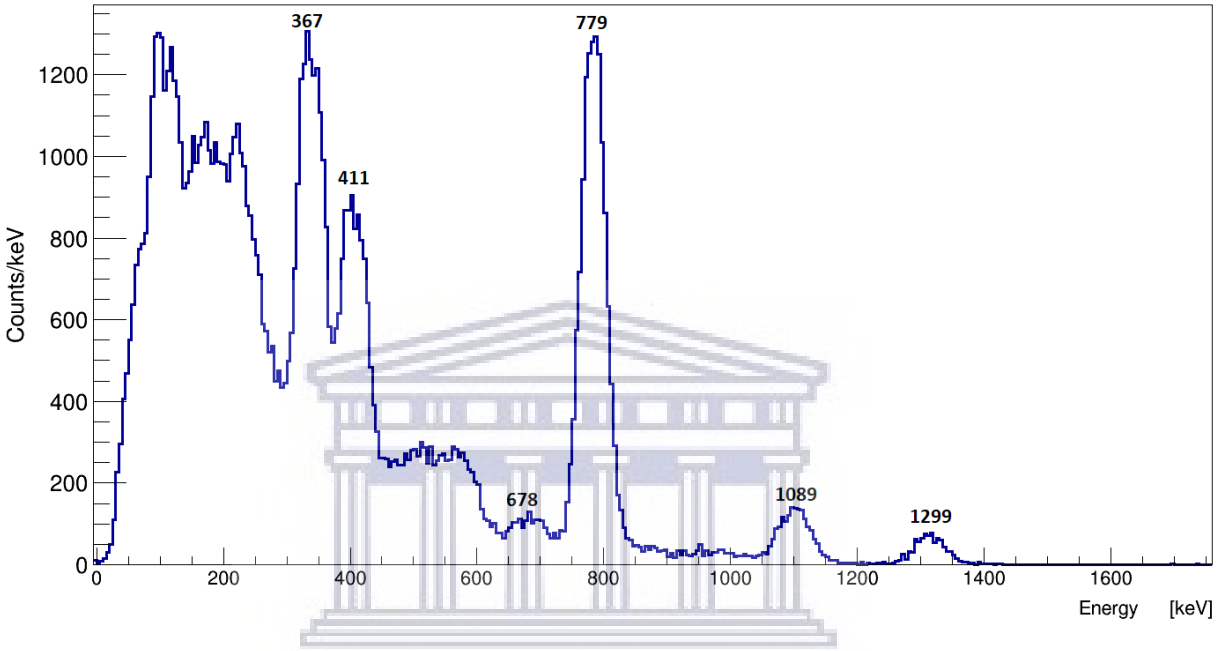

Figure 3.29: Coincidence spectrum gated on 344 keV with γ-rays obtained from the β^- decay of the ^{152}Eu radioactive source to ^{152}Gd.

The measured centroid difference between the energy chosen start and the energy chosen as a stop is given by:

$$\Delta C(E_\gamma)_{E_{ref}} = C(E_\gamma)_{stop} - C(E_\gamma)_{start} \tag{3.13}$$

where $C(E_\gamma)_{stop}$ is obtained by gating the reference transition on the stop detector and another detector gated on the start and vice-versa for $C(E_\gamma)_{start}$. A given excitation level consists of a transition that populates it, E_{feeder} and the one that depopulates it, E_{decay}. The transition corresponding to the E_{feeder} is set as the start detector and the transition corresponding to the E_{decay} is set as stop detector. The time distributions shown in Fig.3.30a exemplify how the measured centroid difference is obtained. The time distribution in blue is the anti-delayed that is obtained by gating E_{decay} as a start and gating on E_{feeder} as a stop. The situation is reversed when E_{decay} is gated as a stop and E_{feeder} is gated as a start, giving the delayed time distribution

which is the red time distribution.

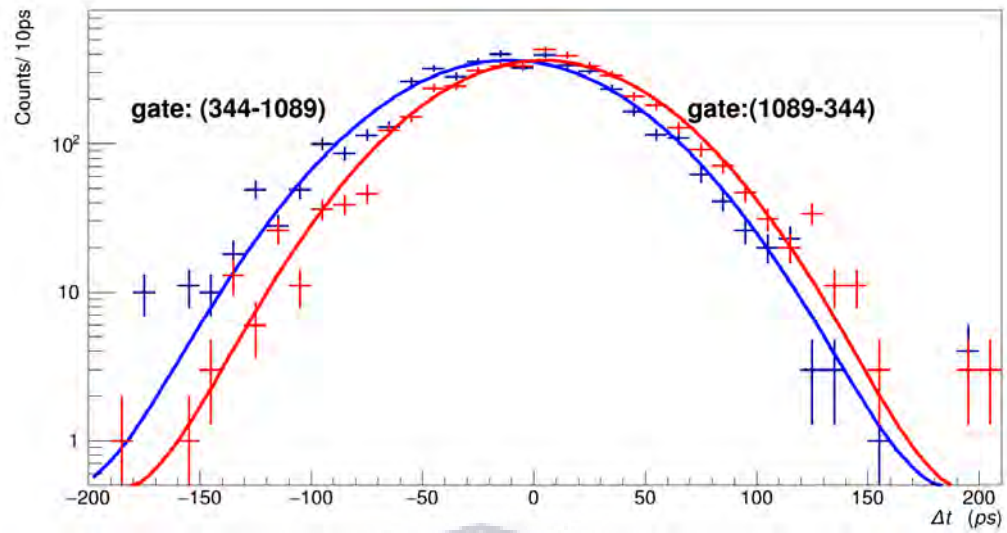

(a)

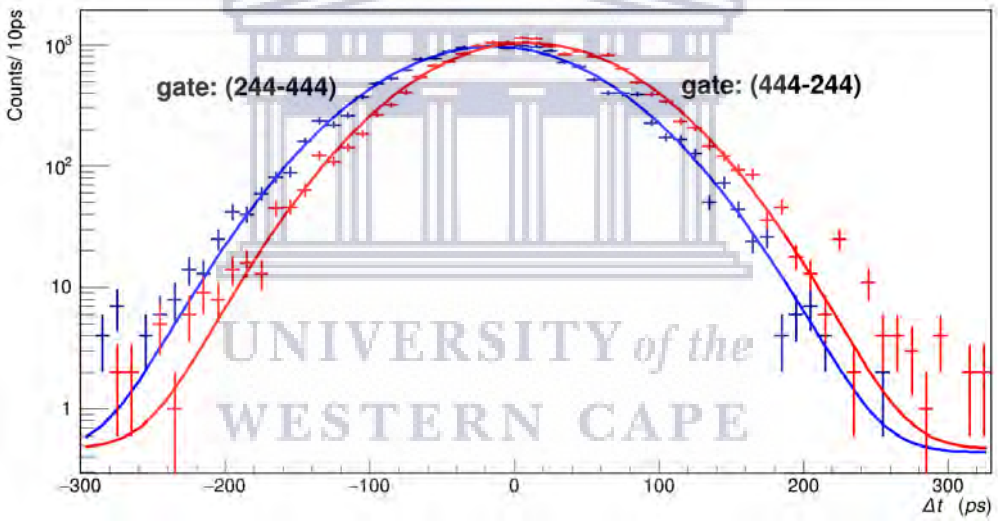

(b)

Figure 3.30: (a) Anti-delayed (blue) and delayed (red) time distributions for E_{decay} = 344 keV and E_{feeder} = 1089 keV.
(b) Anti-delayed (blue) and delayed (red) time distributions for E_{decay} = 244 keV and E_{feeder} = 444 keV. The centroid difference values is obtained from the difference of the centroids these time distributions

This measured centroid difference curve is then corrected by twice the known lifetime of the state, 2τ, to obtain each data point, which is then plotted as function of energy, yielding the PRD curve. The PRD curve obtained by gating on the 344 keV transition is shown in Fig.3.31. The data points of the PRD curve are then fitted using, [133]

$$PRD(E_\gamma) = \frac{a}{\sqrt{b + E_\gamma}} + cE_\gamma + d \tag{3.14}$$

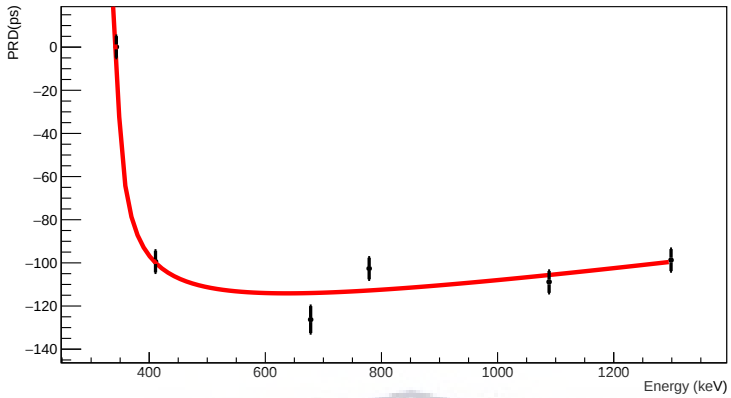

Figure 3.31: The PRD curve obtained by setting the reference energy gate at 344 keV, as a start, showing the energy dependency of $\gamma - \gamma$ fast-timing set-up.

The ^{152}Eu source also decays to ^{152}Sm through electron capture. The 244 keV transition of ^{152}Sm is populated by several transitions, see Fig.3.32b and therefore is useful as a reference energy. Following the similar procedure described previously, a PRD curve is obtained with energy reference at 244 keV, shown in Fig.3.33.

Differences between Fig. 3.31 and 3.33 are visible, with Fig. 3.31 exhibiting a deviation from the smooth monotonic behavour that is observed in figure 3.33. The points that are outside the PRD curve in Fig.3.31 may possibly be falsified by background contributions.

The two PRD curves, 3.31 and 3.33, can be shifted in parallel such that one overlaps onto another thus making a single PRD curve. This was done by changing the parameter d in equation 3.14 while keeping, a, b and c constant. This exercise is useful in adding more data points to the PRD curve. The new PRD, shown in Fig.3.34a is also fitted using equation 3.14, [133] to obtain new fit parameters :

fit 1: $a = 1572 \pm 382.2 \quad ps\sqrt{keV}$

b = -299.9 $\pm$ 11.83 $\quad keV$

c = 0.09113 $\pm$ 0.0188 $\quad ps/keV$

d = -268.2 $\pm$ 32.89 $\quad ps$

The fit residual of the fitted curve is shown in Fig.3.34b.

Deviations from the smooth monotonic curve are possibly induced by Compton events. In fact,

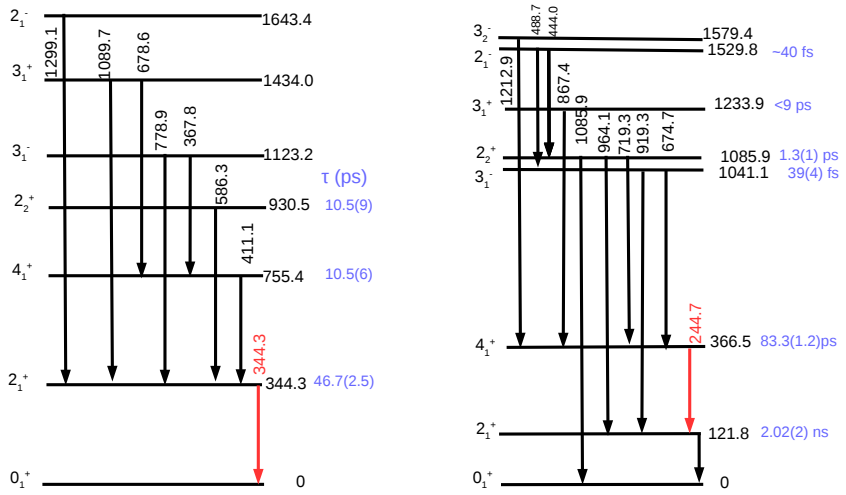

(a) (b)

Figure 3.32: (a) Partial level scheme of ^{152}Gd from the β^- decay of the ^{152}Eu radioactive source. (b) The partial level scheme of ^{152}Sm obtained after the electron capture ^{152}Eu radioactive source. There are several transitions that populate both the 344 keV and 244 keV state making them ideal candidates for reference gates. The half-lives of the excited states are highlighted in blue. The partial level schemes are deduced from information obtained from [119].

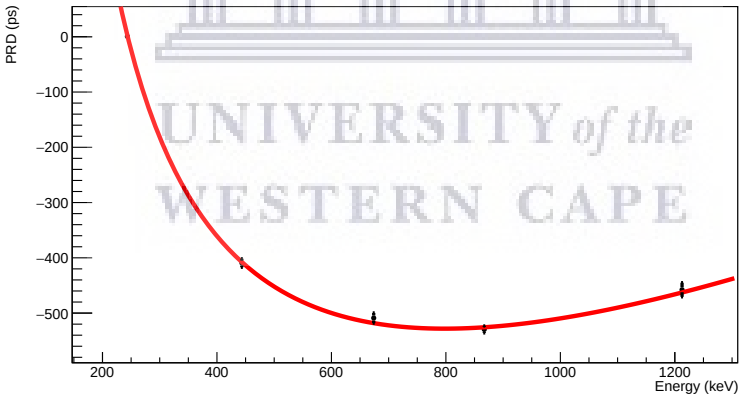

Figure 3.33: The PRD curve obtained by setting the reference energy gate at 244 keV plotted as a function of energy. Since ^{152}Eu source also decays to ^{152}Sm, it makes it possible to use 244 keV as an additional energy reference energy.

Mach *et al*, [134] also observed the shift of Compton events relative to the full energy events. Though both gates were set on full energy events to obtain the PRD curve, exposure to Compton events do contaminate the timing information of a $\gamma - \gamma$ fast-timing set-up, this is elaborated in section 4.1.1. Compton events may result in an artificial delay in the timing information. The

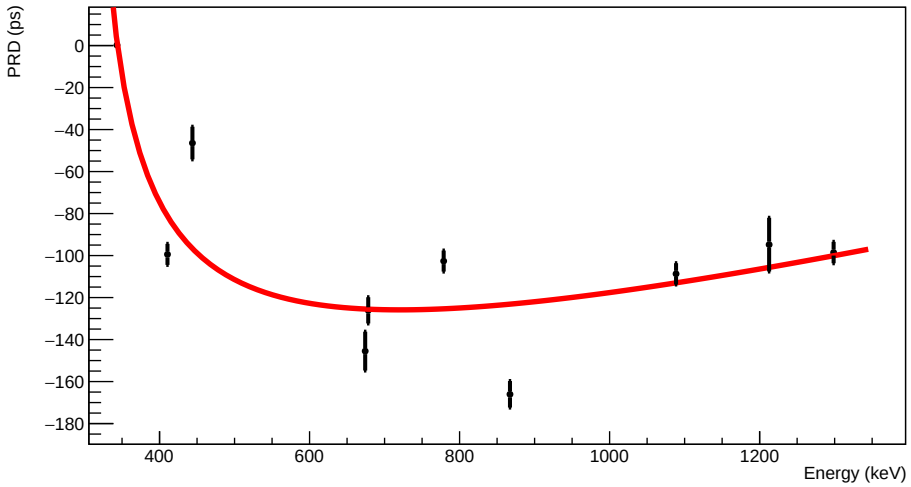

(a)

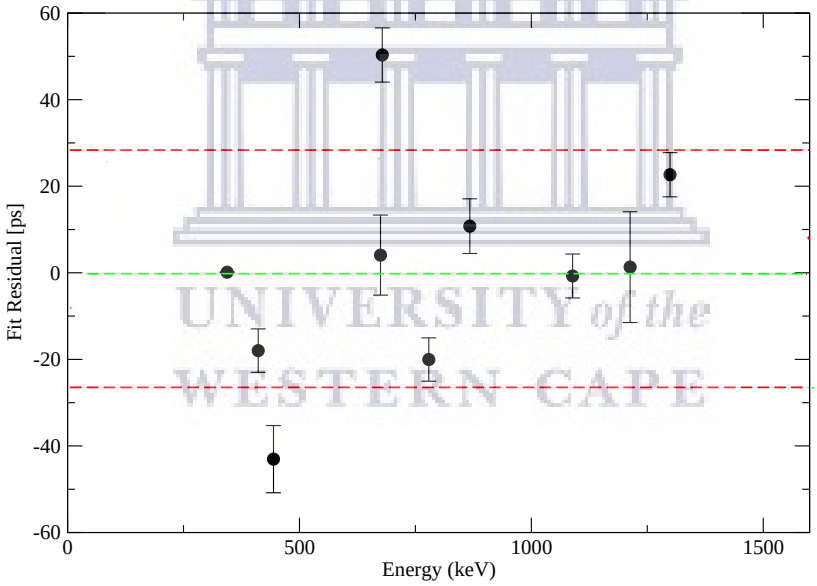

(b)

Figure 3.34: (a) The PRD curve obtained after the overlapping of the two curves obtained with reference energies 344 keV and 244 keV is done.
(b) The fit residual showing the data point deviation to the fit. The red dashed lines correspond to 26 ps, which is equivalent to 1σ . The error bars of each PRD point are obtained from the quadratic sum between: the uncertainty on the centroid values given by the fit, the errors on the literature value for the lifetime, and the residual given by the PRD curve before shifting the point and performing a second fit.

presence of an artificial delay in the time distributions is related to the time-of-flight of the scattered γ-ray, [134].

3.6.5 Background correction

The conventional way to minimize or reduce background in $\gamma - \gamma$ fast-timing set-up would be to do a background subtraction to approximate the pure full energy peak vs full energy peak. Several challenges exists with this conventional approach and include [135]:
It ignores the fact the centroid, the FWHM and slope of the background time distribution are dependent on the energy with a non-linear difference to the timing characteristics of the full energy events.
It does not consider the dependency of the FWHM of the time distribution on the energy gate width, which if overestimated the subtraction may result in a cut of the first part of the time distribution, thereby falsifying the result.

These are among the factors that make the background subtraction very complicated and have possible large systematic errors thus is not recommended for fast-timing. The following two methods were used in this current work are analytical background time-correction procedures that take advantage of the possibility to precisely determine the centroid of the background time distributions. The fundamental principle of both approaches is given by Bateman equations [136, 137].

The three volumes shifted background

Crucial to obtaining lifetimes that are accurate, is the ability to reduce background as much as possible. In this work, one of the methods employed is the three-shifted-volumes method [138]. In this method, one has to carefully select the background regions around full-energy peak events (FEPE). Here one needs to consider and select regions around the delayed and anti-delayed time distributions with each region having four absolute values. No physical subtraction is done but rather a correction is done to the measured ΔC value according to the centroid position of the background components. As an example, the FEPE and their background regions are shown Fig.3.35. The gates on the FEPE are marked in yellow whereas the background regions are marked in black. It is important that when choosing the background region, the gate should not be on the a full-energy peak. This can be ensured by observing the spectrum obtained from the HPGe clover detector. The FEPE gates set on the 350 keV and 772 keV may be labelled as the $p \mid p$ and the measured centroid as $C^m_{p|p}$. The respective background regions may be labelled as $bg \mid bg$ with

measured centroid as $C^m_{bg|bg}$. Setting a gate on the FEPE and the background region the measured centroid is $C^m_{p|bg}$ and vice-versa the measured centroid is $C^m_{bg|p}$.

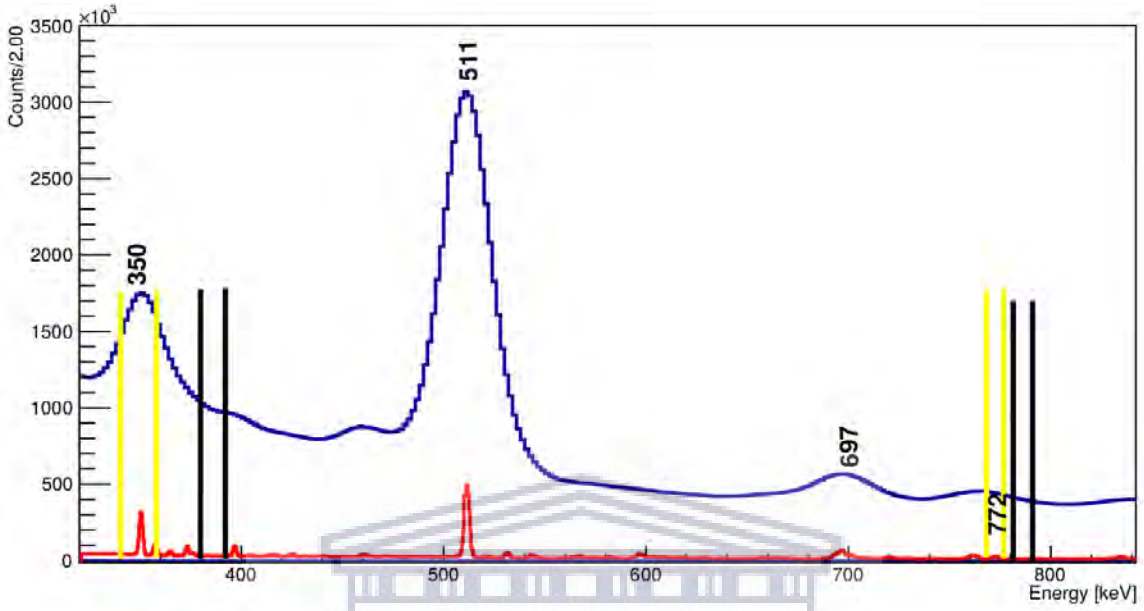

Figure 3.35: The $LaBr_3$:Ce spectrum (blue) and HPGe spectrum (red) showing the gates of FEPE events, shown by the yellow lines and the background gates shown by the black lines.

The position of the true centroid, $C^t_{p|p}$ can be obtained from the background correction procedure using the following relation:

$$C^t_{p|p} = \frac{n^m_{p|p}C^m_{p|p} - n^m_{p|bg}C^m_{p|bg} - n^m_{bg|p}C^m_{bg|p} + n^m_{bg|bg}C^m_{bg|bg}}{n^m_{p|p} - n^m_{p|bg} - -n^m_{bg|p} + n^m_{bg|bg}} \tag{3.15}$$

The Compton background correction

In any $\gamma - \gamma$ cascade, the two energy full energy peaks will most likely have background resulting from Compton contributions stemming from γ -rays from higher energies. The Compton background correction method [125] measures the centroid difference of two Compton time distributions obtained from the start and stop branch for a certain energy combination. Here, the full energy peak is used as a reference gate while the background energies around it are varied. The obtained centroid difference values are then fitted with a second order polynomial [139] and the Compton correction, ΔC_{bg}, is given by the value at a particular full energy peak. The analytical time-correction term is given by:

$$t_{cor} = \frac{\Delta C - \Delta C_{bg}}{P/B(E)} \tag{3.16}$$

Where *P/B(E)* is the relative peak-to-background ratio obtained from the energy gated coincidence spectrum and ΔC is the centroid difference obtained from the FEPE. The lifetime of an excited state is then calculated as follows:

$$\tau = \frac{\Delta C + t_{cor} - PRD}{2} \tag{3.17}$$

An extension to this method has been developed by [135]. Here the total correction time correction is obtained weighted average of two separately measured time correction terms related to the two experimental peak vs. background components of the $\gamma - \gamma$ cascade. The Compton background time correction term is now given by:

$$t_{cor}^{av} = \frac{P/B(E_f)t_{cor}E_i + P/B(E_i)t_{cor}E_f}{P/B(E_i) + P/B(E_f)} \tag{3.18}$$

Where E_i and E_f are the energies of the populating and depopulating transitions respectively in a $\gamma - \gamma$ cascade.

Chapter 4

Experimental results and discussion

4.1 Results

The present work explores how the techniques used in fast-timing yield results that are useful in investigating the properties of nuclear structure. This chapter presents the results obtained from this work and the methods employed to achieve these results. The test cases and the methods used to obtain the results are also discussed.

4.1.1 Compton scattering effects

In γ ray spectroscopy, particularly when studying γ-γ coincidences, Compton background is an inevitable phenomenon. It is therefore essential to comprehend Compton scattering and how it affects γ-γ time distributions. A single Compton interaction in the crystal followed by the escape of a scattered γ ray results in Compton background. In the low energy region, typically below 300 keV, scattered γ- rays can contaminate the γ ray spectrum giving rise to the back-scatter peak around 200 keV. For energies above 300 keV, the background underneath the full-energy peaks is mainly Compton scattered events.

Here the role of Compton scattering is explored in the in-beam set-up described in section 3 and out-of-beam source measurements, see section 3.5.6. The out-of-beam set-up is presented in Fig.3.18, it is apparent that there is no shielding present, either active or passive. The time distributions for the unique detector combinations are shown in Fig.4.1.

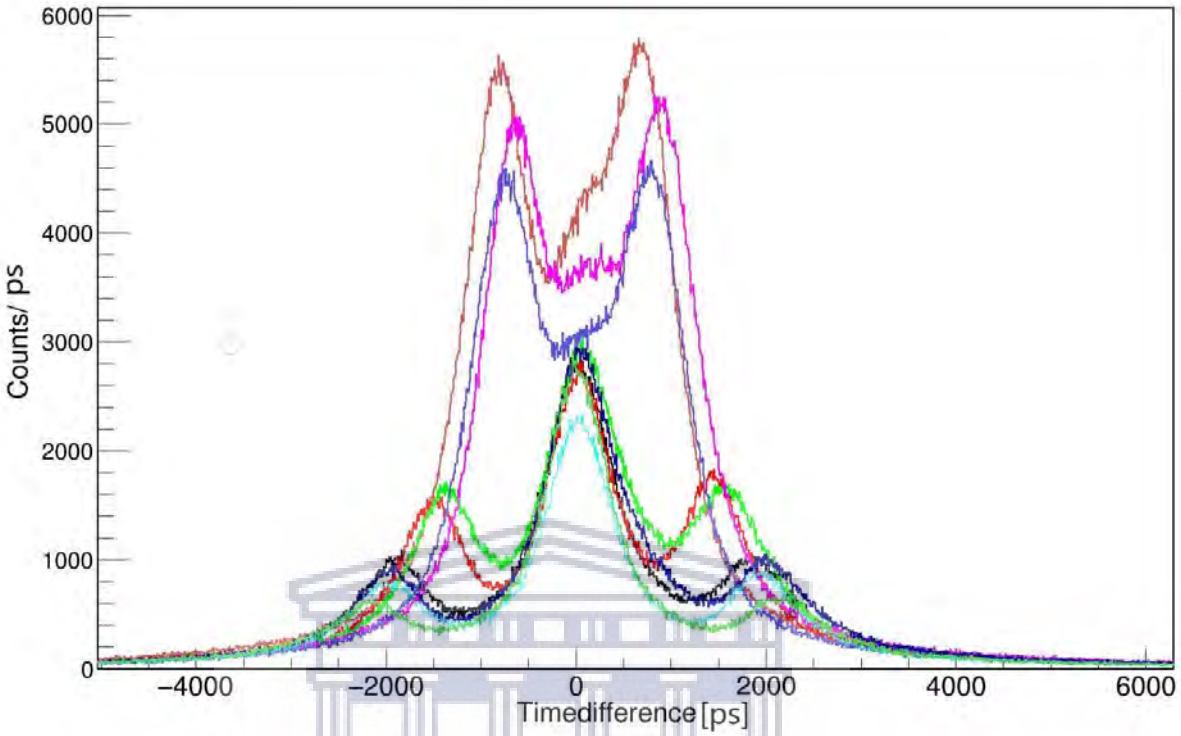

Figure 4.1: The time spectra for different combinations of the detectors used for source measurements. No visible shielding was present and the effect of the background resulting from either inter-detector Compton scattering or cross-talk can be observed.

The time spectra are obtained from the time difference of two detectors and their distributions are characteristic of how the detectors are arranged. The detector pairs that are arranged side by side or direct neighbouring pairs will experience inter-detector Compton scattering. When a γ ray strikes a detector and produces a Compton scattered event, the scattered γ ray will leave the detector and strike another detector and because the detectors arranged side-by-side are much closer to one another they are more likely to experience inter-detector Compton scattering. In this instance the time-of-flight of the time-difference distribution corresponds to the time-of-flight of the scattered γ ray between the two detectors [135]. The time distribution for the detectors that experience inter-detector Compton scattering by virtue of them being arranged side-by-side is illustrated in Fig.4.2a. When taking into account the detector pairs that are only facing each other, the time distribution obtained is illustrated in Fig.4.2b. Interestingly, three peaks are observed: the prompt peak at approximately 0 ps and two peaks at ∼-1600 ps and ∼1600 ps on either side, which is representative of the set-up geometry, which is represented by a source to detector distance of 240 mm.

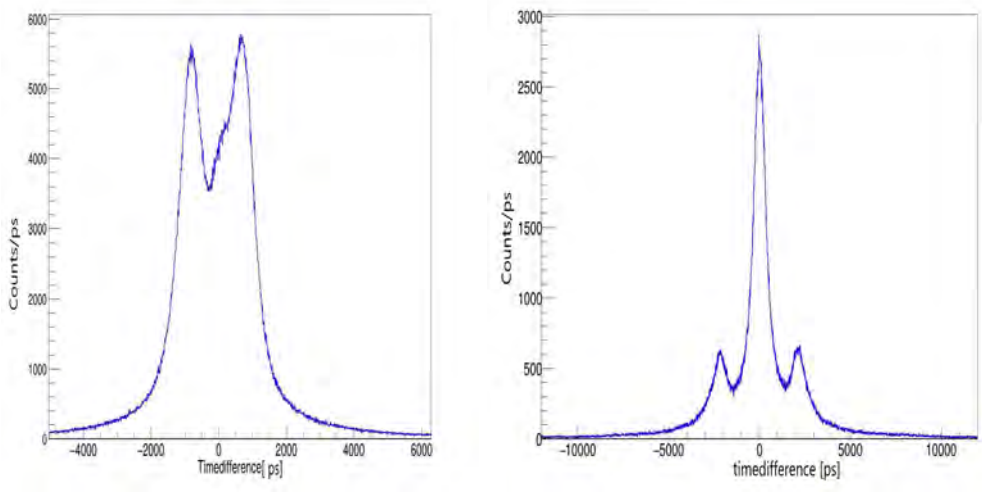

(a) (b)

Figure 4.2: (a) Time distribution for all the detector pairs that are arranged side by side so that they are direct neighbours.
(b) Time distributions of detector pairs that are facing each other. The prompt peak centred around $\Delta t = 0$ ps is where true γ-γ coincidences exists while the peaks at $\sim$ -1600 ps and $\sim$ 1600 ps is where false γ-γ coincidences are found.

The time-difference distribution is obtained from two detectors where one detector corresponds to a "start" and the other detector to a "stop". Events that are slower are recorded when the γ ray hits the "stop" detector, which evidently corresponds to the peak at $\sim$ 1600 ps. The events recorded when γ ray hits the "start" corresponds to the peak at $\sim$ -1600 ps. These events are a consequence of a γ ray depositing energy in one detector and a Compton-escaped γ ray detected in another. Consequently, this provides false γ-γ coincidence and thisobserved by setting a gate on either peak as illustrated in Fig.4.3. Commonly referred to as "cross-talk", these false γ-γ coincidences, carry false timing information related to the time of flight of the Compton-scattered γ ray [140]. The γ-γ matrix shown in Fig.4.3, exhibit diagonal streaks which are typically 180 Compton scattered events.

By setting a gate on the prompt peak, one observes that here there are true γ-γ coincidences as illustrated in Fig.4.4(a). Compton scattering is remarkably reduced in this instance as can be observed by the absence of diagonal streaks on the γ-γ matrix. Considering the in-beam set-up, between the $LaBr_3$:Ce detectors are the BGO shields that were connected to the HPGe clover detectors, see Fig.3.2. The BGO shields act as an effective passive shield, thisshown by the time-difference spectrum obtained from this set-up , Fig.4.4(b). Here, no side peaks that are a result of cross-talk are visible. Figure 4.5 further illustrates the effect of the cross-talk due to Compton

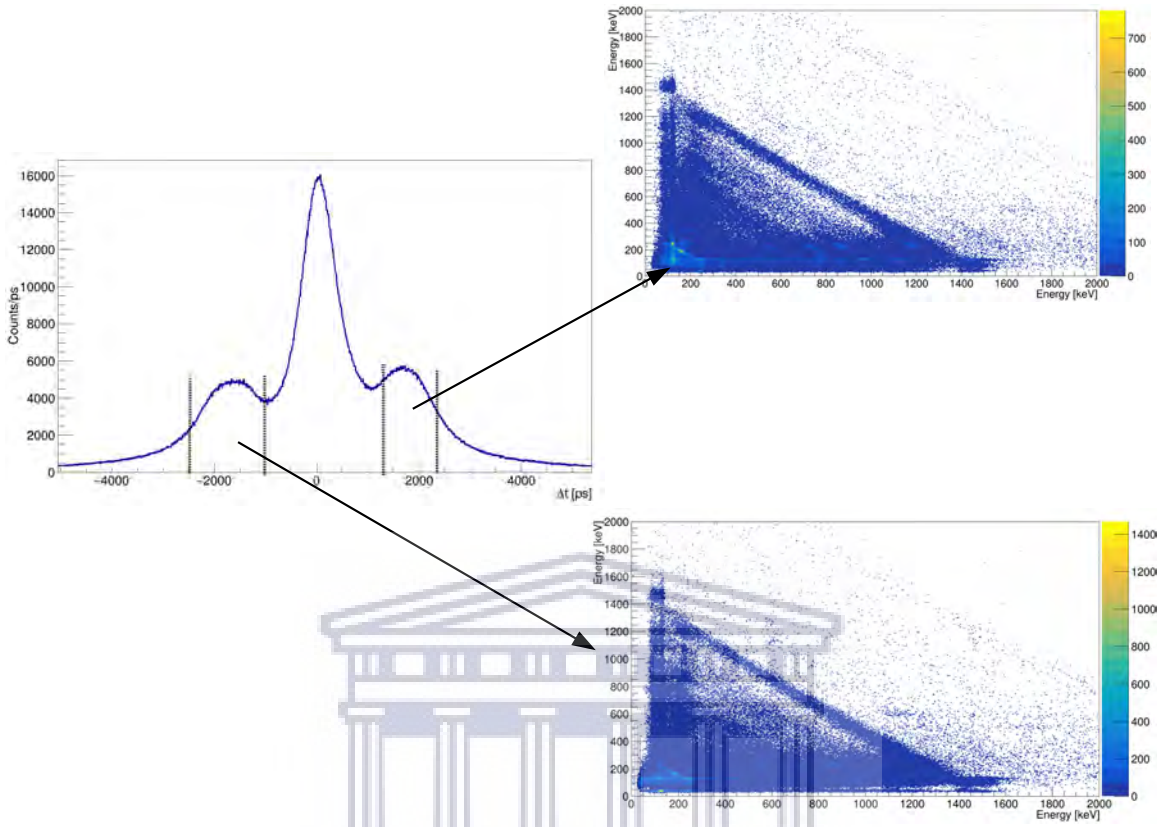

Figure 4.3: Setting a gate on the peak at ∼ -1600 ps and the one at ∼ 1600 ps, false γ-γ coincidences are obtained as can be seen from the γ-γ matrices obtained from each side peak.

scattering, with "ghost peak" overlapping the transitions of interest. Gating on the 245 keV, one would not expect the 1163 keV peak that is between the 1112 keV and 1213 keV, however, due to cross talk it exists in the out of beam set-up, see Fig.4.5a. While the in-beam set up, Fig.4.5b, the 1163 keV peak, this proves how the passive shielding of the BGO shields is effective in reducing cross-talk events.

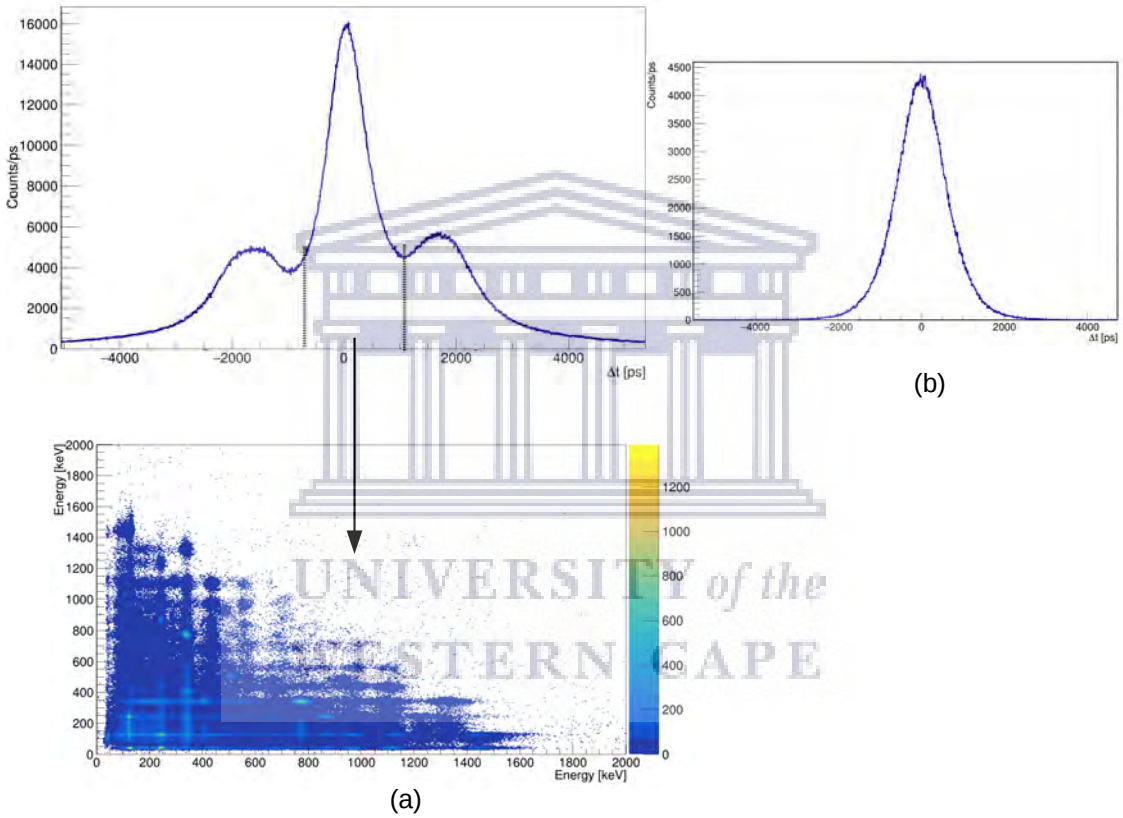

Figure 4.4: (a) Setting a gate on the prompt peak centred at Δt = 0 ps, the true γ-γ coincidences are obtained. (b) The prompt peak centred at Δt = 0 ps.

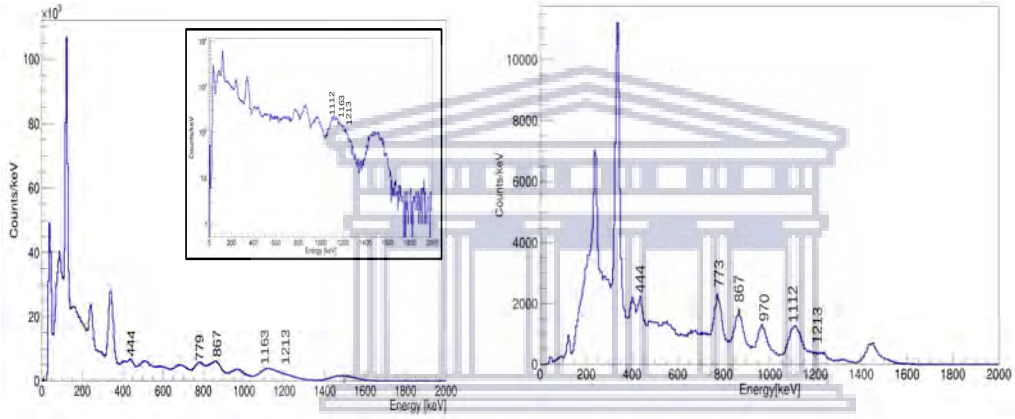

(a) (b)

Figure 4.5: (a) The gated ^{152}Eu spectrum with a gate set on 245 keV obtained from the out of beam set-up (see text). A "ghost peak", at 1163 keV is clearly visible between 1100 keV and 1200 keV . INSERT: The gated ^{152}Eu spectrum on log scale.
(b) Gate ^{152}Eu spectrum with a gate set on 245 keV obtained from the in-beam set up. No "ghost peak" is visible between 1100 keV and 1200 keV.

4.2 Nuclei in the $A > 40$ and $A \leq 45$ mass region

Studying nuclei with the doubly magic ^{40}Ca inert core is crucial in nuclear spectroscopy. In this work, the results of the lifetimes measured, which are crucial observables, for these nuclei are presented in this chapter.

4.2.1 The ^{44}Sc nucleus

The ^{44}Sc nucleus is an odd-odd nucleus with one valence proton and three valence neutrons outside the doubly magic ^{40}Ca nucleus. The nucleus ^{44}Sc was populated through the ^{45}Sc(p,d)^{44}Sc direct reaction at 27 MeV.

The 2^- state

The excited 2^- state, at 234.7 keV level has a known half-life reported by the ENDSF evaluated data sheet as $T_{1/2} = 6.12(23)$ ns [119]. In order to measure the half-life of this state, we set a gate on the feeding 396 keV gamma ray, which is the $4^- \rightarrow 2^-$ transition and a stop gate set on the $2^- \rightarrow 0^-$ transition. As an alternative, a reference timing signal was synchronized with the radio-frequency (RF) of the pulsed beam to form a start signal and the stop was given by one of the 2" by 2" $LaBr_3$:Ce detectors. Using the RF as a reference signal has an added advantage of yielding more statics and better results. In this work, we used the RF as a reference signal and also a $LaBr_3$:Ce detector as a reference signal allowing us to compare the results between RF-$LaBr_3$ and $LaBr_3$-$LaBr_3$ measurements. When the RF was used as a reference signal the lifetime obtained for the excited 2^- state, at 234.7 keV level is $T_{1/2} = 6.160(76) ns$. The time distribution spectrum from which this half-life was measured is shown in Fig.4.6a. The half-life for the same state when using $LaBr_3$-$LaBr_3$ measurements is $T_{1/2} = 5.93(41)$ ns, with the time distribution shown in Fig.4.6b. In both time spectra two components are visible; The large fast component is due to the Compton background and the slow component due to full energy peak detection. The slow component is fitted with an exponential fit in order to obtain the half-life using the slope method. Contributions from the large fast component may falsify lifetime measurements, however, these contributions may be avoided by fitting the slope outside the region of the Compton background. Since the background is distributed uniformly it may be determined and catered for prior the fit. The background contributions present in the time spectra, are partly due to background generated from coincident γ rays.

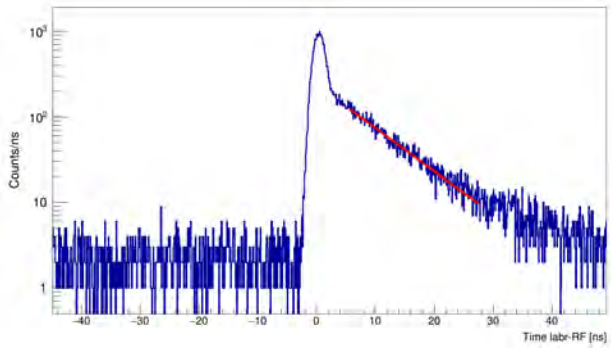

(a)

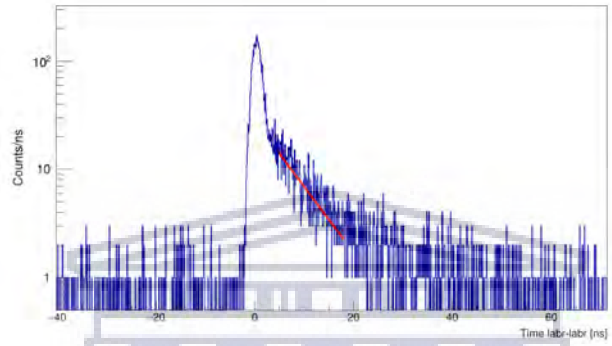

(b)

Figure 4.6: (a) Time spectrum obtained by the gating the radio-frequency and a $LaBr_3$:Ce detector used to measure the half-life the 234.7 keV level. The fitted region represents events of the full energy peak. (b) Time spectrum obtained when two $LaBr_3$:Ce detectors are used, for the 234.7 keV level, in which one is a start and the other is stop.

The 4^+ state

According to the ENDSF evaluated data sheet [119], the 4^+ state at 349.9 keV has a half-life of 3.12 (19)ns. To obtain the half-life of this state a gate was set on the $3^+ \rightarrow 4^+$ transition which feeds the 349.9 keV level. Using the slope method and from the RF-$LaBr_3$ measurement, we determined this half-life to be $T_{1/2} = 3.067(14)$ ns. Using the $LaBr_3$-$LaBr_3$ measurement, the half-life of this state was found to be $T_{1/2} = 2.499(15)$ ns.

The 3^- state

The 3^- state at 424.8 keV level has a reported half-life of 378 (42) ps [119]. The $\gamma - \gamma$ cascade used to measure the lifetime of this state is $5^- \rightarrow 3^-$ and $3^- \rightarrow 1^-$. The populating and depopulating γ energies are 772.5 keV and 356.92 keV respectively. The half-life of this state has been measured through the ^{28}Si(^{18}F, 2pnα) reaction [6] and through the ^{28}Si(^{18}O, pnα) reaction [141] using the Recoil Distance Method, see Table4.3.

The centroid difference value of ΔC = 721 (3) ps was obtained as shown in Fig.4.7 and the PRD correction factor for the combination 772.5 → 356.92 keV is given by PRD(772-356) = -99(26) ps. The lifetime is calculated to be equal to τ = 410(15) ps and the half-life is therefore 284 (10) ps.

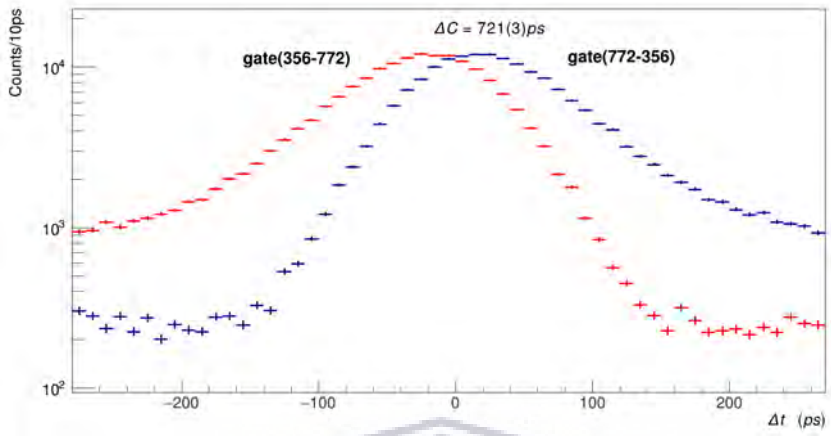

Figure 4.7: Time distribution spectra for the 772 → 356 $\gamma - \gamma$ cascade from which the ΔC value for the 429 keV level was obtained.

$$\tau = \frac{\Delta C(772-356) - \Delta PRD(772-356)}{2} = 410(15)\ ps \tag{4.1}$$

This value is rather low when compared the literature value and data obtained warrants the need to perform background correction. As as a start, both the three shifted volumes method, section 3.6.5 the Compton background correction, section 3.6.5, were applied.

The three shifted volumes method: When using the three shifted volumes method, the background regions were selected in regions where FEPE are not intermingled with the selected background gates. The FEPE are given by the energies 772.5 keV and 356.92 keV, each surrounded by the three background regions, peak-background ($p \mid b$), background-peak ($b \mid p$) and background-background ($bg \mid bg$) . In so doing, both the delayed and the anti-delayed regions are considered, whereby each will have a true centroid position $C^t_{p|p}$. The lifetime can then be calculated by considering the difference between the two values. Table 4.1 and 4.2 shows the values obtained for the centroid and number of counts, which were substituted into Eq.3.15.

The value true centroid position of the anti-delayed distribution is -501(46) ps while for the delayed distribution it is 358(2) ps. The centroid difference value ΔC_{cor} = 859 (46) ps. To obtain the lifetime of the 424.8 keV level, we simply substitute this value into the Eq.4.2, thus yielding a lifetime of τ = 479 (23) ps

Table 4.1: The measured centroid position as well the number of counts from which the true centroid position of the anti-delayed time distribution was obtained.

$C^m_{p\|p}$	$C^m_{p\|bg}$	$C^m_{bg\|p}$	$C^m_{bg\|bg}$
387 (2)	156 (2)	-253 (3)	155 (4)
$n^m_{p\|p}$	$n^m_{p\|bg}$	$n^m_{bg\|p}$	$n^m_{bg\|bg}$
188400	190900	259600	34260

Table 4.2: The measured centroid position as well the number of counts from which the true centroid position of the delayed time distribution was obtained.

$C^m_{p\|p}$	$C^m_{p\|bg}$	$C^m_{bg\|p}$	$C^m_{bg\|bg}$
334 (2)	-4.344 (3)	-17.9 (3)	-170.08 (4)
$n^m_{p\|p}$	$n^m_{p\|bg}$	$n^m_{bg\|p}$	$n^m_{bg\|bg}$
182500	30540	30320	34120

$$\tau = \frac{\Delta C_{cor}(772-356) - \Delta PRD(772-356)}{2} = 479(23)\ ps \tag{4.2}$$

The Compton background correction: In order to compute the energy-dependent centroid difference, ΔC_{bg}, gates were set around well defined background regions for both the FEPE in the $(772 \rightarrow 356)$ cascade. The reference energies are the FEPE whereas the background regions are varied. Figure 4.8 shows both background-timing analyses for the two experimental peak-background components fitted with a second order polynomial. The background gates were set at the same width. The $LaBr_3$:Ce and HPGe gated coincidence spectra are shown in Fig.4.9. The HPGe coincidence spectrum was used to select the background gate because of its excellent energy resolution.

The two time-correction terms for at each peak-background components were computed as follows:

$$t_{cor}(356) = \frac{721(3) + 340(2)}{8.4(2)} = 126(3)\ ps \tag{4.3}$$

and

$$t_{cor}(772) = \frac{721(3) + 125(2)}{3.1(2)} = 270(4)\ ps \tag{4.4}$$

The average, $t_{av} = 231(14)$, of the two time-correction is obtained by employing Eq.3.18. The lifetime of the 424.8 keV level, therefore is

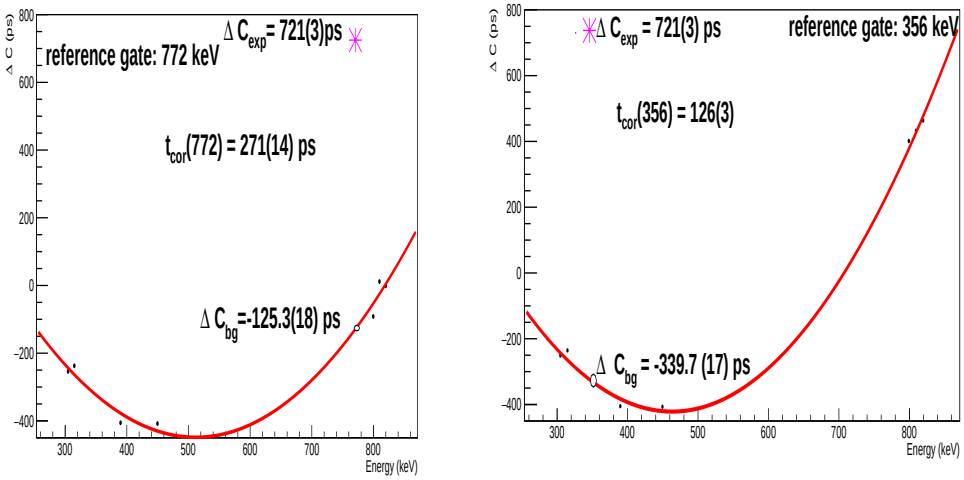

(a) (b)

Figure 4.8: (a) The centroid difference as a function of energy depicting background timing-analysis with the reference gate set at 772 keV with the background gates set around the regions of FEPE at 356 keV and 772 keV. The data points are fitted using a second order polynomial.
(b) The centroid difference as a function of energy depicting background timing-analysis with the reference gate set at 356 keV with the background gates set around the regions of FEPE at 356 keV and 772 keV. The data points are fitted using a second order polynomial.

$$\tau = \frac{721(3) + 231(14) + 100(26)}{2} = 526(15)\ ps \tag{4.5}$$

The 4^- state

With a known half-life of 404(30) ps [119] at 631 keV level, the faster 4^- state necessitates the need to utilize the Generalized Centroid Shift method. Previously this half-life has been measured through the ^{27}Al(^{19}F, pnα) reaction [5] and the ^{28}Si(^{18}O, pnα) reaction [141]. Both references used the Recoil Distance Method and their values are recorded in Table4.3.

The transitions used to measure the lifetime of the 631 keV level in this work are the $6^- \rightarrow 4^-$ transition and the $4^- \rightarrow 2^-$ transition. The corresponding γ rays energies are 1124.1 keV and 396.24 keV respectively which are the populating and depopulating transitions. Figure 4.10 shows the two time distributions from which the centroid difference value of ΔC = 454 (4) ps was obtained. The PRD correction factor for the combination 1124.1 $\rightarrow$ 396.24 keV is given by PRD(1124-396) = -39(26) ps: It follows from 3.13, the lifetime of the 631 keV level is then calculated as follows:

$$\tau = \frac{\Delta C(1124-396) - \Delta PRD(1124-396)}{2} = 246(14)\ ps \tag{4.6}$$

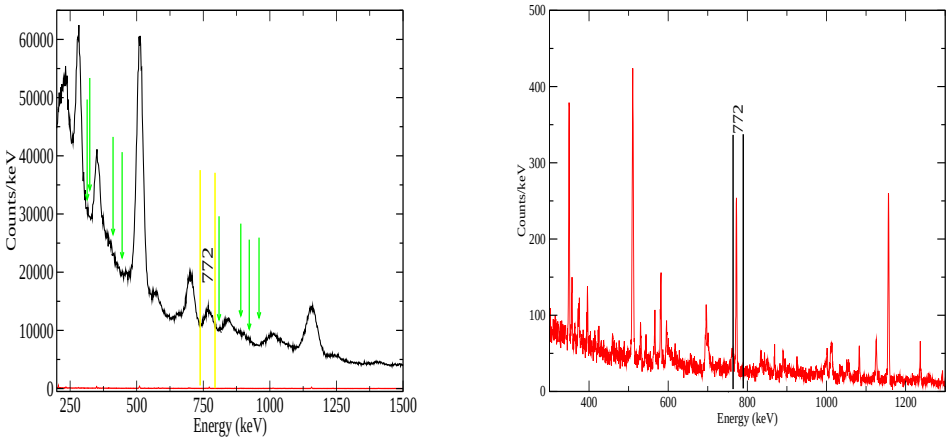

(a) (b)

Figure 4.9: (a) The γ-γ coincidence spectrum gated on the 356 keV. The full energy peak in coincidence with the 356 keV peak, used to obtain the lifetime, is the 772 keV energy. The arrows mark the the regions where the background gates around the full energy peaks were set. The black energy spectrum is the $LaBr_3$:Ce coincidence spectrum and the red energy spectrum is HPGe coincidence spectrum.
(b) The HPGe gated spectrum clearly showing the 772 keV γ ray energy that is in coincidence 356 keV γ ray energy.

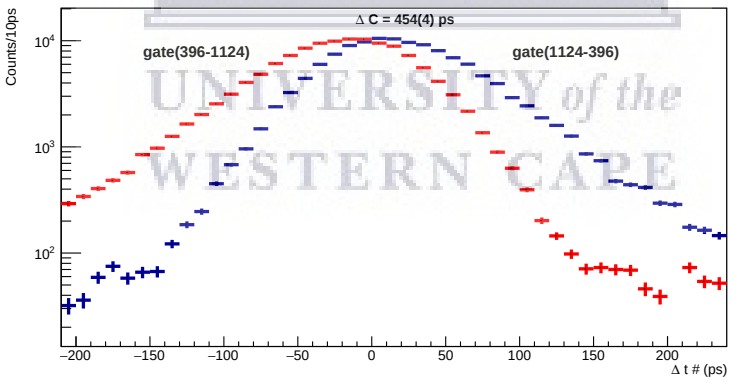

Figure 4.10: Time distribution spectra for the 1124 $\rightarrow$ 396 $\gamma - \gamma$ cascade from which the ΔC value for the 631 keV level was obtained.

A background correction is then performed using the Compton correction method. The background timing-analyses spectra used to correct for the background are shown in Fig.4.11. The lifetime of the 631 keV level is then calculated using the method as elaborated in 4.2.1.

$$\tau = \frac{454(4) + 476(34) + 39(26)}{2} = 484(21)\, ps \tag{4.7}$$

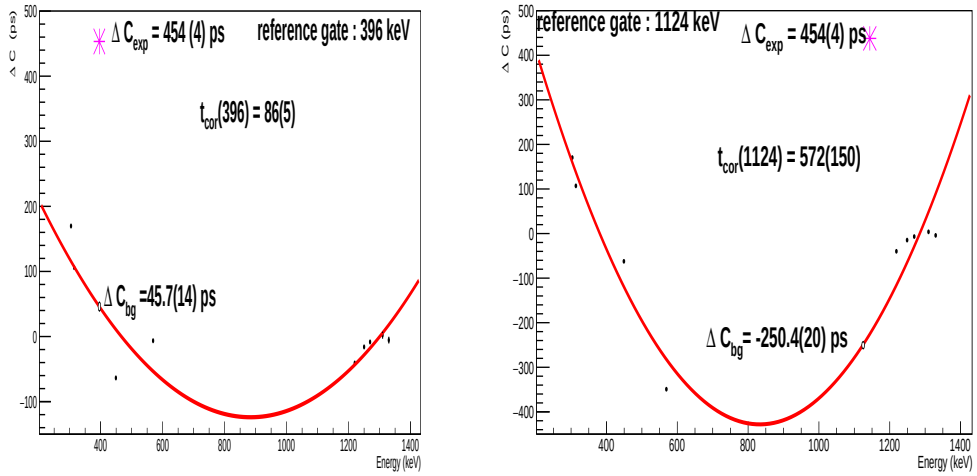

(a) (b)

Figure 4.11: (a) The centroid difference as a function of energy depicting background timing-analysis with the reference gate set at 396 keV with the background gates set around the regions of FEPE at 396 keV and 1124 keV. The data points are fitted using a second order polynomial. (b) The centroid difference as a function of energy depicting background timing-analysis with the reference gate set at 1124 keV with the background gates set around the regions of FEPE at 396 keV and 1124 keV. The data points are fitted using a second order polynomial.

The $LaBr_3$:Ce and HPGe gated coincidence spectra are shown in Fig.4.12. The HPGe coincidence spectrum was used to select the background gate because of its excellent energy resolution.

The 6^- state

The 6^- state at 2210.5 keV level has no known lifetime recorded in literature. In this work, the lifetime of the 6^- state at 2210.5 keV level was measured. The transition that populates this state is the $7^- \rightarrow 6^-$ and it is associated with 396.2 keV γ ray. The 2210.5 keV level is depopulated by the $6^- \rightarrow 5^-$ which is associated with the 1013 keV γ ray. The centroid difference ΔC = 316(2) ps, as illustrated by Fig. 4.13.

Background-timing analyses spectra from which Compton background correction was performed are shown in Fig.4.14. The PRD correction factor for the (396 $\rightarrow$ 1013) cascade is PRD(396-1013) = -45(26) ps. The lifetime of this state is measured as:

$$\tau = \frac{316(2) + 105(6) + 45(26)}{2} = 234(13)\ ps \tag{4.8}$$

The $LaBr_3$:Ce and HPGe gated coincidence spectra are shown in Fig.4.15. The HPGe coincidence spectrum was used to select the background gate because of its excellent energy resolution.

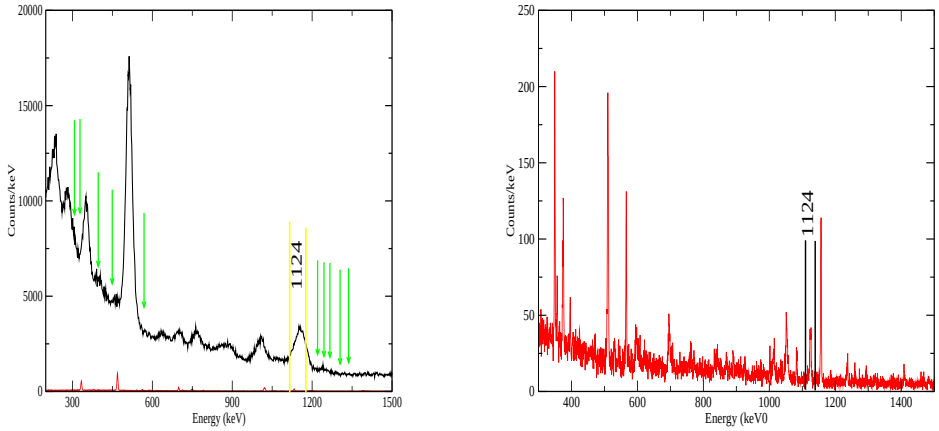

(a) (b)

Figure 4.12: (a) The γ-γ coincidence spectrum gated on the 396 keV. The full energy peak in coincidence with the 396 keV peak, used to obtain the lifetime, is the 1124 keV energy. The arrows mark the the regions where the background gates around the full energy peaks were set. The black energy spectrum is the $LaBr_3$:Ce coincidence spectrum and the red energy spectrum is HPGe coincidence spectrum.
(b) The HPGe gated spectrum clearly showing the 1124 keV γ ray energy that is in coincidence 396 keV γ ray energy.

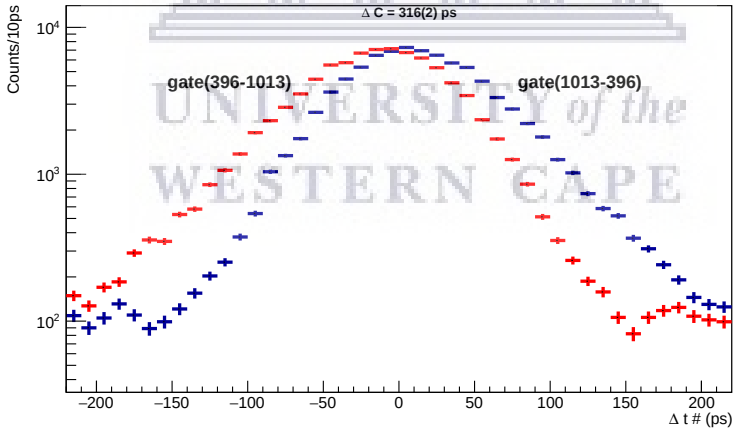

Figure 4.13: Time distribution spectra for the 396 $\rightarrow$ 1013 $\gamma - \gamma$ cascade from which the ΔC value for the 2210.5 keV level was obtained.

The 7^- state

The 7^- state at 2606.7 keV level has no known lifetime recorded in literature. This work reports the lifetime of this state. The 2606.7 keV is populated by the 382 keV γ ray level through the

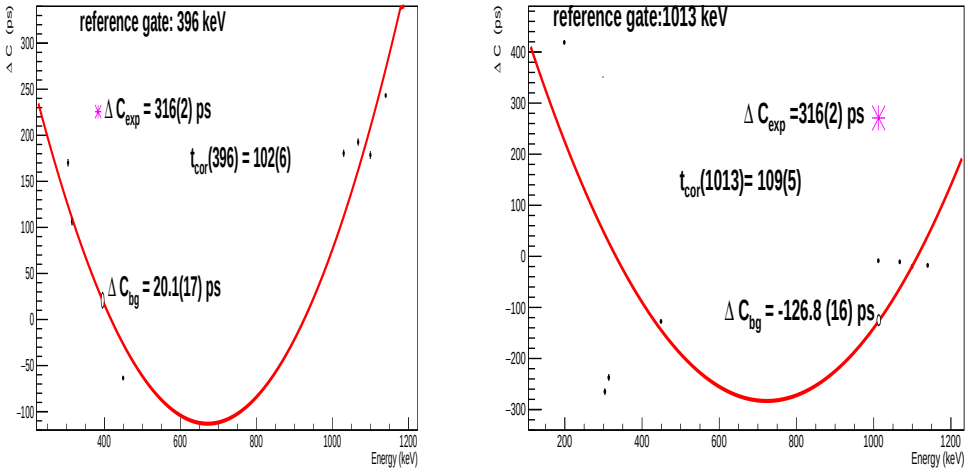

(a) (b)

Figure 4.14: (a) The centroid difference as a function of energy depicting background timing-analysis with the reference gate set at 396 keV with the background gates set around the regions of FEPE at 396 keV and 1013 keV. The data points are fitted using a second order polynomial. (b) The centroid difference as a function of energy depicting background timing-analysis with the reference gate set at 1013 keV with the background gates set around the regions of FEPE at 396 keV and 1013 keV. The data points are fitted using a second order polynomial.

$8^- \rightarrow 7^-$ transition. The depopulating γ ray is 1409 keV through the $7^- \rightarrow 5^-$ transition. The centroid difference is ΔC =344(5) ps, as illustrated by Fig. 4.16.

Correcting for the background using the Compton background correction method, the background-timing analyses spectra are shown in Fig.4.17. The PRD correction factor for the (382 $\rightarrow$ 1409) cascade is PRD(382-1409) = -33(26) ps. Therefore the lifetime of the 2606.7 keV was found to be:

$$\tau = \frac{344(5) + 143(14) + 33(26}{2} = 260(15)\ ps \tag{4.9}$$

The 8^- state

The lifetime of the 8^- state at 3364.1 keV level was measured in this work and it has no known literature value. The 465 keV γ ray populates this level and it is the $9^- \rightarrow 8^-$ transition. It is also depopulated by a $8^- \rightarrow 7^-$ transition associated with the 757 keV γ ray. The centroid difference is ΔC = 292(3) ps, as illustrated by Fig. 4.18.

Correcting for the background using the Compton background correction method, the background-timing analyses spectra are shown in Fig.4.19. The PRD correction factor for the (465 $\rightarrow$ 757) cascade is PRD(465-757) = -22(26) ps. Therefore the lifetime of the 3364.1 keV level was found

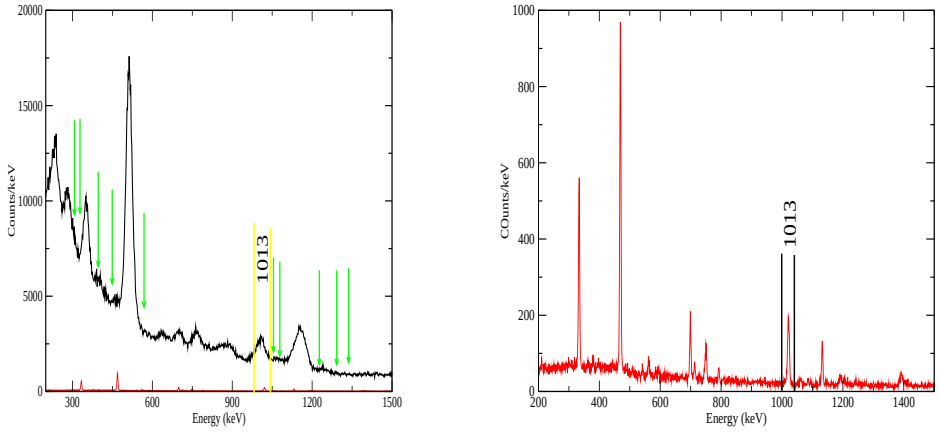

(a) (b)

Figure 4.15: (a) The γ-γ coincidence spectrum gated on the 396 keV. The full energy peak in coincidence with the 396 keV peak, used to obtain the lifetime, is the 1013 keV energy. The arrows mark the the regions where the background gates around the full energy peaks were set. The black energy spectrum is the $LaBr_3$:Ce coincidence spectrum and the red energy spectrum is HPGe coincidence spectrum.
(b) The HPGe gated spectrum clearly showing the 1013 keV γ ray energy that is in coincidence 396 keV γ ray energy.

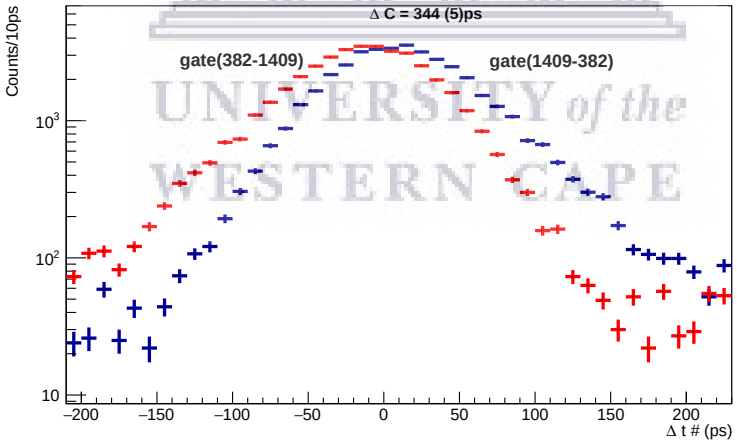

Figure 4.16: Time distribution spectra for the $382 \rightarrow 1409$ $\gamma - \gamma$ cascade from which the ΔC value for the 2606.7 keV level was obtained.

to be:

$$\tau = \frac{292(3) + 160(22) + 22(26)}{2} = 237(17)\, ps \tag{4.10}$$

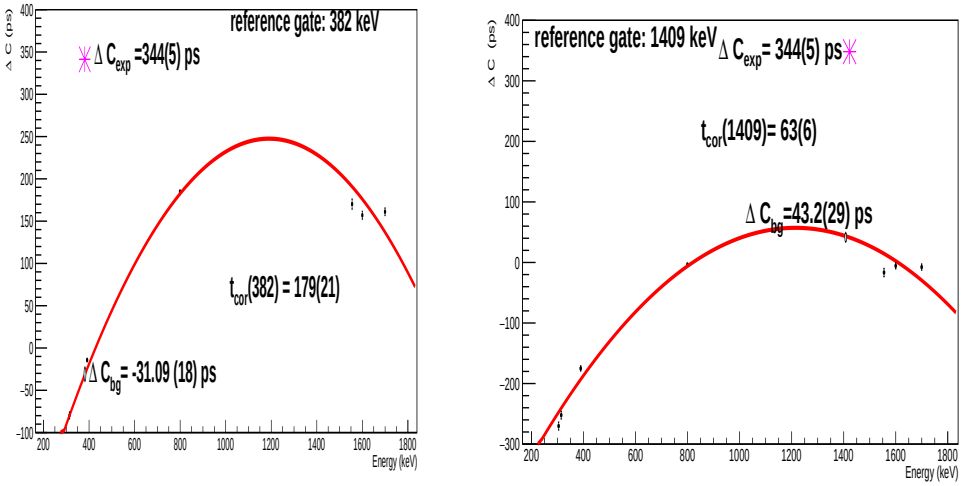

(a) (b)

Figure 4.17: (a) The centroid difference as a function of energy depicting background timing-analysis with the reference gate set at 382 keV with the background gates set around the regions of FEPE at 382 keV and 1409 keV. The data points are fitted using a second order polynomial. (b) The centroid difference as a function of energy depicting background timing-analysis with the reference gate set at 1409 keV with the background gates set around the regions of FEPE at 382 keV and 1409 keV. The data points are fitted using a second order polynomial.

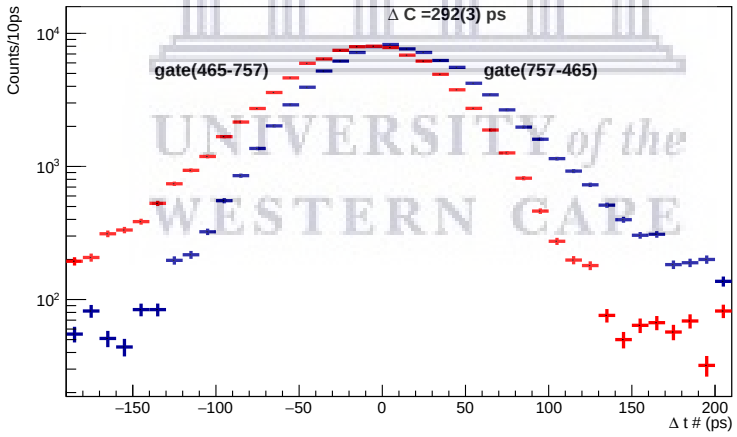

Figure 4.18: Time distribution spectra for the 465 → 757 $\gamma - \gamma$ cascade from which the ΔC value for the 3364.1 keV level was obtained.

Figure 4.20 compares the half-lives obtained in this work (blue) of the 2^- state at 234.7 keV level and 4^+ state at 349.9 keV level with the previously measured half-lives.

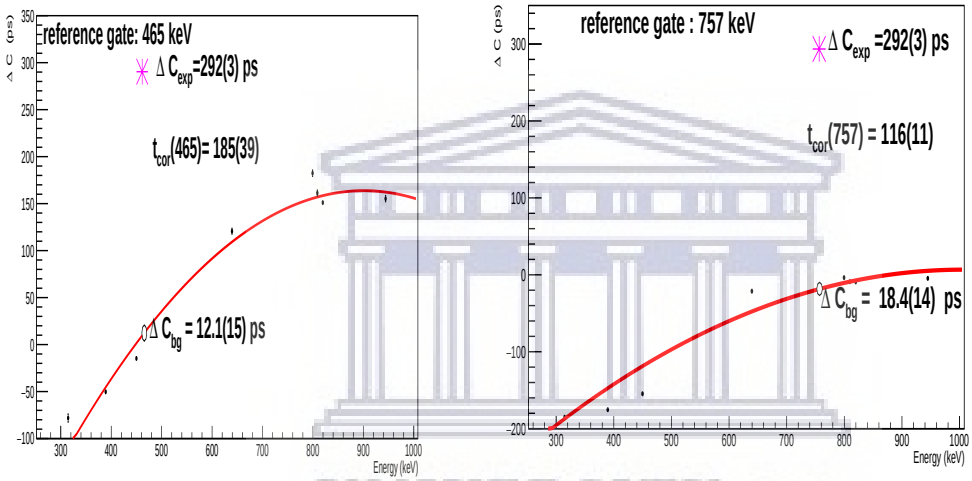

(a) (b)

Figure 4.19: (a) The centroid difference as a function of energy depicting background timing-analysis with the reference gate set at 465 keV with the background gates set around the regions of FEPE at 465 keV and 757 keV. The data points are fitted using a second order polynomial. (b) The centroid difference as a function of energy depicting background timing-analysis with the reference gate set at 757 keV with the background gates set around the regions of FEPE at 465 keV and 757 keV. The data points are fitted using a second order polynomial.

Table 4.3: Experimentally obtained half-lives that have been published for different states of ^{44}Sc. The values obtained in the current work are highlighted in blue. The sub-nanosecond lifetimes are background corrected, those that are corrected via the three volumes shifted method are indicated by the subscript (TSV) and those corrected via the Compton background correction are indicated by the subscript CB.

Energy level (keV)	J^π	Method	Reference	Half-life
234.7	2^-	Recoil Distance	[141]	12.7 (22)ns
234.7	2^-	Delayed coincidence	[142]	6.12 (23)ns
234.7	2^-	ENSDF Evaluation	Adopted ENSDF value [119]	6.12 (23)ns
234.7	2^-	Fast-Timing (RF-$LaBr_3$)	Present work	6.160 (76)ns
234.7	2^-	Fast-Timing ($LaBr_3$-$LaBr_3$)	Present work	5.93 (41)ns
Energy level (keV)	J^π	Method	Reference	Half-life
349.9	4^+	Recoil Distance	[141]	3.12 (28)ns
349.9	4^+	Recoil Distance	[6]	3.1 (3)ns
349.9	4^+	ENSDF Evaluation	Adopted ENSDF value [119]	3.12 (19)ns
349.9	4^+	Fast-Timing (RF-$LaBr_3$)	Present work	3.067 (14)ns
349.9	4^+	Fast-Timing ($LaBr_3$-$LaBr_3$)	Present work	2.499 (15)ns
Energy level (keV)	J^π	Method	Reference	Half-life
631	4^-	Recoil Distance	[5]	381 (55)ps
631	4^-	Recoil Distance	[141]	411 (30)ps
631	4^-	ENSDF Evaluation	Adopted ENSDF value [119]	404 (30)ps
631	4^-	Fast-Timing (GCD_{CB})	Present work	336 (15)ps
631	4^-	Fast-Timing (GCD_{TSV})	Present work	323 (12)ps
Energy level (keV)	J^π	Method	Reference	Half-life
428.8	3^-	Recoil Distance	[6]	380 (40)ps
428.8	3^-	Recoil Distance	[141]	378 (42)ps
428.8	3^-	ENSDF Evaluation	Adopted ENSDF value [119]	378 (42)ps
428.8	3^-	Fast-Timing (GCD_{CB})	Present work	364 (10)ps
Energy level (keV)	J^π	Method	Reference	Half-life
2210.5	6^-	Fast-Timing (GCD_{CB})	Present work	162 (9)ps
2606.7	7^-	Fast-Timing (GCD_{CB})	Present work	180 (10)ps
3364.1	8^-	Fast-Timing (GCD_{CB})	Present work	164 (12)ps

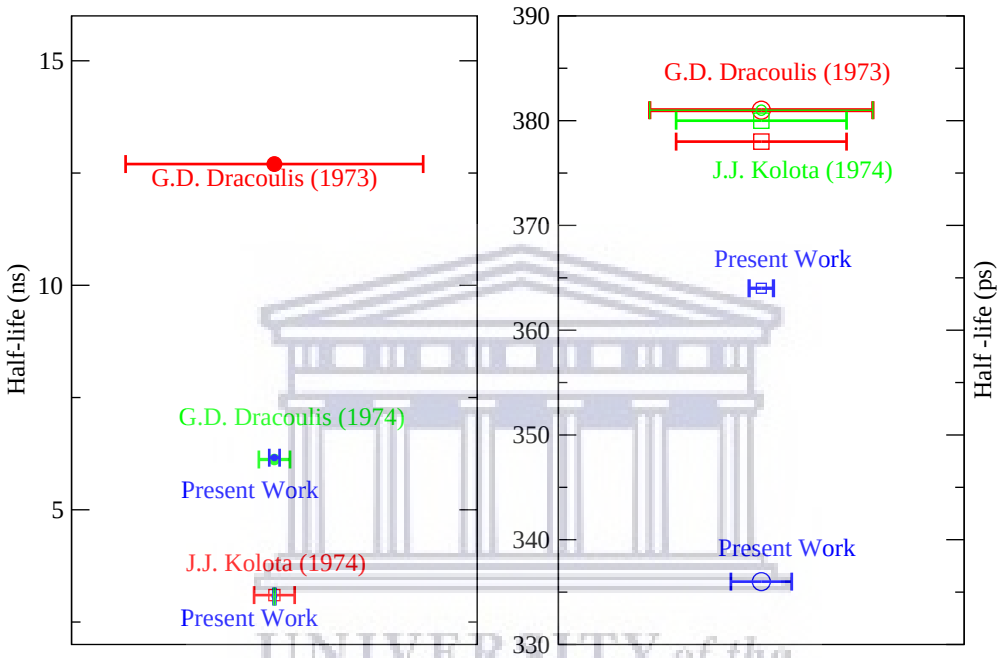

Figure 4.20: Left:The half-life of the 2^- state at 234.7 keV level obtained from the RF-$LaBr_3$ measurement, symbolized by solid circle, obtained in this work is compared to previously measured obtained literature values. The half-life of the 4^+ state at 349.9 keV level, symbolized by squares, obtained in this work is compared to previously measured obtained literature values. Methods employed in obtaining these half-lives is shown in Table4.3.
Right: The half-life of the 4^- state at 631 keV level, symbolized by the open circles, obtained in this work is compared to previously measured obtained literature values. The half-life of the 3^- state at 428.8 keV level, symbolized by the open squares, obtained in this work is compared to previously measured obtained literature values. Methods employed in obtaining these half-lives is shown in Table 4.3.

4.2.2 The ^{42}Ca nucleus

The 6^+ state

The ^{42}Ca nucleus has only two valence neutrons outside the outside the doubly magic ^{40}Ca nucleus. The nucleus ^{42}Ca was populated through the ^{45}Sc(p,α)^{42}Ca direct reaction. The excited 6^+ state, at 3189.3 keV level has a known half-life reported by the ENDSF evaluated data sheet as $T_{1/2}$ = 5.28(15) ns [119]. In order to measure the half-life of this state, we set a gate on the feeding 910 keV gamma, which is the $5^- \rightarrow 6^+$ transition and a stop gate set on the $6^+ \rightarrow 4^+$ transition. The time distribution spectrum from which this half-life was measured is shown in Fig.4.21. Using the slope method and from the RF-LaBr$_3$ measurement, we determined this half-life to be $T_{1/2}$ = 4.91(4) ns.

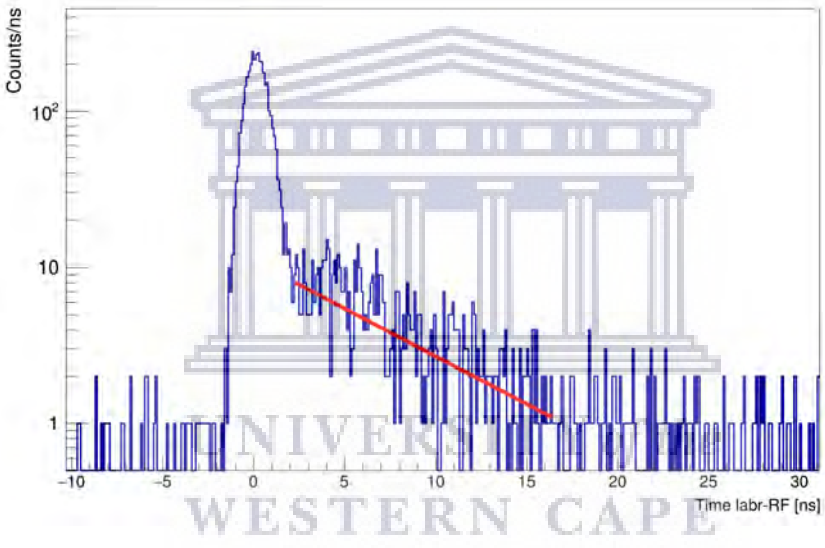

Figure 4.21: Time spectrum obtained by the gating the radio-frequency and a LaBr$_3$:Ce detector used to measure the half-life the 3189.26 keV level for the ^{42}Ca nucleus.

The second 0^+ state

The first excited 0_2^+ state of ^{42}Ca is found at 1837.3 keV energy level and has a known half-life of $T_{1/2}$ = 387(6) ps. This state is populated by an $2^+ \rightarrow 0^+$ associated with the 587 keV γ ray. It is depopulated by an $0^+ \rightarrow 2^+$ transition associated with the 312 keV γ ray. Without background correction, we measured the lifetime of this state to be τ = 387(9) ps. Therefore the half-life of this state without background correction, therefore, is $T_{1/2}$ = 268(6) ps. Figure 4.22 shows the delayed and anti-delayed time distributions from which the centroid difference was determined. The Compton background correction method was employed to correct for the background and

Table 4.4: Experimentally obtained half-lives that have been published for different states of ^{42}Ca. The values obtained in the current work are highlighted in blue. The sub-nanosecond lifetimes are background corrected, those that are corrected via the Compton background correction are indicated by the subscript CB.

Energy level (keV)	J^{π}	Method	Reference	Half-life
3189.3	6^+	Doppler Shift Attenuation	[143]	5.30 (16)ns
3189.3	6^+	Delayed Coincidence Techniques	[144]	3.7 (5)ns
3189.3	6^+	Doppler Shift Attenuation	[145]	5.3 (3)ns
3189.3	6^+	Delayed Coincidence Techniques	[146]	5.52 (15)ns
3189.3	6^+	ENSDF Evaluation	Adopted ENSDF value [119]	5.30 (16)ns
3189.3	6^+	Fast-Timing (RF-$LaBr_3$)	Present work	4.91 (4)ns
3189.3	6^+	Fast-Timing ($LaBr_3$-$LaBr_3$)	Present work	4.29 (5)ns
1837.3	0^+	Direct electronic timing	[147]	387(6)ps
1837.3	0^+	Delayed Coincidence Techniques	[148]	330 (20)ps
1837.3	0^+		[149]	420 (11)ps
1837.3	0^+	ENSDF Evaluation	Adopted ENSDF value [119]	387(6)ps
1837.3	0+	Fast-Timing (GCD_{CB})	Present work	391 (17)ps

the background-timing analyses spectra are shown in Fig.4.23. The PRD correction factor for the (587 → 312) cascade is PRD(587-312) = -323(26) ps. Therefore the lifetime for the first excited 0_2^+ state of ^{42}Ca is calculated as:

$$\tau = \frac{451(4) + 355(44) + 323(26)}{2} = 565(25)\ ps \tag{4.11}$$

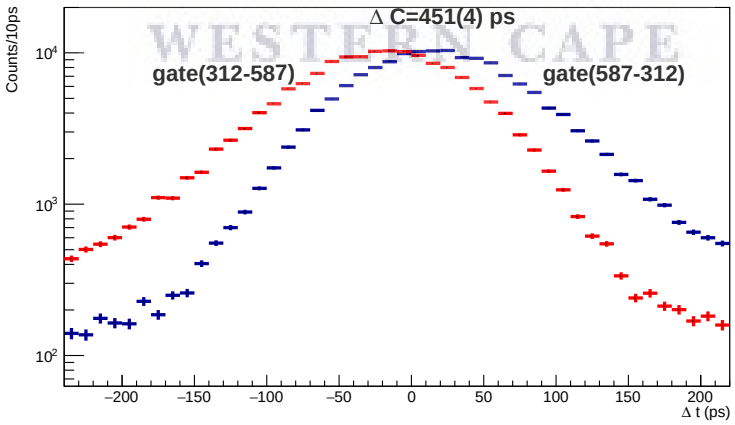

Figure 4.22: Time distribution spectra for the 587 → 312 $\gamma - \gamma$ cascade from which the ΔC value for the first excited 0_2^+ state of ^{42}Ca was obtained.

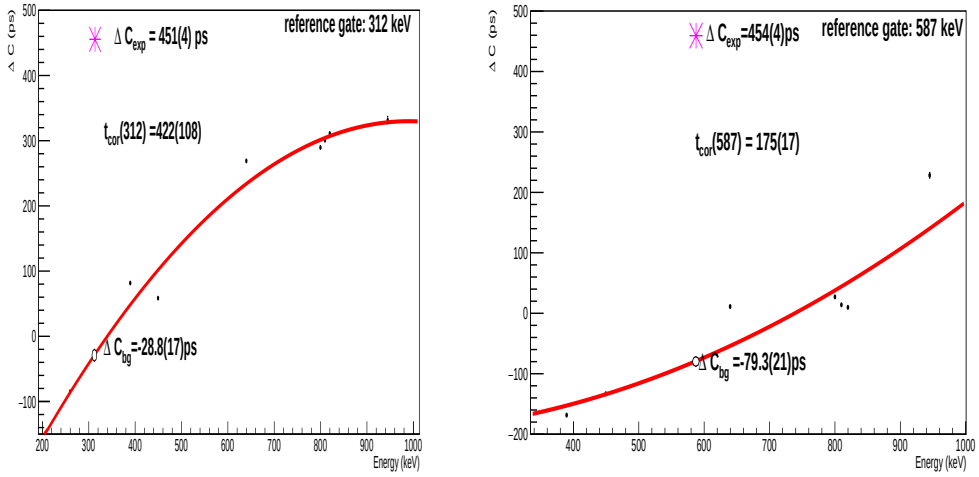

(a) (b)

Figure 4.23: (a) The centroid difference as a function of energy depicting background timing-analysis with the reference gate set at 312 keV with the background gates set around the regions of FEPE at 312 keV and 587 keV. The data points are fitted using a second order polynomial. (b) The centroid difference as a function of energy depicting background timing-analysis with the reference gate set at 587 keV with the background gates set around the regions of FEPE at 312 keV and 587 keV. The data points are fitted using a second order polynomial.

4.3 The rare earth nucleus ^{150}Gd

To gain a broader perspective on the behaviour of nuclei and their general motion as collective motion or single particle motion, this work studied the rare earth nucleus ^{150}Gd. No lifetimes are recorded in the NuDat 2.8 chart of nuclide, [119], for this nucleus. Attempting to measure the lifetimes of this nucleus, we found that some states had no visible shift. It may be that the lifetimes of these states are in the nanosecond range, however, no delayed time distributions were found for these states using the slope method as in the previous cases 4.2.1. Through the GCS method, we were only able to measure one lifetime for this nucleus and the results are presented below.

4.3.1 The 8^+ state

This 8^+ state is found at 2554.1 keV level. The transition that populates this state is an E2 transition ($10^+ \rightarrow 8^+$) associated with the 734 keV γ ray. It is also depopulated by an E2 transition ($8^+ \rightarrow 6^+$) which is associated with the 438 keV γ ray. The centroid difference obtained is $\Delta C = 129(2)$ ps as shown in Fig.4.25. Background-timing analyses spectra from which Compton background was performed are shown in Fig.4.26. The PRD correction factor for the (438 $\rightarrow$ 734) cascade is PRD(434-734) = -31(26) ps. The lifetime of this state is measured as:

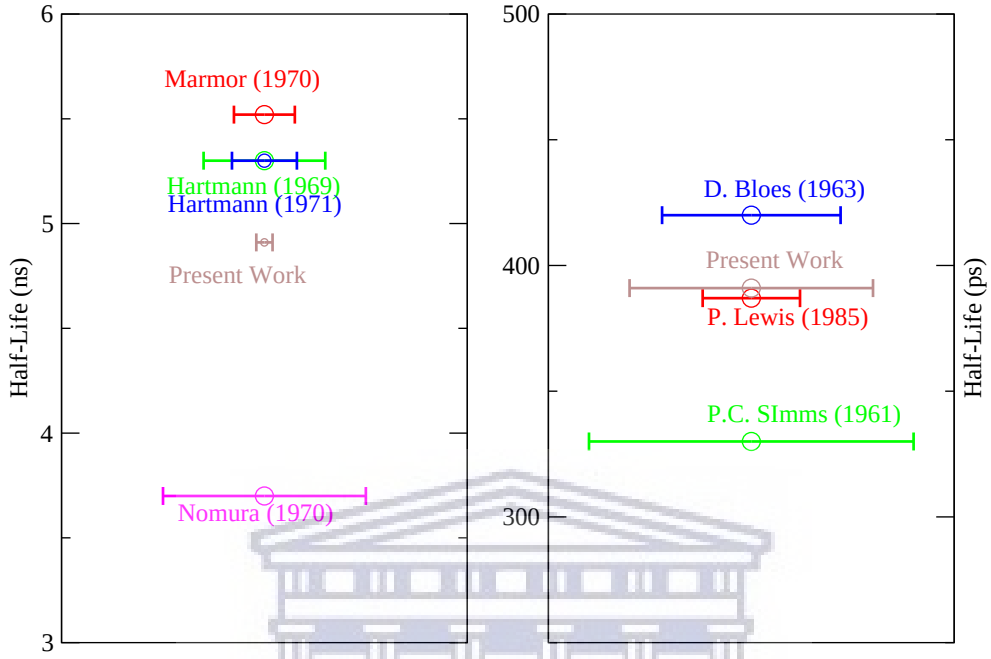

Figure 4.24: Left: The half-life of the 6^+ state at 3189.3 keV level obtained in this work is compared to previously measured obtained literature values. Methods employed in obtaining these half-lives is shown in Table4.4.
Right: The half-life of the 0^+ state at 1837 keV level, symbolized obtained in this work is compared to previously measured obtained literature values. Methods employed in obtaining these half-lives is shown in Table4.4.

$$\tau = \frac{131(2) + 59(2) + 31(26)}{2} = 110(13)\ ps \tag{4.12}$$

The BE(2) value and the intrinsic quadrupole moment obtained for this state are listed in Table4.5.

The $LaBr_3$:Ce and HPGe gated coincidence spectra are shown in Fig.4.27. The HPGe coincidence spectrum was used to select the background gate because of its excellent energy resolution.

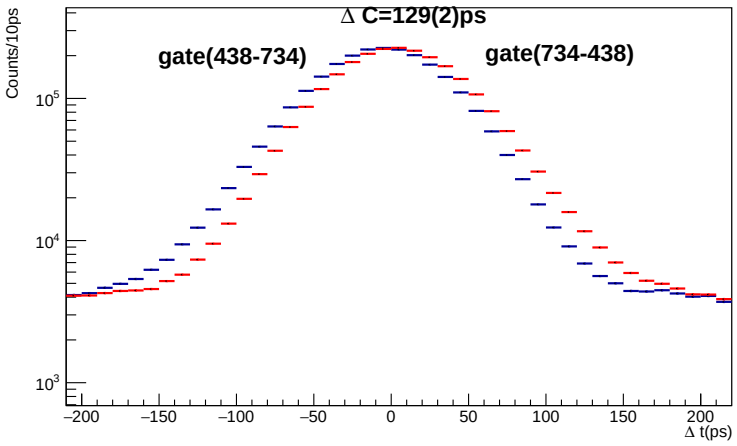

Figure 4.25: Time distribution spectra for the 438 $\rightarrow$ 734 $\gamma - \gamma$ cascade from which the ΔC value for the 8^+ state of ^{150}Gd was obtained.

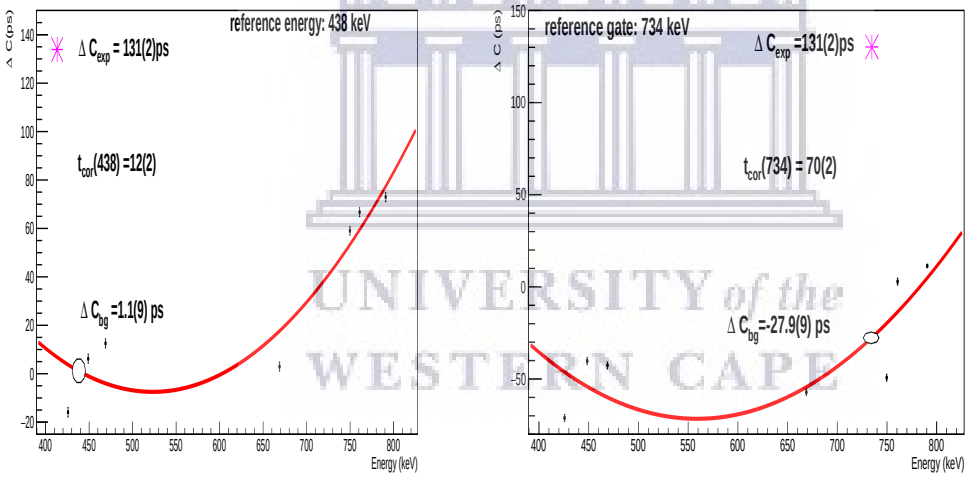

(a) (b)

Figure 4.26: (a) The centroid difference as a function of energy depicting background timing-analysis with the reference gate set at 438 keV with the background gates set around the regions of FEPE at 438 keV and 734 keV. The data points are fitted using a second order polynomial. (b) The centroid difference as a function of energy depicting background timing-analysis with the reference gate set at 734 keV with the background gates set around the regions of FEPE at 438 keV and 734 keV. The data points are fitted using a second order polynomial.

Table 4.5: The experimental lifetimes, (τ), B(E2) and quadrupole moments of ^{150}Gd.

Energy level	(τ) (ps)	B(E2) e^2fm^4	Quadrupole Moment$_{EXP}$ (b)
2554.1	110 (4)	449 (17)	1.50 (2)

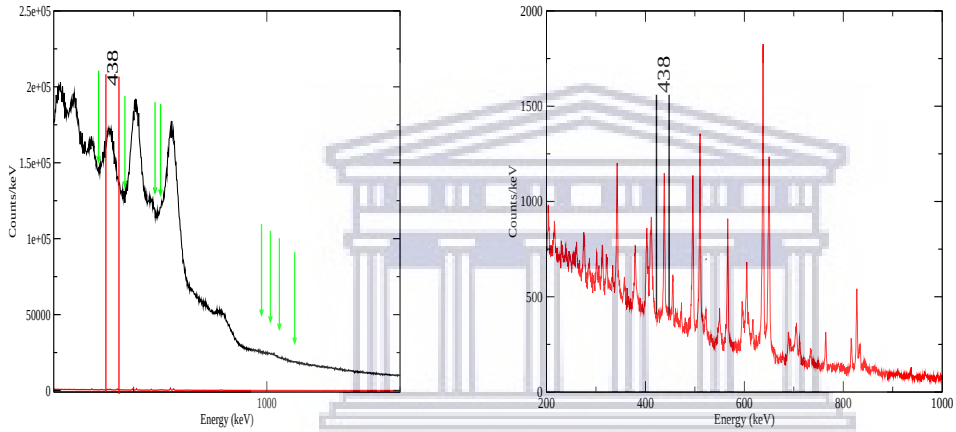

(a) (b)

Figure 4.27: (a) The γ-γ coincidence spectrum gated on the 734 keV. The full energy peak in coincidence with the 734 keV peak, used to obtain the lifetime, is the 438 keV energy. The arrows mark the the regions where the background gates around the full energy peaks were set. The black energy spectrum is the $LaBr_3$:Ce coincidence spectrum and the red energy spectrum is HPGe coincidence spectrum.
(b) The HPGe gated spectrum clearly showing the 438 keV γ ray energy that is in coincidence 734 keV γ ray energy.

4.4 Shell Model calculations of light nuclei in the $A > 40$ and $A \leq 45$ mass region

To better understand the behaviour and the properties of the nuclei in the $A > 40$ and $A \leq 45$ mass region, shell model calculations were performed. Two codes were employed to perform these shell model calculations namely, the NUSHELLX [150] and the KSHELL [151]. For KSHELL calculations, the model space used is the fp model space that was used together with the $gxpf1a.snt$ interaction file [152]. This interaction file contains the single particle energies pf shell together with 195 Two-Body Matrix Elements (TBME) whose starting parameters are derived from a realistic interaction based on the Bonn-C potential. Caurier et al., [50], argues that the model space can produce one or several starting wave functions that can evolve to exact eigenstates which can be viewed as matrix elements of a many-body operator. In choosing a model space, a presumption is made that the bulk of the wave-function is restricted in the chosen model space. Nucleon-nucleon interactions form a complex nuclear structure that can be described by the analytical solutions of their wave-functions. The following single particle levels were included in the model space for both protons and neutrons:

$$0f_{7/2},\ 1p_{3/2},\ 0f_{5/2},\ 1p_{1/2}$$

The current work computed the positive parity states for both ^{44}Sc and ^{42}Ca using this model space and the $gxpf1a.snt$ interaction file.

With NUSHELLX both the positive and negative parity states were computed. The level scheme for ^{44}Sc (Fig.4.29 and ^{42}Ca (Fig.4.30) shows the γ ray transitions as well as excitation energies obtained from NUSHELLX. A different model space and interaction file was used for the different parity states. For the positive parity states, the $fppn$ model space used with the following single particle orbits:

$$1f_{7/2},\ 2p_{3/2},\ 1f_{5/2},\ 2p_{1/2}$$

These orbits for model space were used for both protons and neutrons together with the $gxpf1a.snt$ interaction file. For the negative parity states, $d3f7pn$ model space was used. The model space, fp, used above consists of only negative parity orbitals and the next positive parity orbital is $1g_{9/2}$ which is above the $N = 20 = Z$ sub-shell closure. To obtain negative parity states, a coupling between the negative orbital and positive orbital is needed. Since the $d3f7pn$ model space includes the $1d_{3/2}$ and $1f_{7/2}$ orbitals, it is the suitable candidate to compute the negative parity states. This work used this model space and $w0$ interaction file to obtain negative parity

states and the results are recorded in Table4.7. This model space and interaction file proved to be very useful in producing negative parity states of interest to this work. Negative parity states are not easily produced as the positive parity states. Through conventional shell model calculations, [153] assumed that the negative parity states may a result of excitations out of the $s-d$ shell.

The effective charges were chosen as $e_\pi = 1.5e$ for protons and $e_\nu = 0.5e$ for neutrons , which result from the admixtures of the giant quadrupole states outside the pf model space [154]. The effective charges are due to the center of mass motion of the nucleus such that when a neutron moves it shifts the rest of the nucleus which is charged.

The nuclear observables obtained in this work are compared to those predicted by KSHELL calculations and NUSHELLX in Table4.6 and Table4.7 respectively. The experimental quadrupole moment shown is the intrinsic quadrupole moment and is obtained from Eq.2.15. The KSHELL calculations provide the spectroscopic quadrupole moment while the NUSHELLX calculations provide the intrinsic quadrupole moment.

For ^{44}Sc, the lifetime obtained for the 4^+ state at 349.9 keV level is 4.242 (58) ns and the B(E2) value is 36.8(8) e^2fm^4, as given in Table4.6. The value of the lifetime for this state obtained from NUSHELLX calculations is 0.521 ns which is given in Table4.7. Evidently, the NUSHELLX calculations massively underestimates the lifetime of the 4^+ state. The B(E2) value of this 4^+ state obtained from the measured lifetime agrees fairly well with to those obtained by KSHELL and NUSHELLX, as shown Table4.6 and 4.7. The spectroscopic quadrupole moment for the 4^+ state is-0.424 b as per the KSHELL calculations and the intrinsic quadrupole moment is 0.328 e^{2}fm^4 as per NUSHELLX calculations.

For the 4^- state of ^{44}Sc, the B(E2) value obtained from NUSHELLX is 0.0229 e^2fm^4 was obtained which is much lower than the experimentally obtained value of 174(6) e^2fm^4. The intrinsic quadrupole moment of this state is 3.65 e^2fm^4 according to NUSHELLX and the experimentally obtained value is 0.144(1) b.

For the 6^+ state of ^{42}Ca, the B(E2) value obtained from KSHELL calculations is 2.899 e^{2}fm^4 while from NUSHELLX a B(E2) value of 0.0907 e^{2}fm^4 was obtained. The experimental B(E2) value obtained from measured lifetime is 7.33(2) e^{2}fm^4. The B(E2) value obtained from KSHELL calculations agrees fairly well with the experimental B(E2) value. The spectroscopic quadrupole moment for the 6^+ state of ^{42}Ca is -3.416 b according to KSHELL calculations and the intrinsic quadrupole moment is -10.22 e^{2}fm^4 according to NUSHELLX calculations. In this work, the in-

trinsic quadrupole moment for the 6^+ state was found to be 0.2622(3) b.

The first excited 0_2^+ of ^{42}Ca decays to the 2_1^+, hence the B(E2) value of this state could be measured. From KSHELL calculations, the B(E2) value of 0.0547 e^2fm^4 of the 0_2^+ state was obtained while from NUSHELLX calculations a B(E2) value of 0.0645 e^2fm^4 was obtained. The experimental B(E2) value obtained from the lifetime measurement of this work is 490(19) e^2fm^4. Both KSHELL and NUSHELLX underestimate the collectivity of this state. The experimental intrinsic quadrupole moment of this state is 0.0024 (1) b.

We could not measure B(E2) values for the new lifetimes obtained for the states 6^-, 7^- and 8^- since these decay by M1 transitions and hence no quadrupole moment were determined for these states.

Table 4.6: The lifetimes of different energy levels, (τ), B(E2) and quadrupole moments of ^{44}Sc and ^{42}Ca obtained from shell model calculations using the KSHELL code and experimental values. The values obtained from KSHELL calculations are indicated by the subscript KS and the values obtained from experiments are indicated by the subscript EXP. The effective charges are chosen as $e_\pi = 1.5e$ and $e_\nu = 0.5e$.

Nucleus	Energy level (keV)	J^π	B(E2) $(e^2fm^4)_{KS}$	Quadrupole Moment$_{KS}$ (b)	τ_{EXP}	B(E2)$_{EXP}$ (e^2fm^4)	Quadrupole Moment$_{EXP}$ (b)
^{44}Sc	349.9	4^+	27.049	-0.424	4.242 (58) ns	36.8(8)	0.42(2)
^{42}Ca	3189.26	6^+	2.889	-3.416	7.087(2)ns	7.33 (2)	0.191 (5)
^{42}Ca	1837.3	0_2^+	0.0547		565(22) ps	490 (19)	0.0024 (1)

The sub-nanosecond lifetimes are plotted in Fig.4.28 in which the experimental values are compared with theoretical NUSHELLX values and the adopted literature ENSDF values. The NUSHELLX lifetime obtained for the 3^- state is in reasonable agreement with the experimentally obtained lifetime. The NUSHELLX predicts faster lifetimes for other states.

Single particle orbitals and their location with respect to magic numbers have a direct bearing on the fundamental properties of nuclei. It is possible to have a mixed configuration that contains different configurations of different orbitals. It also possible to have a pure configuration, i.e where no mixing takes place. These configurations are sensitive to the wave-function nuclei and give rise to the characteristics of different states. For example, the location of the $p_{3/2}$ single particle orbital relative to the $f_{7/2}$ single particle orbital may be an important determination factor on whether rotational bands are formed or not, as illustrated by [155] for ^{44}Ti.

Table 4.7: The lifetimes of energy levels, (τ), B(E2) and quadrupole moments of ^{44}Sc and ^{42}Ca obtained from shell model calculations using the NUSHELLX code and experimental values. The values obtained from NUSHELLX calculations are indicated by the subscript NSH and the values obtained from experiments are indicated by the subscript EXP. The effective charges are chosen as $e_\pi = 1.5e$ and $e_\nu = 0.5e$.

Nucleus	Energy level (keV)	J^π	τ_{NSH}	B(E2) (e^2fm^4)$_{NSH}$	Quadrupole Moment$_{NSH}$ (e^2fm^4)	τ_{EXP}	B(E2)$_{EXP}$ (e^2fm^4)	Quadrupole Moment$_{EXP}$ (b)
^{44}Sc	349.9	4^+	521 ns	31.66	0.328	4.242(58) ns	36.8(8)	0.42(2)
^{44}Sc	428.8	3^-	467 ps	0.00726	-0.80	526(15) ps	271(4)	1.1690 (2)
^{44}Sc	631	4^-	75 ps	0.0229	3.65	484(21) ps	174(6)	0.934(2)
^{44}Sc	2210.5	6^-	34 ps			234(13) ps		
^{44}Sc	2606.7	7^-	20 ps			260(15) ps		
^{44}Sc	3364.1	8^-	110 ps			237(17) ps		
^{42}Ca	3189.26	6^+	4.7 x10^{-6} ns	0.0907	-10.22	7.087(2) ns	7.33 (2)	0.191 (5)
^{42}Ca	1837.3	0_2^+	0.0647 ps	0.0645	0.0	565(25) ps	490 (19)	0.0024 (1))

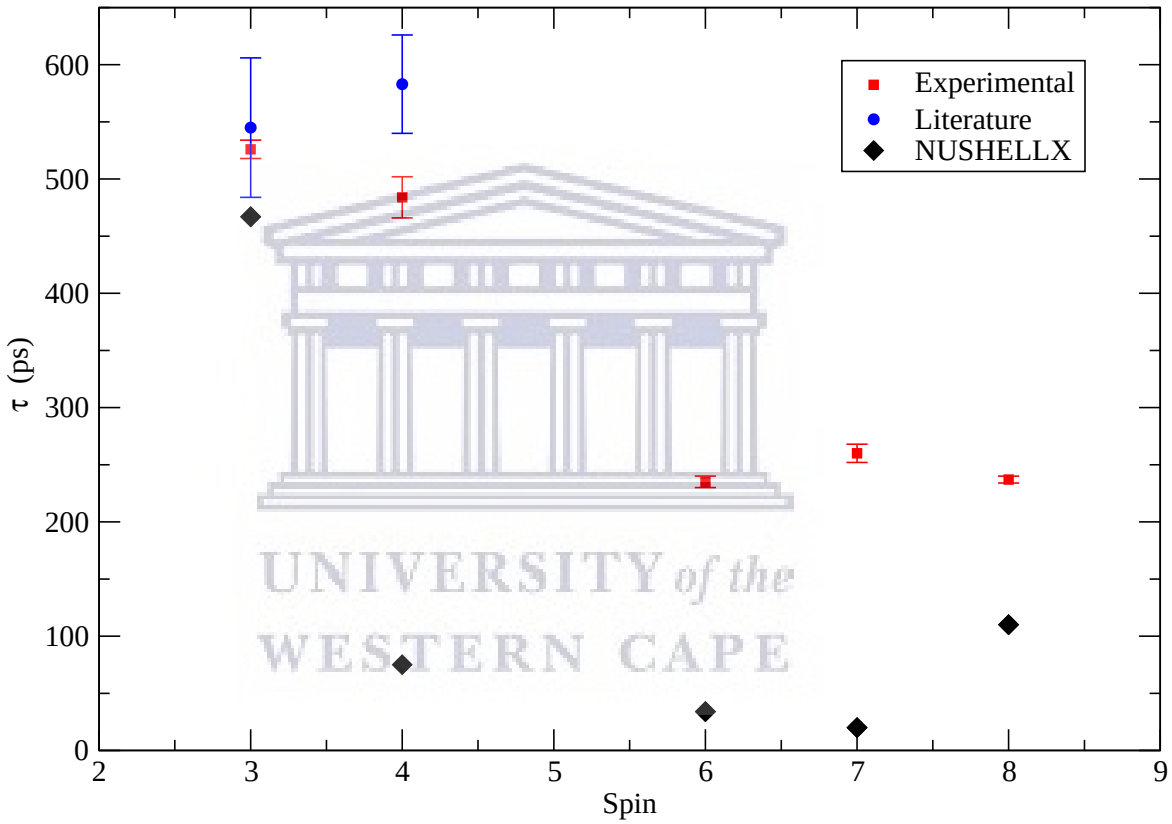

Figure 4.28: The experimentally obtained lifetimes for ^{44}Sc, plotted as a function of spin and compared to NUSHELLX and adopted ENSDF values.

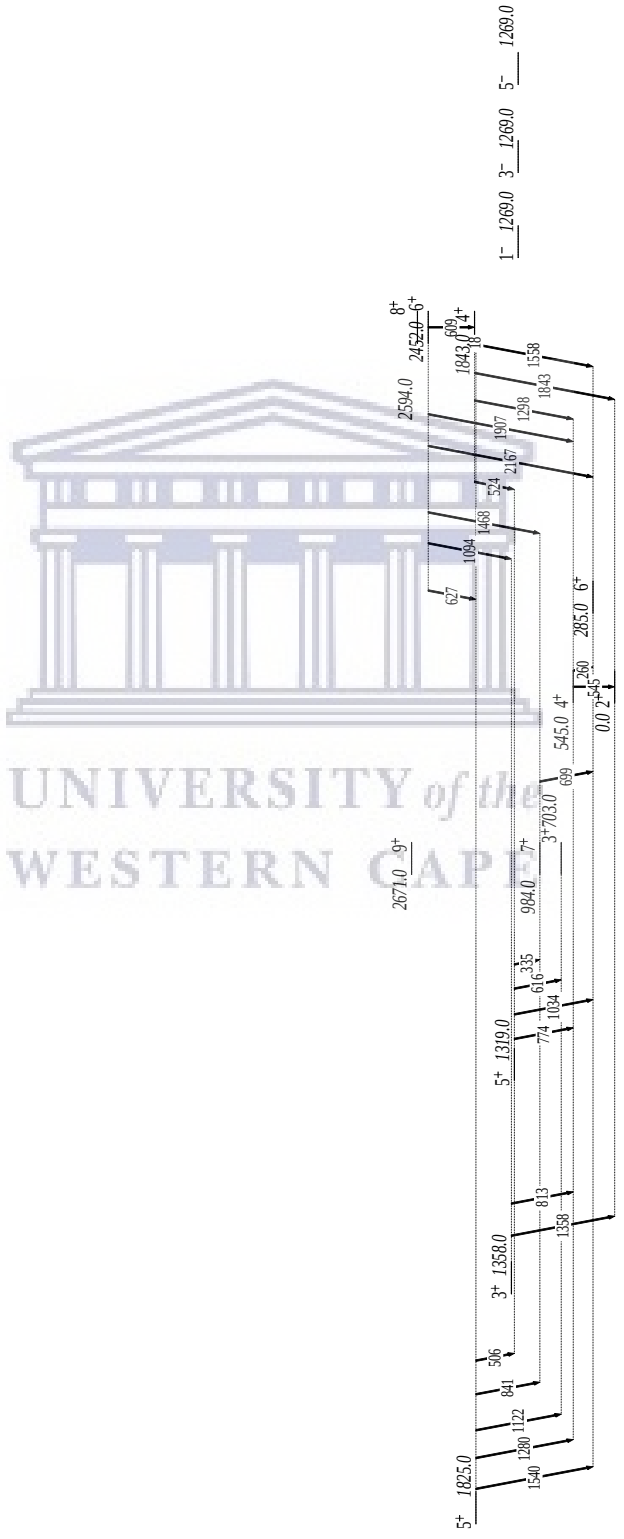

Figure 4.29: The partial level scheme of low lying positive and negative parity states of ^{44}Sc obtained from NUSHELLX. The intensities of the γ ray energies are not represented here.

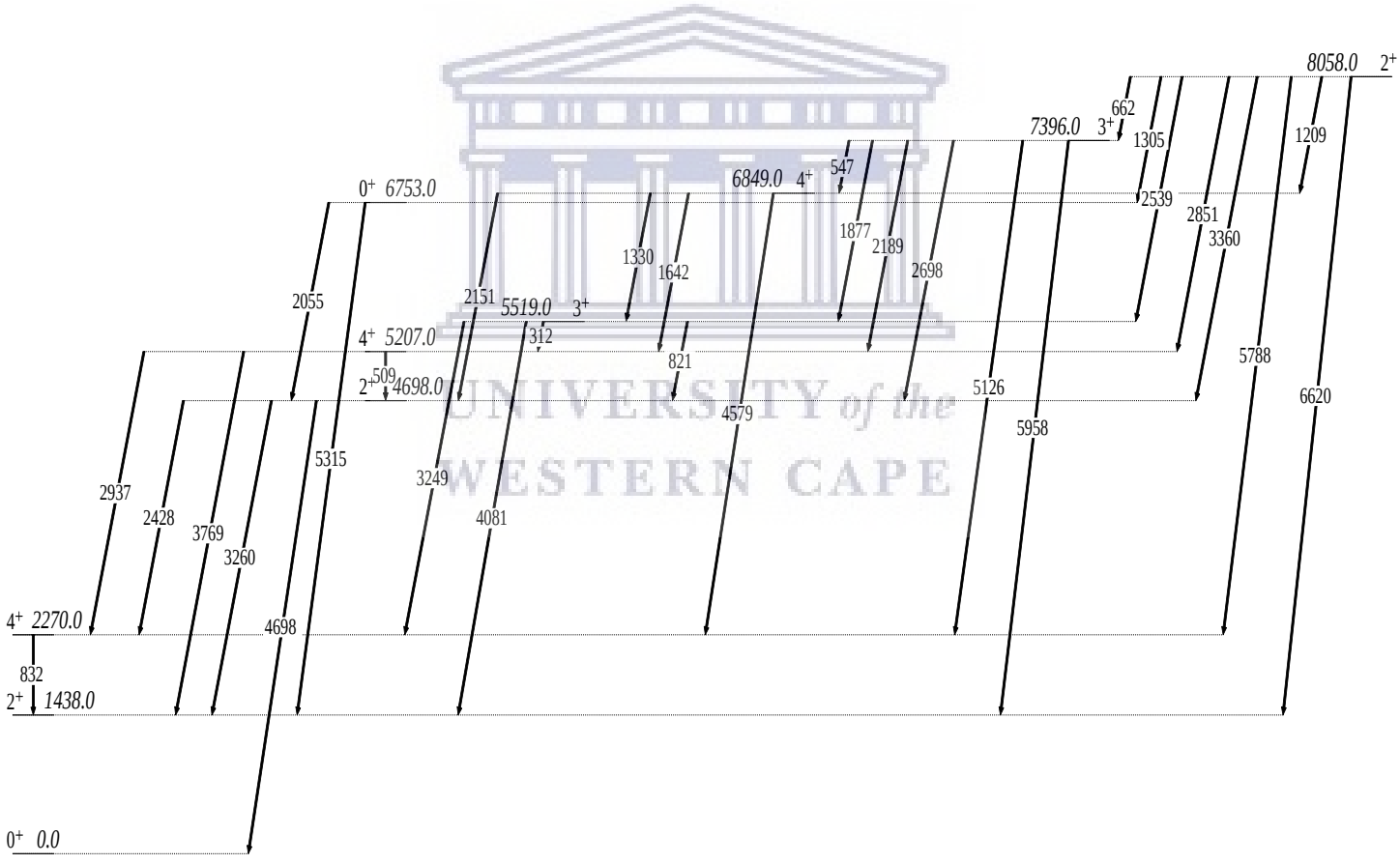

Figure 4.30: The partial level scheme of low-lying positive parity states of ^{42}Ca obtained from NUSHELLX. The intensities of the γ ray energies are not represented here.

Chapter 5

Interpretation of Results

5.1 Discussion

The nuclei in mass region $40 < A < 56$, which in this work are represented by ^{44}Sc, ^{45}Sc and ^{42}Ca are well placed to unveil the key factors of the underlying nuclear structure. This chapter seeks to interpret the results obtained in this work. The comparison between the experimental results as well as the Shell Model calculations is presented. The lifetimes obtained from rare earth nucleus ^{150}Gd , a region where nuclear collectivity and deformation characteristics are commonly investigated, are discussed here.

5.2 Nuclear spectroscopy of light nuclei in the $A > 40$ and $A \leq 45$ mass region

Lifetimes of excited states are an effective probing tool to test shell-model predictions and this work takes advantage of this. The $f_{7/2}$ shell, the valence shell of the ^{44}Sc and ^{42}Ca nuclei, is a nuclear shell in which the phenomenon of shape coexistence is said to exist. This phenomenon was noticed in early γ-ray spectroscopy, where, other than yrast excitations expected for a spherical shape, other regularly spaced low-lying levels characteristic of nuclear deformation were observed [14]. Understanding competition between collective and single particle excitation is key in nuclear spectroscopy, as this is a manifestation of shape coexistence. Nuclei in the fp shell are good candidates to study this competition.

The relatively small number of nucleons in the $A > 40$ and $A \leq 45$ mass region makes these nuclei ideal for studying fundamental nuclear deformations. Studying the systematics of this mass region

gives a broader perspective into the properties of excited nuclear states.

5.2.1 The ^{44}Sc nucleus

The nucleus ^{44}Sc is an odd-odd nucleus with one proton and three neutrons occupying the $f_{7/2}$ shell outside the doubly magic ^{40}Ca core. Apart from the fact that this is an odd-odd nucleus, making it a complex structure, ^{44}Sc exhibits a rather unusual behaviour with several low-lying negative parity states. To probe the properties of this nucleus and others mentioned above, we measured lifetimes of excited nuclear states. The results mentioned in this section are recorded in Tables 4.6 and 4.7. The rather low B(E2) value, 36.8 (8) e^{2}fm^4, obtained for the $4^+ \rightarrow 2^+$ transition signifies the lack of collectivity for the 349.9 keV level. This low B(E2) value may also suggest a poor overlap of the wave-functions between these two states. The $B(E2; 4^+ \rightarrow 2^+)$ value for ^{44}Sc obtained in this work is shown in Fig.5.1, together with $B(E2; 4^+ \rightarrow 2^+)$ values for other Sc isotopes. For these isotopes, lowest $B(E2; 4^+ \rightarrow 2^+)$ value is predicted at $N = 21$ by the KSHELL and at $N = 25$ by the NUSHELLX. Both models predict the highest $B(E2; 4^+ \rightarrow 2^+)$ value to be at $N = 23$. The configuration of the 4^+ state as obtained from NUSHELLX calculations is $\pi f_{7/2}\nu f_{7/2}$, which is a rather pure configuration. This perhaps is supported by the poor wave-function overlap that exists between the 4^+ state and the 2^+ state.

Calculations done by [156] show that the lower spin states of ^{44}Sc are dominated by particle-hole excitations. The $B(E2; 4^+ \rightarrow 2^+)$ values for scandium isotopes depicted in Fig.5.1, are declining as the closed shell is approached at $N = 28$. A steady increase is observed after adding one neutron to the $N = 28$ closed shell for the ^{50}Sc isotope at $N = 29$. For negative parity states above 6 MeV in ^{44}Sc, the energy levels appear to be loosing their collectivity with increasing spin [14]. This observation was made by the studying the trend of the B(E2) values of these states.

In contrast, the 4^- state at an excitation energy level 631 keV has a rather large B(E2) value of 174(6) e^{2}fm^4, signifying an increase in collectivity. This state is most likely dominated by the $\pi g_{9/2}\nu f_{7/2}$ configuration according to the NUSHELLX calculations. The intrinsic quadrupole moment yields a positive value of 0.934(2) b. The 4^- state of ^{44}Sc forms part of the unnatural parity band that is consistent with deformation. The experimentally obtained B(E2) value and intrinsic quadrupole moment supports this.

The present analysis measured the half-life of the 2^- state with the results reported in chapter 4. Together with the 4^- state at 631 keV, the 2^- state at 235 keV forms part of the unnatural parity band, labeled as band D, observed by *Lach et al* [14]. This band can be interpreted as coupling of valence nucleons to the lowest $d_{3/2} - f_{7/2}$ particle-hole excitations of the doubly magic ^{40}Ca core.

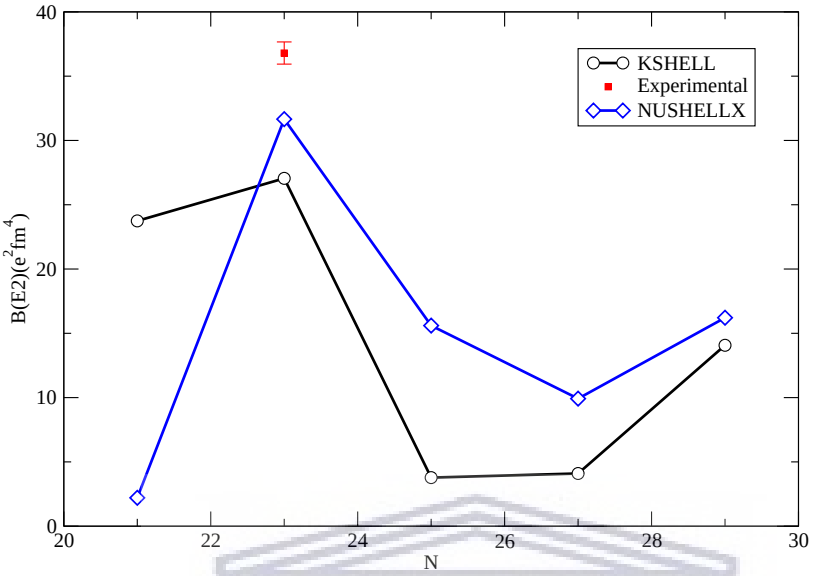

Figure 5.1: The experimental $B(E2; 4^+ \rightarrow 2^+)$ value for ^{44}Sc (red) obtained from the measured lifetime and the $B(E2; 4^+ \rightarrow 2^+)$ values for scandium isotopes obtained from KSHELL and NUSHELLX calculations. Lines connect the data points to guide the eye.

As with other neighbouring nuclei, this unnatural-parity band displays a rotational character [14]. In particular, rotational like bands with negative parity have been observed in ^{43}Sc, ^{45}Sc [157] and in ^{43}Ca [158]. The development of rotational structures in these nuclei shows a likelihood of configuration mixing within the $s-d$ shell.

The 3^- state at 428.8 keV level shows a much more collective nature with experimentally obtained BE(2) value of 271(4) e^{2}fm^4. The intrinsic quadrupole moment of this state is 1.1690(2) b. This state is most likely dominated by the $\pi g_{9/2}\nu f_{7/2}$ configuration according to the NUSHELLX calculations. The results obtained for this state show a character that is consistent with a deformed state.

The yrast positive-parity sequence of levels is formed by coupling of valence nucleons in the $f_{7/2}$ shell. This yrast positive-parity structure is representative of a spherical nuclear shape. The unnatural-parity band, on the hand, has some intra-band transitions decaying into the yrast positive parity band. The existence of both the spherical and deformed bands is a sign of possible shape coexistence, which is typical of the $f_{7/2}$ shell.

Table 5.1: The lifetimes energy levels, (τ), B(E2) and quadrupole moments of ^{44}Sc obtained from shell model calculations using the NUSHELLX code using the *GX1APN* and *fpd6pn* interaction files. The values obtained for the respective interaction files are indicated by the subscript GX and by the subscript FPD.

Nucleus	Energy level (keV)	Energy level$_{GX}$ (keV)	J^π	τ_{NS} (ns)	B(E2) (e^{2}fm^4)$_{GX}$	Energy level$_{FPD}$	τ_{FPD} (ns)	B(E2)$_{FPD}$ (e^{2}fm^4)
^{44}Sc	349.9	545	4^+	0.3617	31.66	529	0.3755	36.36
^{44}Sc	234.7		2^-				6.160(76)	128.49

Studies by *Stoitcheva et al.* [156, 159] have indicated the existence of collective intruder states in ^{44}Sc and other nuclei in the $A = 44$ region. Intruder states in ^{44}Sc are represented by the unnatural parity band and are more deformed than other regular structure, which is characteristic of intruder states. In general, unnatural parity intruder states in $A \sim 44$ from lower fp shell linked with cross-shell excitations across the $N = Z = 20$ closed shell that is responsible for shape coexistence and appearance of collective rotational excitations [160], [161], [14].

Low $B(E2 : 0^+ \rightarrow 2^+)$ values have been observed in $N = 20$ isotones with $Z = 14$, $Z = 16$, $Z = 18$, and $Z = 20$ [30]. It is argued by *Sorlin et al.* [30] that the low $B(E2; 0^+_1 \rightarrow 2^+_1)$ in ^{40}Ca is due to quadrupole excitations to the fp shells that can only proceed through small matrix elements provided by the overlap of the sd and fp wave-functions. There is, however, a sudden sharp increase observed for the B(E2) value at $Z = 22$ that is evident after adding protons to $Z = 20$. This rapid increase in the B(E2) value may be due to $2p - 2h$ neutron excitations from sd to the fp shells if one considers the possibility that valence neutrons do include the fp orbits. This sudden sharp increase in the B(E2) value is also observed when two protons are added to ^{16}O to form ^{18}Ne, with $Z = 10$ and $N = 8$. The doubly magic ^{16}O has low B(E2) value [30], consistent with the doubly magic ^{40}Ca. In fact a similar trend is observed at the closed shell $N = 28$, confirming a decrease of collectivity when approaching closed shell.

Ibbotson et al. [162] studied the systematic behaviour of $B(E2; 0^+_1 \rightarrow 2^+_1)$ in silicon isotopes and found that as the neutron number increases, the degree of collectivity decreases smoothly and monotonically until closed shell is reached at $N = 20$. As more neutrons are added to the $N = 20$ closed shell the collectivity is then seen to be regained. The closeness of the $f_{7/2}$ and $p_{3/2}$ neutron orbits for $2\hbar\omega$ configurations in $N = 20$ results in the two neutron configuration tending towards collectivity [58].

By way of testing the sensitivity of the nuclear observables to different interaction files, this current

analysis used NUSHELLX with the *fpd6pn* [163] interaction file. The effective charges were still maintained as $e_p = 1.5$ and $e_n = 0.5$. The results are similar to those obtained when using the *GX1APN* interaction file. The results for the two interaction files are shown in the Table 5.1 It apparent from these results that the nuclear observables are not sensitive to different interaction files as they are to the the model space.

The intrinsic quadrupole moment shows a decline with increasing spin, see Fig.5.2, for the excited states 4_1^+, 5_1^+, 6_1^+. Both the NUSHELLX and KSHELL results show a similar trend, with a noticeable difference only at $Spin = 6\hbar$. The intrinsic quadrupole moments for these states are indicative of prolate deformation.

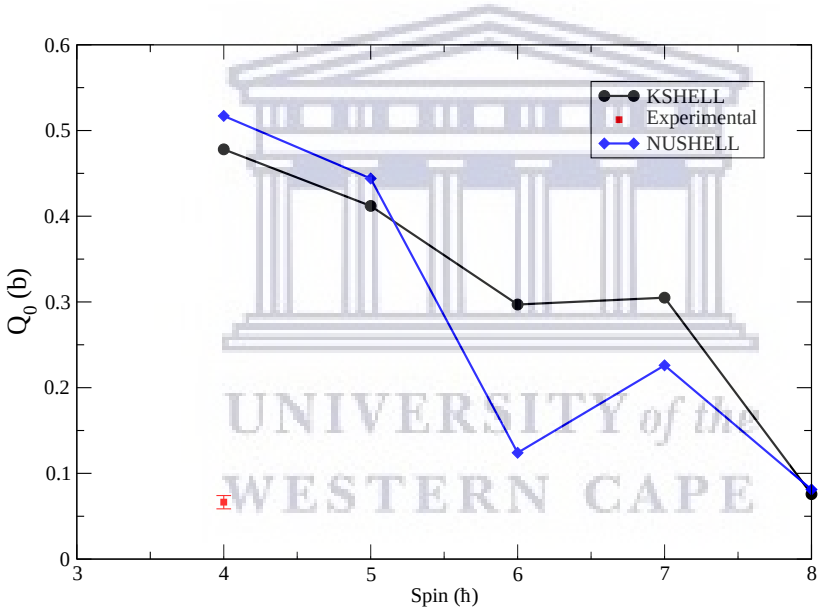

Figure 5.2: Intrinsic quadrupole moments for first excited states 4_1^+, 5_1^+, 6_1^+, and 7_1^+ for ^{44}Sc as a function of spin.

5.2.2 The ^{42}Ca nucleus

The other nucleus of interest in this work is ^{42}Ca, populated by the reaction ^{45}Sc(p,α) ^{42}Ca. The half-life of the 6^+ state at 3189.26 keV measured in this work is $T_{1/2} = 4.912(4)$ ns, see Table 4.3. The 6^+ state decays to the 4^+ state through the 436.9 keV γ ray. The lifetime of this state is rather longer compared to other known lifetimes in ^{42}Ca. The B(E2) value obtained from the

current measured lifetime is 7.33 (2)e^2fm^4. The B(E2) values obtained from the KSHELL and NUSHELLX are listed in Table 4.6 and 4.7 respectively, including values obtained from this work. The B(E2) value obtained in this work is similar to that obtained by Nomura et al [146]. The low B(E2) value at the 6^+ state is suggestive of loss in collectivity in medium to high lying states in ^{42}Ca. Figure 5.3 illustrates the B(E2) values, for the 6^+ state, of calcium isotopes as a function of the neutron number N obtained from this work as well as from KSHELL and NUSHELLX. The B(E2) values reach a peak at $N = 24$ and then decline at $N = 26$ and again increasing at $N = 28$, which is shell closure.

For the first excited 0_2^+, the experimentally obtained BE(2) value is 490(19) e^2fm^4, signifying a highly collective state. This result sopports the results obtained by Hartmann and Grawe [145], whose experimentally obtained BE(2) value is 556(34) e^2fm^4. The intrinsic quadrupole moment of this state is 0.0024(1) b. The first excited 0_2^+ state of ^{42}Ca decays to first excited 2^+ state of the ground state band. Casten and Von Brentano suggested that the lowest 0^+ bands should be understood as phonon excitations [164, 165]. This is due to the fact that 0^+ bands in deformed nuclei decay predominantly to the $\gamma-$ band rather than to the ground state band. There are cases where the first excited 0_2^+ does not decay to the $\gamma-$ band and in fact it may lie lower than $\gamma-$ band [166]. Because of this, Gunther et al [167] emphasized that it is not possible to conclude that the origin of this state has two-phonon $\beta-$ vibration character. It is widely accepted that the 0_2^+ state of ^{42}Ca is very deformed 2 neutrons and 2 protons in the $f_{7/2}$ shell and 2 protons holes in the $d_{3/2}$ shell. The 0_2^+ state of ^{40}Ca, which is a 4p-4h configuration, is more deformed that of ^{42}Ca [168]. Another structure that can be found in ^{40}Ca is the octupole vibration decaying a 27 Wu E3 transition.

With just two neutrons added to the doubly magic ^{40}Ca core, ^{42}Ca is the best candidate, as with other nuclei around shell closure, for studying the coupling between particles and collective excitations.

The first excited 2^+ state is at 1524.71 keV while for ^{44}Sc the 2^+ state is the ground state . Since the ground state of the ^{42}Ca nucleus is paired more energy is required to break the paired nucleons and excite them to the next level.

The $_{20}$Ca isotopic chain is well suited to derive neutron-neutron or proton-neutron effective interactions and is a good testing ground for nuclear models. This due to the fact that the shell gap is large enough to avoid coupling between single particle states and collective excitations at low energy. Adding more neutrons to the doubly magic ^{40}Ca core leaves it hardly polarized, making the neutron single-particle energies to act as references to constrain effective nuclear interactions

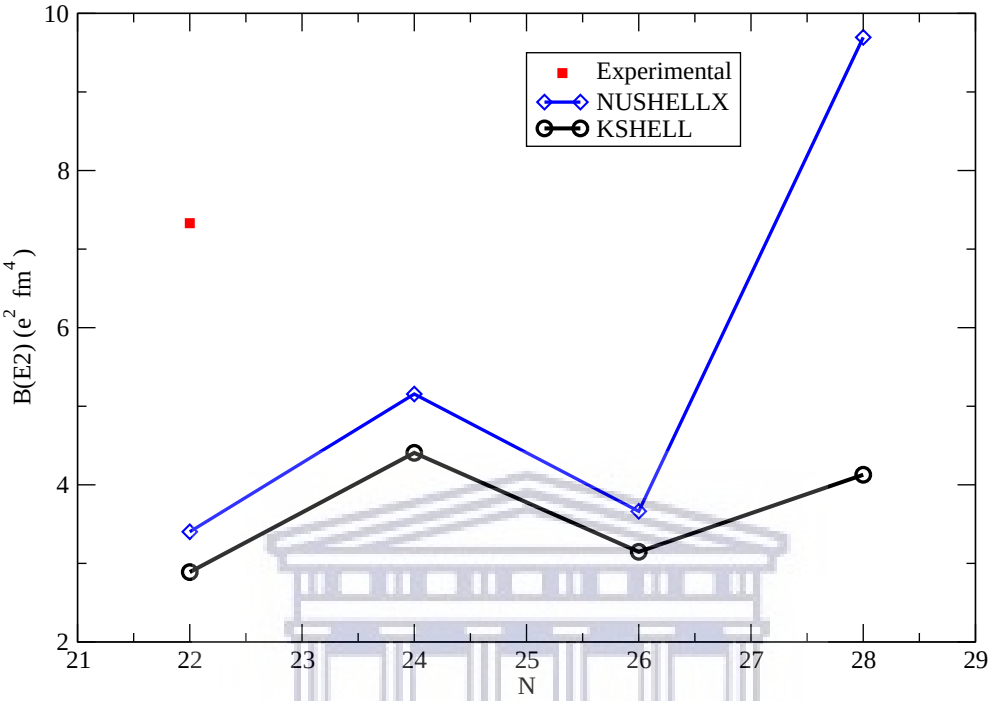

Figure 5.3: The experimental $B(E2; 6^+ \rightarrow 4^+)$ value for ^{44}Ca (red) obtained from the measure lifetime and the $B(E2; 6^+ \rightarrow 4^+)$ values for calcium isotopes obtained from KSHELL and NUSHELLX calculations. Lines connect the data points to guide the eye.

for shell model calculations [30]. To comprehend the behaviour of the nucleus of interest, ^{42}Ca, with respect to its neighbouring nuclei shell model calculations for different $_{20}$Ca isotopes were performed. The excitation energy of the first excited 2^+ state for the $_{20}$Ca isotopic chain obtained from KSHELL calculations is shown in Fig.5.4. The values of excitation energy of the first excited 2^+ state for the $_{20}$Ca isotopic chain obtained from NUSHELLX are equivalent to that of KSHELL. The excitation energies for the $N = 22$, $N = 24$, $N = 26$ and $N = 30$ are relatively similar, with their behaviour being typical of weak core excitations at low excitation energy. The ^{48}Ca nucleus at $N = 28$ exhibits a sharp increase of the excitation energy of the first excited 2^+ state. This increase is characteristic of a strong sub-shell closure and is consistent with what is expected for doubly magic nuclei. The prevailing $[f_{7/2}^{-1}, p_{3/2}]$ component for the 2^+ yrast state of ^{48}Ca is said to be a non collective $1p-1h$ configuration [169]. The fact that the neutron $f_{7/2}$ shell of ^{48}Ca is filled is indicative that the 2^+ state comes mainly from particle-hole excitations across the $N = 28$ gap. The 2^+ state, as with other positive parity states, is not formed by $1p-1h$ excitations in the

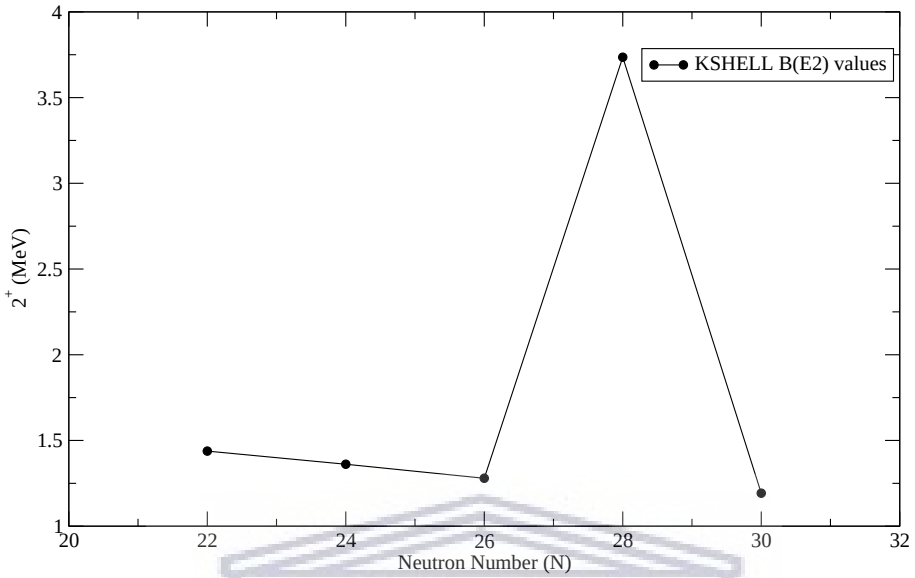

Figure 5.4: The excitation energies for the first excited 2^+ state for $_{20}$Ca isotopes obtained from KSHELL. Lines connect the data points to guide the eye.

case of $N = 20$ magic number. This is because the $N = 20$ magic number exists between between two shells of the harmonic oscillator well having opposite parities [30].

Warbuton et al [58] assumed that the low $f_{7/2}$ shell becomes low in energy giving rise to a reduced *sp* shell and anomalous inverted structure was proposed which is based on 2p-2h neutron cross shell configurations in ground state. It is this 2p-2h neutron excitation from the *sd* to the *fp* shells that are likely to result in an increase in BE(2) values, thus resulting in a gain of collectivity. It is expected that the dominance of the 2p-2h neutron excitation will dominate the *sd* configuration if the single-particle energy difference between the $d_{3/2}$ and *fp* shell is reduced. The nucleus of interest ^{42}Ca, is a Z=20 nucleus whose gap is bound by states of opposite parities. It is for this reason that a minimum of 2p-2h is required to induce quadrupole deformation [30]. The intrinsic quadrupole moment for ^{42}Ca decreases with increases spin, as shown in Fig.5.5. A similar trend was observed for ^{44}Sc as well.

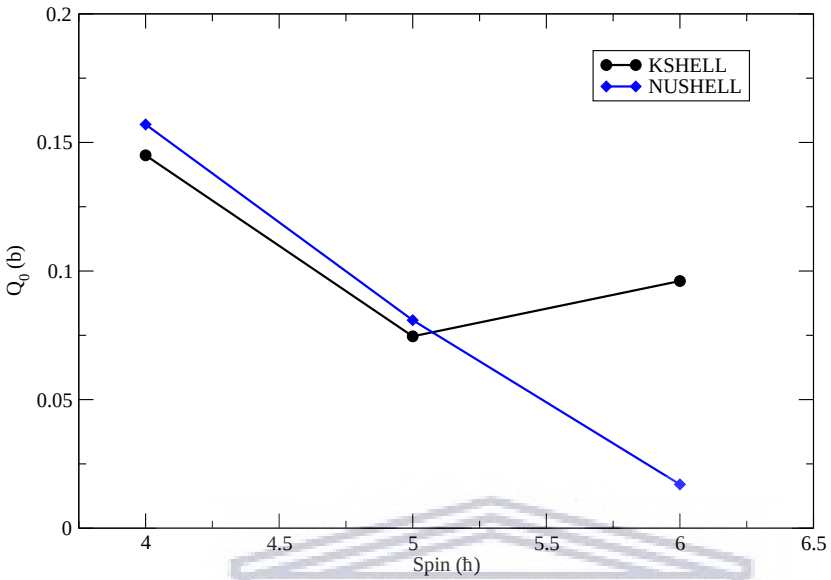

Figure 5.5: The Intrinsic Quadrupole Moment as a function as function of spin.

5.3 Nuclear spectroscopy of nuclei in the rare earth region

The rare earth nucleus, ^{150}Gd, which forms part of this analysis, are even-even nuclei that are ideal for investigating rotational properties and phenomenon such as superdeformation. This is an $N = 86$ nucleus and it provides a platform to study the origin of collective rotation and its progression with rotational frequency. Studying the reduced transition probabilities that are obtained from lifetime measurements provides a solid test to theories of collective motion of nuclei. A more detailed study on the underlying physics of this nucleus is being undertaken by Mdletshe et al. [170] and the purpose of this work was to observe potential lifetimes.

5.3.1 The ^{150}Gd nucleus

With four neutrons outside the $N = 82$ shell closure, ^{150}Gd lies is in the transition region, where nuclei exhibit behavioural change between rotational character and spherical change. Furthermore, nuclei in the $A = 150$ region are well known for their superdeformed states at high angular momentum ([171] is an example of this). The hybrid array used in the current analysis gives the opportunity to measure lifetimes in the $N = 86$ nucleus where no lifetimes are reported in the data sheets for deformed nuclei. The BE(2) value of 449(17) e^2fm^4, see Table 4.5, obtained from the

measured lifetime indicates that the 8^+ state as highly collective. This may indicate that this state is part of a deformed structure. Other $N = 86$ rare earth nuclei, ^{148}Sm and ^{146}Nd, have known lifetimes recorded for the 2^+ and 4^+ state [119]. The nucleus ^{150}Gd has many superdeformed bands and a detailed investigations into its low and medium spins can uncover the collective nature in deformed nuclei. Besides not having known lifetimes, this nucleus does not have any known yrast traps. This is the lack of yrast traps may likely be due to its number of protons , $Z = 64$, being at sub-shell closure.

Chapter 6

Conclusion

Eight 2" x 2" $LaBr_3$:Ce detectors used in conjunction with the 16 channel all-digital waveform 500 MHz acquisition card, PIXIE16 were commissioned at iThemba Laboratory for Accelerator Based Sciences. The results presented here give insight of the performance of the 2" x 2" $LaBr_3$:Ce detectors when used in conjunction with a digital pulse processing (DPP) module and electronic read-out card. The properties of this scintillator detector, such as energy resolution, efficiency and time resolution were thoroughly investigated and reported here. Analysis was done to gauge the performance of the 2" x 2" $LaBr_3$:Ce detectors in a hybrid array. This study demonstrated the significance of having the best energy resolution, optimal time resolution and high efficiency in modern γ-ray spectroscopy. We were able to measure lifetimes in the nanosecond range using the slope method and lifetimes in the sub-nanosecond range using the Generalized Centroid Shift method. Underlying nucleonic properties of light nuclei ^{44}Sc and ^{42}Ca and the heavy rare earth nucleus ^{150}Gd were studied through electronic technique of direct measurement of lifetimes. Nuclear models and predictions were put to the test in this work. Known lifetimes for ^{44}Sc and ^{42}Ca were extracted with new lifetimes for ^{44}Sc and ^{150}Gd obtained. The phenomenon of shape coexistence that is associated with nuclei in the $f_{7/2}$ shell was shown to exist in ^{44}Sc in this work. The collective nature of ^{42}Ca that may result from 2p-2h neutron excitations is observed in this work. The lifetimes of excited states in ^{150}Gd were explored and one state, the 8^+ state was measured successfully. This state proved to be highly collective.

The 2" x 2" $LaBr_3$:Ce detectors prove to be very useful in unearthing the underlying physics of different nuclei. With these detectors, observables that are sensitive to the structure of the intrinsic wavefunction can be extracted. With the proposed expansion and commissioning of new Arrays at

iThemba Laboratory for Accelerator Based Sciences more interesting physics will be obtained when using these portable detectors in these arrays. In this work we were able to obtain lifetimes without active shielding. Improved quality of results may be obtained in future experiments through active shielding, since this does more to minimize Compton background. Indeed this study has shown, in but a small measure, the unlimited physics potential that exists in fast-timing methods.

Bibliography

[1] A. Giaz *et al.*, *Nucl. Instr. Methods*, vol. A 729, p. 910, 2013.

[2] L. M. Fraile, *J. Phys. G: Nucl. Part. Phys.*, vol. 094004, 2017.

[3] G. D. Dracoulis *et al.*, *J. Phys. A: Math. Nucl. Gen.*, vol. 6, p. 1772, 1972.

[4] R. J. Keddy, *S.Afr.J.Phys.*, vol. 6, p. 79, 1983.

[5] A. R. Poletti *et al.*, *Phys. Rev. C*, vol. 13, pp. 1180–1193, 1976. [Online]. Available: https://link.aps.org/doi/10.1103/PhysRevC.13.1180

[6] J. J. Kolata *et al.*, *Phys. Rev. C*, vol. 10, p. 1663, 1974.

[7] J. P. Coffin *et al.*, *Phys. Rev. C*, vol. 14, p. 861, 1976.

[8] F. Brandolini *et al.*, *Lett.Nuovo Cim.*, vol. 12, p. 433, 1975.

[9] J. W. Olness *et al.*, *Phys. Rev. C*, vol. 11, p. 110, 1975.

[10] N. Wust *et al.*, *Journal of Physics G: Nuclear Physics*, vol. 1, p. 1, 1975.

[11] K. P. Lieb and M. Uhrmacher, *Z.Phys*, vol. 267, p. 399, 1974.

[12] R. Hartmann *et al.*, *Nucl. Phys A*, vol. 123, pp. 437–438, 1969.

[13] E. K. Johansson, *Eur.Phys.J.A*, vol. 27, pp. 157–165, 2006.

[14] M. Lach *et al.*, *Eur.Phys.J.A*, vol. 25, pp. 1–4, 2005.

[15] P. Fallon *et al.*, *Phys. Lett.*, vol. B218, p. 137, 1989.

[16] P. Lipas, *Phys. Scr.*, vol. 27, p. 8, 1983.

[17] H. Cember, *Introduction to Health Physics*. The McGraw-Hill Companies, Inc., 2009.

[18] A. H. Compton, *Phys. Rev.*, vol. 21, p. No5, 1923.

[19] [Online]. Available: http://hyperphysics.phy-astr.gsu.edu/hbase/quantum/compton.html

[20] G. F. Knoll, *Practical Gamma-ray Spectrometry.* (John Wiley and sons, Ltd)., 1979.

[21] G. R. Gilmore, *Radiation Detection and Measurement.* (John Wiley and sons, Ltd)., 2008.

[22] K. S. Krane, *Introductory Nuclear Physics.* John Wiley and Sons, 1998.

[23] J. Suhonen, *From Nucleons to Nucleus.* (Springer), 2007.

[24] H. Morinaga and T. Yamazaki, *In-beam Gamma-ray Spectroscopy.* (North-Holland Pub. Co.), 1976.

[25] P. J. Nolan and J. F. Sharpey-Schafer, *Rep. Prog. Phys.*, vol. 42, p. 1, 1979.

[26] H. Bateman, *Proc. Camb. Phys. Soc*, vol. 15, p. 423, 1910.

[27] P. Ring and P. Schuck, *The Nuclear Many Body Problem.* (Springer-Verlag, New York), 1980.

[28] T. K. Alexander and J. S. Forster, *Adv. Nucl. Phys.*, vol. 10, p. 197, 1978.

[29] M. Moszyński *et al.*, *Nucl. Instr. and Meth*, vol. A567, p. 31, 2007.

[30] [Online]. Available: http://dx.doi.org/10.1016/j.ppnp.2008.05.001

[31] R. F. Casten, *Nuclear Structure from a Simple Perspective, Second ed.* Oxford University Press, USA,, 2001.

[32] M. G. Mayer, *Phys. Rev.*, vol. 74, p. 235, 1948.

[33] F. G. Moradi, "Experimental nuclear structure studies in the vicinity of the n = z nucleus ^{100}Sn and in the extremely neutron deficient ^{162}Ta nucleus," Ph.D. dissertation, University Center, Sweden, 2014.

[34] J. A. Sheikh *et al.*, *Phys. Rev.*, vol. C 77, p. 014303, 2008.

[35] J. Bardeen *et al.*, *Phys. Rev.*, vol. 106, pp. 162–164, 1957.

[36] N. N. Bogoliubov, *Usp. Fiz. Nauk*, vol. 67, p. 549, 1959.

[37] G. H. Jehangir *et al.*, *Nucl. Phys*, vol. A968, p. 48, 2017.

[38] J. Marcellino *et al.*, *Nucl. Phys*, vol. C96, p. 034319, 2017.

[39] R. Palit *et al.*, *Eur.Phys.J*, vol. A53, p. 90, 2017.

[40] A. Navin *et al.*, *Phys. Lett.*, vol. B767, p. 480, 2017.

[41] G. H. Bhat *et al.*, *Nucl. Phys.*, vol. A947, p. 127, 2016.

[42] T. Nikśi *et al.*, *Phys. Rev*, vol. C79, p. 034303, 2009.

[43] G. H. Li *et al.*, *Phys. Rev*, vol. C79, p. 054301, 2009.

[44] T. Otsuka *et al.*, *Nucl.Phys.*, vol. 47, p. 319, 2001.

[45] A. de Shalit and M. Talmi, *Nuclear Shell Theory.* Academic Press,New York and London, 1963.

[46] R. Bark *et al.*, *J. Phys.*, vol. G17, p. 1209, 1991.

[47] A. de Shalit and M. Goldhaber, *Phys.Rev.*, vol. 92, p. 1211, 1953.

[48] T. S. Kuo and S. S. M. Wong, *Topics in Nuclear Physics,vol I, ch III.* Springer, Berlin, 1981.

[49] R. D. Lawson, *Theory of the Nuclear Shell Model.* Claredon Press, Oxford, 1980.

[50] E. Caurier, *Rev.Mod.Phys.*, vol. 77, p. 2, 2005.

[51] L. Coraggio *et al.*, "Shell-model calculations and realistic effective interactions," 2009.

[52] B. A. Brown, *Ann.Rev. Nucl.Part.Sci*, vol. 38, pp. 29–66, 1988.

[53] R. Machleidt *et al.*, *Phys. Rep. J. Phys.*, vol. G 149, p. 1, 1947.

[54] W. N. Cottingham *et al.*, *Phys. Rev.*, vol. D 8, p. 800, 1973.

[55] R. Vinh-Mau *et al.*, *Phys. Lett*, vol. B 44, p. 1, 1973.

[56] M. Lacombe *et al.*, *Phys. Rev. D*, vol. D 12, p. 1495, 1975.

[57] M. Lacombe. *et al.* , *Phys. Rev. D*, vol. C 21, p. 861, 1980.

[58] E. K. Warburton *et al.*, *Phys. Rev.*, vol. C41, p. 1147, 1990.

[59] K. Wimmer *et al.*, *Phys. Rev. Lett.*, vol. 105, p. 252501, 2010.

[60] E. Caurier *et al.*, *Phys. Rev.*, vol. C 90, p. 014302, 2014.

[61] F. Nowacki *et al.*, *Phys. Rev.Lett.*, vol. 117, p. 272501, 2016.

[62] J. L. Wood *et al.*, *Phys.Reports.*, vol. 215 101, p. 69, 1985.

[63] F. Raimondi and C. Barbieri, *Phys. Rev.*, vol. C 100, p. 024317, 2019.

[64] M. S. Sandel *et al.*, *Z. Physik*, vol. A 280, pp. 259–266, 1977.

[65] A. Bohr and B. R. Mottelson, *Nuclear Structure*. Benjamin, New York, 1975.

[66] W. Greiner *et al.*, *Nuclear Models*. Springer, 1996.

[67] C. Wheldon, "K-isomerism at high-spin beyond fusion limit states," Ph.D. dissertation, University of Surrey, 1999.

[68] S. G. Nilsson, *Mat. Fys. Medd. Dan. Vid. Selks.*, vol. 29, p. 16, 1955.

[69] B. R. Mottelson, *Phys. Rev.*, vol. 99, p. 1615, 1955.

[70] D. R. Zolnowski *et al.*, *Phys. Rev*, vol. C21 (6), p. 2556–2574, 1955.

[71] R. F. Casten, *Phys. Rev.Lett*, vol. 47(20), p. 1433, 1981.

[72] L. G. Elliot and P. E. Bell, *Phys. Rev.*, vol. 74, pp. 1869–1890, 1948.

[73] L. G Elliot and Bell P. E. , *Phys. Rev.*, vol. 76, p. 168, 1949.

[74] H. Mach *et al.*, *Nucl. Instr. and Meth.*, vol. A280, pp. 49–72, 1989.

[75] M. Moszyński and H. Mach, *Nucl. Instr. and Meth.*, vol. A277, p. 407, 1989.

[76] C. M. Rozsa *et al.*, *Brilliance 380 Scintillator Perforamnce Summary*, 2009.

[77] M. Moszyński *et al.*, *Nucl. Instr. and Meth*, vol. A567, p. 359, 2006.

[78] *Scintilation Products Technical Note available at.* www.detectors.saint-gobain.com.

[79] L. M. Fraile *et al.*, *Nucl. Instr. and Meth.*, vol. A701, p. 235, 2013.

[80] H. Mach and L. M. Fraile, "Hyperfine interactions, in press," 2012.

[81] E. V. D. van Loef *et al.*, *Nucl. Instr. and Meth*, vol. A 486, p. 254, 2002.

[82] J. Glodo *et al.*, *IEEE Trans. Nucl. Sci..*, vol. NS-52, p. 1805, 2005.

[83] W. W. Moses *et al.*, *Nucl. Instr. and Meth.*, vol. A 487, p. 123, 2002.

[84] K. S. Shah *et al.*, *IEEE Trans. Nucl. Sci. NS-51*, vol. NS-51, p. 2395, 2004.

[85] B. Morosin *et al.*, *J.Chem. Phys.*, vol. 49, p. 2007, 1968.

[86] J. F. Sharpey-Schafer, *Nucl. Phys. News. Int.*, vol. 14, p. 5, 2004.

[87] L. Msebi *et al.*, *To be published*, 2021.

[88] M. Ali, " Development and Characterization of a High Resolution Portable Gamma Spectrometer," Master's thesis, University of Ontario Institute of Technology, 2012.

[89] P. M. Jones *et al.*, *Nucl. Instr.and Meth. in Phy.Res.*, vol. A326, p. 556, 1995.

[90] P. N. Prashanth, *D.A.E Symp.on Nucl. Phys, Clover detectors set-up for the study of beta decay spectroscopy*, 2010.

[91] D. B. Campbell, "Angular momentum induced shape changes in the rare earth nuclei ^{152,153}Gd and ^{159,160}Yb," Ph.D. dissertation, Florida state University college of arts and sciences, 2004.

[92] W. R. Leo, *Technique for Nuclear and Particle Physics Experiment, page.113.* Lausanne, 1987.

[93] D. Radford, *Nucl. Instr.Methods Phys. Res. Sect.A*, vol. 361, p. 297, 1995.

[94] P. Nicolini *et al.*, *Nucl Instr Meth A*, vol. 582, p. 554, 2007.

[95] [Online]. Available: https://unarydigits.com/jkinz/

[96] N. Marginean *et al.*, *Eur. Phys. J*, vol. A 46, p. 329, 2010.

[97] J. M. Régis *et al.*, *Nucl. Instr. Methods*, vol. A 726, p. 191, 2013.

[98] T. Alharbi *et al.*, *Phys. Rev.*, vol. C 87, p. 014323, 2013.

[99] T. Alharbi *et al.* , *Applied Radiation and Isotopes*, vol. 70, p. 1337, 2012.

[100] P. J. R. Mason *et al.*, *Phys. Rev.*, vol. C 88, p. 044301, 2013.

[101] S. Kisyov *et al.*, *J. Phys.Conf. Ser*, vol. 366, p. 012027, 2012.

[102] S. Kisyov *et al* , *Phys. Rev*, vol. C 84, p. 014324, 2011.

[103] T. J. Paulus *et al.*, *IEEE Trans. Nucl. Sci.*, vol. NS-32/3, p. 1242, 1985.

[104] "Xia llc. pixie-16 user's manual. version 3.03,2018." [Online]. Available: http://www.xia.com

[105] I. Deloncle *et al.*, *J. Phys.:Conf. Ser.*, vol. 205, p. 012044, 2010.

[106] A. Iltis *et al.*, *Nucl. Instr. and Meth.*, vol. A563, p. 359, 2006.

[107] Y. Shao, *Phys. Med. Biol.*, vol. 52, p. 1103–1117, 2007.

[108] R. Pani *et al.*, *Nucl Instr Meth A*, vol. 610, pp. 41–4, 2009.

[109] D. Weisshaar *et al.*, *Nucl Instr Meth A*, vol. 594, p. 56, 2008.

[110] M. Ciemala *et al.*, *Nucl Instr Meth A*, vol. 608, pp. 76–79, 2009.

[111] P. Menge *et al.*, *Nucl Instr Meth A*, vol. 579, p. 6, 2007.

[112] P. Quarati *et al.*, *Nucl Instr Meth A*, vol. 574, p. 115, 2007.

[113] G. A. Kumar *et al.*, *Nucl Instr Meth A*, vol. 609, p. 183, 2007.

[114] G. A. Kumar *et al.* , *Nucl Instr Meth A*, vol. 610, p. 522, 2007.

[115] I. P. Etim *et al.*, *Lat. Am. J. Phys. Educ*, vol. 6, p. 1, 2012.

[116] O. J. Roberts *et al.*, *Nucl Instr Meth A*, vol. 748, p. 91, 2014.

[117] O. J. Roberts *et al* , *EPJ Web of Conferences*, vol. 63, p. 01018, 2013.

[118] M. Bashir, "Design, construction and characterisation of a low-level radioactivity counting system based on gamma-ray spectroscopy of labr$_3$(ce) scintillaor detectors," Ph.D. dissertation, Stellenbosch University, 2020.

[119] [Online]. Available: http://www.nndc.bnl.gov/nudat2/chartNuc.jsp

[120] J. M. Régis *et al.*, *Nucl. Instr. Methods*, vol. A 897, pp. 38–46, 2018.

[121] G. J. Wozniak *et al.*, *Nucl. Instr. Methods*, vol. 180, pp. 509–510, 1981.

[122] E. Lamprou *et al.*, "Characterization of tof-petdetectors based on monolithic blocks and asic-readout," 2018.

[123] J. Du, *el IEEE Trans Radiat Plasma Med Sci*, vol. 1(5), p. 385–390, 2017.

[124] J. M. Régis *et al.*, *Nucl. Instr. Methods*, vol. A 684, p. 36, 2012.

[125] J. M. Régis *et al* , *Nucl. Instr. Methods*, vol. A 622, p. 83–92, 2010.

[126] J. Cresswell and J. Sampson, "MTsort manual," 2006, http://nnst.dl.ac.uk/MIDAS/manual/MTsort/edoc033.

[127] [Online]. Available: https://root.cern/

[128] R. M. Lieder *et al.*, *Nuclear Physics A*, vol. 106(2), p. 389, 1967.

[129] H. Engel *et al.*, *Naturfosch*, vol. 27a, p. 1368, 19.

[130] K. Lan and W. Jorgenson, *Journal of Chromatography A*, vol. 915, p. 1, 2001.

[131] J. M. Régis *et al.*, *Phys. Rev.*, vol. C 95, p. 054319, 2017.

[132] J. M. Régis *et al.*, *EPJ Web of Conferences*, vol. 93, p. 01013, 2015.

[133] J. M. Régis, "Fast timing with labr$_3$(ce) scintillators and the mirror symmetric centroid difference method," Ph.D. dissertation, Köln, 2011.

[134] H. Mach *et al.*, *Nucl.Phys.*, vol. A523, p. 197, 1991.

[135] J.-M. Régis *et al.*, "- fast timing at x-ray energies and investigation on various timing deviations," *Nuclear Instruments and Methods in Physics Research Section A: Accelerators, Spectrometers, Detectors and Associated Equipment*, vol. 955, p. 163258, 2020. [Online]. Available: http://www.sciencedirect.com/science/article/pii/S016890021931527X

[136] Z. Bay, *Physical Review*, vol. 77, p. 419, 1950.

[137] K. E. G. Löbner, *The electromagnetic interaction in nuclear spectroscopy.* ed. W. D. Hamilton, North-Holland New York 1975, 173.

[138] E. R. Gamba, A. M. Bruce, and M. Rudigier, *Nucl. Instr. and Meth.*, vol. A928, p. 93–103, 2019.

[139] S. Ansari *et al.*, *Phys. Rev. C*, vol. 96, p. 054323, 2017.

[140] J. M. Régis *et al.*, *Nucl. Instr. Methods*, vol. A 736, p. 210, 2014.

[141] G. D. Dracoulis, J. L. Durell, and W. Gelletly, *Journal of Physics A: Mathematical, Nuclear and General*, vol. 6, no. 11, pp. 1772–1799, 1973. [Online]. Available: https://doi.org/10.1088/0305-4470/6/11/014

[142] G. D. Dracoulis, G. S. Foote, and M. G. Slocombe, "The g-factor of the 235 keV state in44sc," *Journal of Physics A: Mathematical, Nuclear and General*, vol. 7, no. 18, pp. 2289–2294, 1974. [Online]. Available: https://doi.org/10.1088/0305-4470/7/18/009

[143] M. Marmor, S. Cochavi, and D. B. Fossan, *Phys. Rev. Lett.*, vol. 25, pp. 1033–1035, 1970. [Online]. Available: https://link.aps.org/doi/10.1103/PhysRevLett.25.1033

[144] R. Hartmann, K. P. Lieb, and H. Röpke, *Nuclear Physics A*, vol. 123, no. 2, pp. 437 – 448, 1969. [Online]. Available: http://www.sciencedirect.com/science/article/pii/0375947469905120

[145] R. Hartmann and H. Grawe, *Nuclear Physics A*, vol. 164, no. 1, pp. 209 – 218, 1971. [Online]. Available: http://www.sciencedirect.com/science/article/pii/0375947471908517

[146] T. Nomura, C. Gil, H. Saito, T. Yamazaki, and M. Ishihara, "E2 effective charges of the $f_{\frac{7}{2}}$ proton and neutron deduced from the lifetimes of the 6^+ states in ^{50}Ti, ^{54}Fe, and ^{42}Ca," *Phys. Rev. Lett.*, vol. 25, pp. 1342–1345, 1970. [Online]. Available: https://link.aps.org/doi/10.1103/PhysRevLett.25.1342

[147] P. M. Lewis, A. R. Poletti, M. J. Savage, and C. L. Woods, "The mean life of the second 0+ state in ^{42}Ca," *Nuclear Physics A*, vol. 443, no. 2, pp. 210 – 216, 1985. [Online]. Available: http://www.sciencedirect.com/science/article/pii/037594748590260X

[148] P. C. Simms, N. Benczer-Koller, and C. S. Wu, "New application of delayed coincidence techniques for measuring lifetimes of excited nuclear states—^{42}Ca and ^{47}Sc," *Phys. Rev.*, vol. 121, pp. 1169–1174, 1961. [Online]. Available: https://link.aps.org/doi/10.1103/PhysRev.121.1169

[149] D. Bloess and F. Munnich, "Untersuchung der lebensdauer angeregter kernniveaus von ^{42}Ca," *Z.Naturforsch.*, vol. 18, p. 671, 1963.

[150] B. A. Brown and D. M. Rae, "The shell-model code nushellx@msu," *Nucl. Data Sheets*, vol. 120, p. 115, 2014.

[151] T. Shimizu *et al.*, *Prog.Theor.Exp.Phys.*, vol. 4502012, p. 01A205, 2012.

[152] M. Honma *et al.*, *Eur. Phys.J. A 25*, vol. Suppl. 1, p. 499, 2005.

[153] S. J. B. Mcgrory and E. C. Halbert, *Phys. Lett.*, vol. 37B, p. 1, 1971.

[154] B. A. Brown *et al.*, *Nucl.Phys.*, vol. A277, p. 77, 1977.

[155] K. H. Bhatt and J. B. McGrory, *Phys. Rev. C*, vol. 3, p. 2293, 1971.

[156] G. Stoitcheva *et al.*, "High-spin states in ^{44}Ti and ^{44}Sc," *Eur. Phys. J*, vol. A 25, pp. 509–510, 2005.

[157] P. R. Maurenzig, *The Structure of $f_{7/2}$ nuclei. Editrice Compositori.* Bologna, 1971.

[158] N. G. Alenius *et al.*, *Nuovo Cimento*, vol. 8, p. 147, 1972.

[159] G. Stoitcheva *et al.*, "High-spin intruder states in the fp shell nuclei and isoscalar proton-neutron correlations," *Phys. Rev.*, vol. C 73, p. 6, 2005.

[160] H. Ṙopke, *Eur. Phys. J.*, vol. A 22, p. 213, 2004.

[161] P. Bednarczyk *et al.*, *Eur. Phys. J.*, vol. A 20, p. 45, 2004.

[162] R. W. Ibbotson *et al.*, *Physical Review Letters*, vol. 10, p. 10, 1970.

[163] W. A. Richter *et al.*, *Nucl.Phys.*, vol. A 523, p. 325, 1991.

[164] R. Casten and P. von Brentano, *Phys. Rev.*, vol. C50, p. R1280, 1994.

[165] R. F. Casten and P. von Brentano, *Phys. Rev.*, vol. C51, p. 3528, 1995.

[166] M. Gerceklioglu, *Czech.J.Phys.*, vol. 52, p. 5, 2002.

[167] C. Gunther *et al.*, *Phys. Rev.*, vol. C54, p. 679, 1996.

[168] R. Betts, H. Fortune, J. Bishop, M. Al-Jadir, and R. Middleton, *Nuclear Physics A*, vol. 292, no. 1, pp. 281–287, 1977. [Online]. Available: https://www.sciencedirect.com/science/article/pii/0375947477903748

[169] P. Federman and S. Pittel, *Nucl. Phys.*, vol. A 155, p. 161, 1970.

[170] L. Mdletshe *et al.*, *To be published*, 2021.

[171] P. J. Twin, *Nucl.Phys.*, vol. A 520, p. 17c, 1990.